UNIVERSITY OF SOUTHAMPTON

FACULTY OF PHYSICAL SCIENCES AND ENGINEERING

Optoelectronics Research Centre

Laser-induced Ferroelectric and Photonic Structures in Lithium Niobate Crystals

by

Zisis Grigorios Konstantinos

Thesis for the degree of Doctor of Philosophy

March 2016

UNIVERSITY OF SOUTHAMPTON

ABSTRACT

FACULTY OF PHYSICAL SCIENCES AND ENGINEERING

OPTOELECTRONICS RESEARCH CENTRE

Doctor of Philosophy

Thesis for the degree of Doctor of Philosophy

LASER-INDUCED FERROELECTRIC AND PHOTONIC STRUCTURES IN LITHIUM NIOBATE CRYSTALS

Zisis Grigorios Konstantinos

The influence of laser illumination on ferroelectric domain engineering, waveguide formation and surface micro-structuring in lithium niobate (LN) is investigated. The ability to combine and to manipulate the size and depth of poling inhibited (PI) domains, which are produced by UV-laser irradiation of the +z face of congruent lithium niobate crystals followed by electric field poling, is demonstrated. It is therefore possible to produce complex domain structures, by partially overlapping individual UV laser irradiated tracks thus increasing the utility of this method for the fabrication of surface microstructures. Investigation of the electro-optic performance of ferroelectric/photonic composite structures, which occur naturally as a consequence of the PI process, had shown a significant enhancement (by ~ 36.7 % under the experimental conditions used) of the inherent electro-optic coefficient of the crystal attributed to large range stress at the domain boundaries. The feasibility of UV laser induced PI domain engineering in proton exchanged waveguides in LN was investigated showing that PI domain inversion is in principle possible. It requires however high laser intensity illumination which may produce significant surface damage. Additionally it was found that the proton concentration was also affected by the UV laser irradiation resulting in modifications of the original proton exchanged waveguide structure. Finally, an alternative to UV laser irradiation as a means for PI domain engineering and waveguide formation in LN is presented. This alternative method uses visible c.w. laser irradiation and an amorphous silicon absorbing layer to couple energy into the LN crystal thus emulating the direct absorption that occurs at UV wavelengths.

Table of Contents

List of Tables

List of Figures

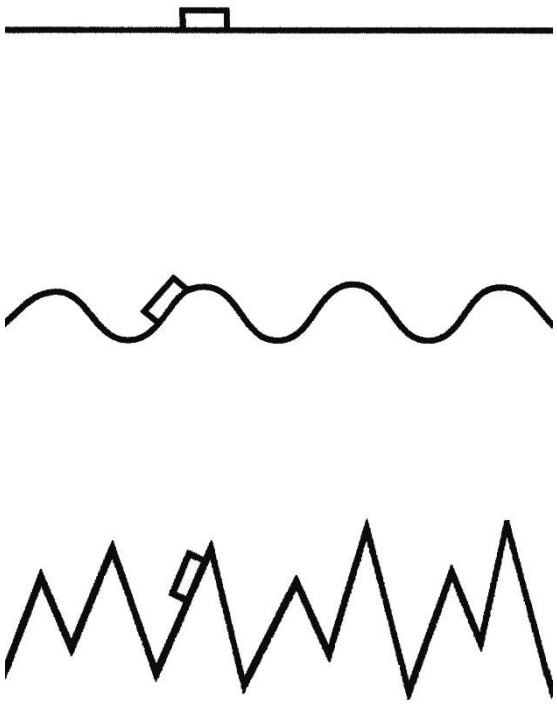

R. Bolaño, “The Savage Detectives” Picador, London, p. 672, 2007

DECLARATION OF AUTHORSHIP

I, Zisis Grigorios Konstantinos declare that this thesis, entitled “Laser-induced ferroelectric and photonic structures in Lithium Niobate crystals”, and the work presented in it are my own and has been generated by me as the result of my own original research.

I confirm that:

1. This work was done wholly or mainly while in candidature for a research degree at this University;
2. Where any part of this thesis has previously been submitted for a degree or any other qualification at this University or any other institution, this has been clearly stated;
3. Where I have consulted the published work of others, this is always clearly attributed;
4. Where I have quoted from the work of others, the source is always given. With the exception of such quotations, this thesis is entirely my own work;
5. I have acknowledged all main sources of help;
6. Where the thesis is based on work done by myself jointly with others, I have made clear exactly what was done by others and what I have contributed myself;
7. Parts of this work have been published as listed in Appendix:

Signed: .....

Date: ……..03/02/2016.....

Acknowledgements

As with any substantial body of work, contributions from many individuals have been made in a variety of ways. First of all, I would like to thank my supervisor Dr. Sakellaris Mailis for all his efforts in supervising, supporting and encouraging me. This thesis would never be accomplished without his help.

Thanks the ORC colleagues: Professor Rob W. Eason and Professor James Wilkinson for their comments and feedbacks in my 9- and 15-months viva, respectively. Dr. Collin Sones and Charlie Y. Ying, for passing on the much useful expertise and skills during my 3 month internship. I would also like to thank Gregorio Martinez-Jimenez and Yohann Franz for their companion in the lab and sharing with me their thoughts and concerns. I am also very grateful to physics clean room technician Zondy Webber and ORC technician Neil Sessions for all the support in my experiments.

Thanks also to our Bonn collaborator Dr. Elisabeth Soergel for all the PFM work and Ass. Professor Katia Gallo and her PhD student Michele Manzo from KTH for their work on the proton exchange waveguides.

Finally, special thanks to all my Sotonians friends for being there , to my friends back in Greece for not being there, my family for their continuous support and Sophia for the constant encouragement and inspiration.

Abbreviations

AFM	Atomic Force Microscope
APE	Annealed Proton Exchange
a-Si	Amorphous Silica
ASL	Acoustic Super-Lattices
CCD	Charge Coupled Device
CLN	Congruent Lithium Niobate
CW	Continuous Wave
DC	Direct Current
EFP	Electric Field Poling
EO	Electro-Optic
FE	Ferro-Electric
FWHM	Full Width at Half-Maximum
HF	Hydro-Fluoric
HW	High Voltage
IDT	Inter-Digitated Transducer
IR	Infra-Red
LN	Lithium Niobate
NA	Numerical Aperture
NPM	Non-Phase Matching
PE	Proton Exchange
PFM	Piezoresponse Force Microscopy
PI	Poling-Inhibition

Abbreviations

PPLN	Periodically Poled Lithium Niobate
QPM	Quasi Phase Matching
SAW	Surface Acoustic Wave
SEM	Scanning Electron Microscope
Si	Silicon
SHG	Second Harmonic Generation
SHW	Second Harmonic Wave
SLN	Stoichiometric Lithium Niobate
UV	Ultra-Violet
WUT	Waveguide Under Test

Chapter 1: Introduction

1.1 Introduction

After the first growth of crystalline lithium niobate (LN) in 1965 [1] using the Czochralski technique, and the reports about its synthesis [2] and its ferroelectricity [3], this material has been the subject of extensive research for the last 30 years resulted in almost a thousand publications. Its technological importance has resulted in tons of this crystal being grown each year. LN has a range of attractive physical properties (electro-optic, piezo-electric, acousto-optic, photo-refractive, pyro-electric, photo-voltaic, and optical non-linearity) [4], which led to applications in various areas of technology. Especially in photonics, it has become the material of choice for applications in optical communications [5], sensing [6], optical switching [5], nonlinear optical frequency generation [7] and surface acoustic wave (SAW) filtering [8].

Regarding non-linear optical applications, such as frequency conversion, LN offers the ability for quasi phase matching (QPM) by controlling the sign of the non-linear coefficient, $\chi^{(2)}$, by periodic inversion of the ferroelectric domains [9]. Although ferroelectric domain engineering has been developed primarily for QPM nonlinear frequency conversion [7], other applications are starting to arise such as the performance improvement of electro-optic [10] and acousto-optic devices [11], [12]. Surface micro-structuring by differential etching of domain engineered LN crystals is another option in the area of integrated optics [13], [14].

1.2 Synopsis

The development of a reliable technique in order to achieve precise domain inversion that will enhance the characteristics of the lithium niobate (LN) crystal by means of photonic functionality was the main motivation of this research work.

The first part of this thesis, which is included in Chapters 2 to 4, presents a step towards on the investigation of the UV laser direct writing process that has already been done by the Group of Non-linear Optical Materials, aiming at the optimisation of the technique that will allow the fabrication of advanced integrated photonic devices. This technique is capable to be used for domain engineering through the poling inhibition (PI) effect, waveguide fabrication, and micro-structuring on undoped congruent lithium niobate (CLN). The produced PI domains have a moderate depth (a few microns below the surface) that can be controlled, to some extent, by the laser exposure

conditions; providing a route to bypass some of the limitations of the conversional technique that is mainly used, which achieves domain inversion by the application of a patterned electric field, referred to as electric-field poling (EFP). Optical waveguides can be fabricated through this one step technique without the requirement of high temperatures, cleanroom environment or acid treatment. Additionally, using UV laser processing on LN crystal, is possible to fabricate a structure where a channel waveguide is made to overlap with an individual ferroelectric domain. Lastly, micro-structuring is possible by adding a hydrofluoric acid (HF) etching step after the fabrication of the UV-induced PI domains.

More specifically, an examination of the photonic micro-structure fabrication capabilities was performed by producing a range of different configurations (disks, rings, couplers, etc.). In addition, the variations in the nonlinear and electro-optic response as a consequence of PI domain inversion were under inspection and the waveguide characteristics. Finally, an investigation of the UV-induced PI domain inversion method in proton exchanged CLN waveguides was realized. It is essential here to note that these experiments stopped abruptly after a failure of the tube of the UV-laser on January of 2013. Although a significant amount of work had been already done by then, some future plans, which are described in the relative chapter (Chapter 6), weren't able to be finalised. The second part of this thesis, Chapter 5, arised as a result of this incident which engaged our group in discovering a new technique in order to avoid the restriction of using UV-lasers. A brief description of the contents of each chapter follows.

Chapter 1 presents a review of the crystalline structure of lithium niobate and discuss some of its physical properties relevant to the research work presented such as the linear electro-optic effect.

Chapter 2 discusses the technique of UV laser-induced poling inhibition in CLN crystals. A brief description of the effect is given, explaining the experimental domain formation processes, the mechanism that lies behind and the relevant domain visualisation methods. An investigation of the ability to manipulate the width and depth of the PI domains, is presented afterwards, by partially overlapping the subsequent UV laser irradiated tracks and by repeated UV irradiation along the same track, respectively. Finally, it is shown that complex domain structures, much wider than the irradiating laser spot, can be obtained by combining individual PI domains thus increasing dramatically the utility of this method for the fabrication of surface microstructures.

Chapter 3 presents an enhancement of the electro-optic coefficient in LN waveguides which are overlapping with a PI domain. The waveguide and the overlapping PI domain are both produced by a single UV irradiation process and thus they are self-aligning. The effect is attributed to the stress field, which is associated with the presence of a domain wall that contains the channel waveguide.

Chapter 4 contains a study of ferroelectric domain inversion in proton exchanged lithium niobate crystals following irradiation with a continuous wave (c.w) UV-laser beam. Local inhibition of poling, which is associated with UV irradiation of the +z face of the crystal has been observed

under specific conditions. The state of domain inversion of the processed crystals was investigated using differential etching in HF acid and piezoresponse force microscopy. Both investigation methods revealed that UV irradiation of post proton exchanged crystals modifies the proton concentration and consequently the associated waveguide.

Chapter 5 presents an alternative route to produce optical waveguides and poling inhibited ferroelectric domain in CLN using a hybrid composite a-Si/CLN platform, which uses a visible wavelength c.w. laser. A full description of this novel technique is given, explaining the fabrication process and the mechanism. An investigation of the waveguiding characteristics, first, and of the ferroelectric domains, later, as a function of the fabrication conditions is also given.

Finally, Chapter 6 contains a summary of suggestions for future work which is based on this thesis. The Appendix lists the related published and due submission papers emanating from this work.

1.3 Ferroelectrics

A ferroelectric crystal, as defined by Martienssen and Warlimont [15], is a crystal, which belongs to the pyroelectric family (i.e. exhibits a spontaneous electric polarization P_s) and whose direction of spontaneous polarization can be reversed by an electric field.

Generally, as indicated in Figure 1.1 [16], among the 32 point group crystal classes there are 21 non-centrosymmetric classes within which 20 are piezoelectric. Among the piezoelectric group, ten (10) have a temperature dependant spontaneous electric polarization P_s which is, hence they are pyroelectric. Ferroelectric crystals are a subgroup of the pyroelectric materials; therefore in their ferroelectric phase possess the properties of the groups in which they belong (non-symmetric, piezoelectric and pyroelectric). Possible nonlinear optical properties in ferroelectric crystals derive from the absence of inversion symmetry and are odd-rank polar tensor.

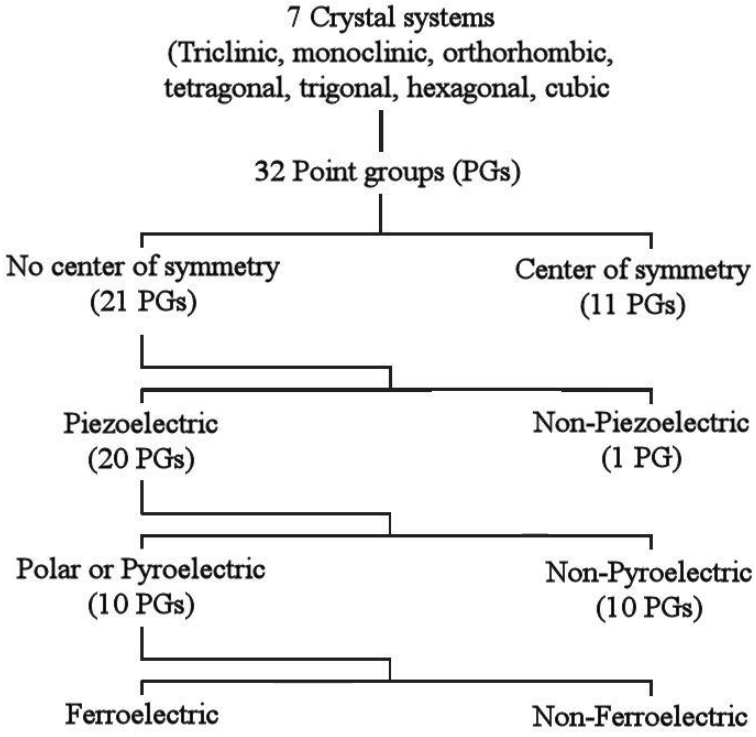

Figure 1.1 Grouping of crystal classes according to their piezoelectric, pyroelectric, ferroelectric and electrostrictive properties. Reprinted from Ref. [16]

The orientation of P_s can be changed in two or more orientational states at a temperature higher than the material's Curie point T_c or by applying an external electric field above a threshold value related to the crystal's coercive field E_c. When $T < T_c$ the crystal is in its ferroelectric phase. Above that temperature the crystal is in its paraelectric phase in which its electric dipoles are unaligned and cannot exhibit spontaneous polarization.

In its ferroelectric phase the orientational states of P_s that can be switched from one to other by an external field are crystallographic identical and only alter in the direction of the P_s vector. The homogenous region in which all of the dipole moments in adjacent unit cells have the same orientation is called ferroelectric domains and the plane/boundary that separates two different domain regions, is called domain wall [17].

1.4 Lithium Niobate

Lithium Niobate is an artificial ferroelectric crystal first fabricated in Bell Laboratories in the mid-sixties, which has numerous attractive properties (electro-optic, piezoelectric, acousto-optic, photorefractive, pyro-electric, photovoltaic). The main parameters (stoichiometry, defects, etc.) and properties of LN will be discussed in the following sections.

1.4.1 LN crystal structure-Stoichiometry

The Czochralski technique is the most common method for the growth of large, high quality single LN crystals in a number of different growth directions [1], [18]. LN can be grown in a wide range of compositions. The composition that matches exactly chemical compound symbol, $LiNbO_3$, having a ratio of [Li]:[Nb]:[O] of 1:1:3, is referred as *stoichiometric lithium niobate* (SLN), but due to the volatility of Li ions the growth of SLN is fairly challenging. The easiest and more common is the *congruent lithium niobate*, which is lithium-deficient and corresponds to congruent point at which both the solid and the liquid phase can co-exist. CLN have lithium ion concentration of less than 50 mol% Li_2O (typically ~ 48,5 mol% Li_2O).

LN is a uniaxial trigonal ferroelectric crystal and belongs to the 3m in the Hermann-Mauguin notation point crystal group [19]. In the ferroelectric phase it is also called oxygen octahedra ferroelectric [20] as the crystal structure is being consisted by six octahedral cages which are stacked with shared close-packed planes forming one unit cell. The oxygen atoms do not lie above one another but are arranged in a screw-like fashion, forming a succession of distorted octahedra along the polar z-axis (optic axis) which are filled with Li and Nb ions in the following sequence: "Li → Nb → vacancy (V) → Li → ..." along the positive polar direction, +z direction as illustrated in Figure 1.2. The Li and Nb ions however are not situated at equal distances between the oxygen planes but they are displaced slightly away from the octahedra centres (dashed lines) along the z-axis.

This displacement of the metallic ions is responsible for the existence of the electric dipole moment in the LN crystal. Each neighbouring Li-Nb pair, acts as individual dipoles which can all be aligned either 'up' or 'down' giving rise to two possible domain orientations.

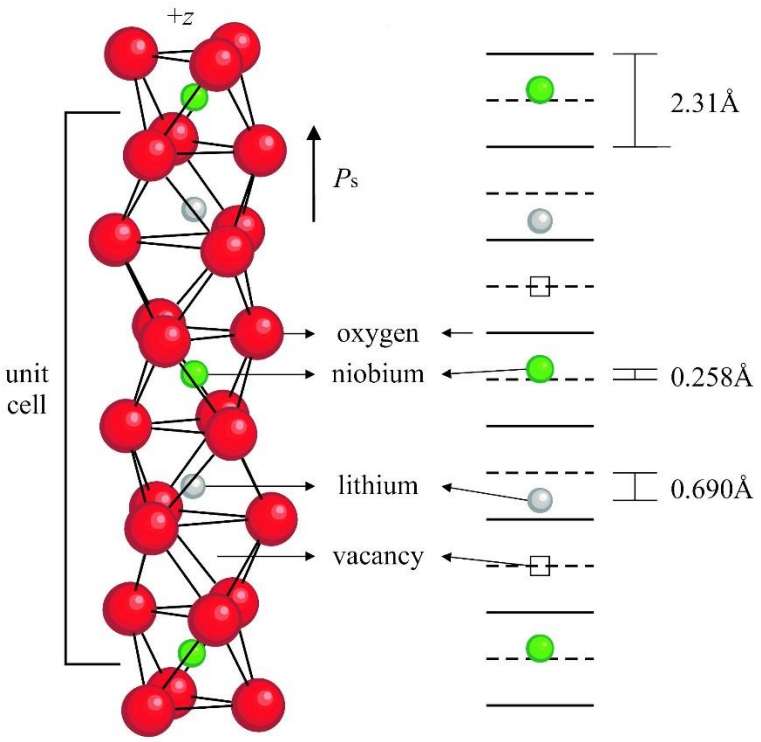

Figure 1.2 (a): the crystal structure of LN unit cell reprinted from Ref. [20] and b) the relative positions of the Li and Nb atoms in relation to the O planes represented by the black lines. The dashed lines represent the centre plane between two oxygen planes.

At temperatures higher than the Curie temperature, $T_c \sim 1210°C$, LN is in paraelectric state in which the Li ions are lying either slightly above or slightly below an oxygen layer, with the average position being planar with the oxygen and the Nb ions are located at the centre of oxygen octahedral. This configuration results in the non-polar paraelectric phase of the crystal.

1.4.2 Defects in congruent LN

Li deficiency characteristic in CLN is responsible for a high level of intrinsic defects, usually referred as *non-stoichiometric defects* and affects the physical properties of the crystal. Although there is some disagreement in the literature about the precise nature of this defect structure, it is commonly accepted that the anti-site defect, Nb on a lithium site, Nb_{Li}^{4+}, plays an important role in non-stoichiometric defects [21].

The influence of non-stoichiometry on physical properties can be understood within the framework that point defects arising from such non-stoichiometry are not randomly distributed but organized as defect clusters. These defect clusters can themselves possess a defect polarization P_D that is different from the lattice polarization P_s. Figure 1.3 shows schematics of a possible defect complex involving Nb_{Li} and V_{Li} as proposed in [22]. The proposed model describes how the equilibrium states of the defect complexes composed of a niobium antisite surrounded by three Li^+

vacancies in the nearest neighbourhood, plus one independent Li^+ vacancy along the polar c direction. Figure 1.3a depicts a stoichiometric $LiNbO_3$ unit cell, which acts as reference to the proposed stable defect states in congruent $LiNbO_3$ (Figure 1.3b,d) at room temperature.

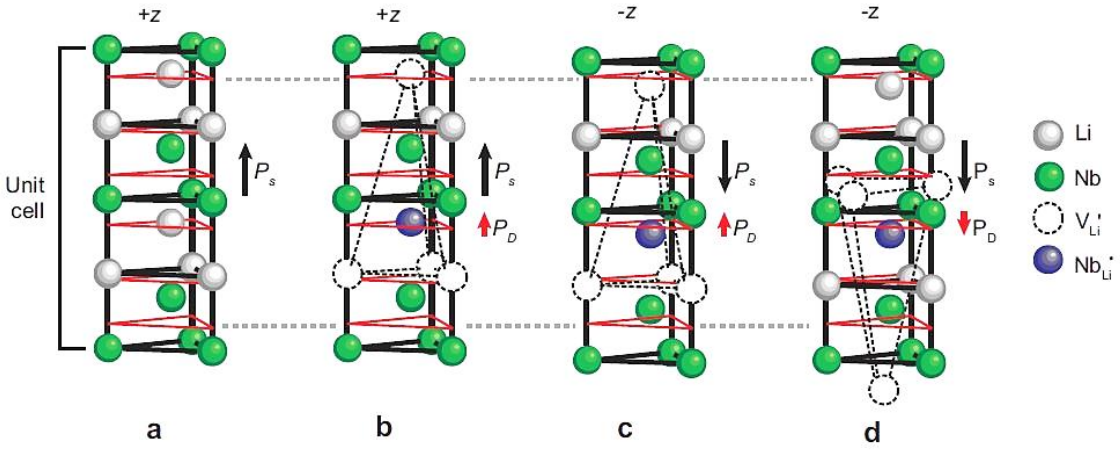

Figure 1.3 Schematics of a possible defect complex involving Nb_{Li} and V_{Li}. (a) A stoichiometric crystal with no defects. (b) A defect dipole complex in its low-energy configuration. Upon polarization reversal, state b becomes state c, in which the dipole in c is in a frustrated state. State c will relax to state d after annealing at >150◦C, which allows diffusion of V_{Li} . The defect polarization P_D is shown in b, c, and d. The oxygen planes are represented by red triangles.

In a stable defect state, the defect polarization P_D is assumed to be parallel to the lattice polarization *P*s. Upon domain reversal, domain state (Figure 1.3c) is achieved, which is termed as a *frustrated defect state* and is achieved when the niobium antisite defect moves to the neighbouring octahedron by the movement of Nb_{Li} through the close-packed oxygen plane. While V_{Li} remains at the same position because of lack of lithium mobility at room temperature. This frustrated state can be relieved into the stable state of Figure 1.3d after a high-temperature anneal [23], [24].

The size of defect clusters is restricted to ~ 11,4 Å (about four cation sites), while the average spacing between defect clusters along the chains is estimated to be ~76 Å [25].

1.5 Nonlinear optical properties

1.5.1 Second order nonlinear susceptibility

The absence of suitable lasing devices in the UV to near-visible region of the spectrum restricts the photonic applications. One of the main uses of lithium niobate crystals are in second

harmonic frequency conversion devices, which are able to generate a second harmonic wave (SHW) that has double frequency of the fundamental/input wave.

In order to achieve this, an electromagnetic wave must be incident on a dielectric medium. Then, electrons in the medium will be displaced from their equilibrium positions and start to oscillate under the influence of the oscillating electric field, producing oscillating electric dipoles resulting in a macroscopic polarization function which can be expressed as an expansion in powers of *E* field.

$$P_i(\omega) = \varepsilon_0 \left[\chi_{ij}^{(1)} E_j + \chi_{ijk}^{(2)} E_j E_k + \chi_{ijkl}^{(3)} E_j E_k E_l + \ldots \right] \quad 1\text{-}1$$

$$P = P^{(1)} + P^{(2)} + P^{(3)} + \ldots \quad 1\text{-}2$$

where ω is the angular frequency of the optical field *E*, ε_0 is the permittivity of free space, and $\chi_{ij}^{(1)}$ is the linear susceptibility which describes the linear response of the material with refractive index *n* and absorption α and $\chi_{ijk}^{(2)}$, $\chi_{ijkl}^{(3)}$ are the second- and third-order susceptibilities relatively, both responsible for nonlinear optical phenomena. Second-order nonlinear optical interactions can occur only in non-centrosymmetric crystals as LN crystal is.

A tensor of nonlinear optical coefficients, d_{ijk}, is typically used in place of the second-order nonlinear susceptibility according to the relation:

$$d_{ijk} = \frac{1}{2} \chi_{ijk}^{(2)} \quad 1\text{-}3$$

The *d* tensor can be described by a contracted notation, where d_{ijk} is expressed using two indices d_{il}, with l defined as in Table 1.1, allowing the convenient rearrangement of the third-order tensor into a 3×6 two-dimensional matrix.

jk :	11	22	33	23,32	31,13	12,21
l :	1	2	3	4	5	6

Table 1.1 Definition of the contracted notation

Taking into account the symmetry of point group 3m of LN as well, d_{ij} can be expressed in matrix form as:

$$d_{jk} = \begin{pmatrix} 0 & 0 & 0 & 0 & d_{15} & -d_{22} \\ -d_{22} & d_{22} & 0 & d_{15} & 0 & 0 \\ d_{31} & d_{31} & d_{33} & 0 & 0 & 0 \end{pmatrix} \quad 1\text{-}4$$

The most commonly used coefficients of the non-linear tensor are the coefficient $d_{22} = 3$ pm/V and the largest coefficient, $d_{33} = 31$ pm/V .

If we substitute an electric field of the form $E = E_0 \cos(\omega_1 t) + E_0 \cos(\omega_2 t)$ into Eq 1-1, the resulting polarization $P_i(\omega)$ will produce terms such as $(\omega_1 - \omega_2)$, $(\omega_1 + \omega_2)$, $2\omega_1, 2\omega_2$, leading to a range of physical processes that occur as a result of the second-order polarization term. One of those is the second harmonic generation (SHG) which occur when a non-centrosymmetric crystal is illuminated by an intense laser beam, resulting in second harmonic wave, with double frequency of the fundamental wave. The fundamental and second harmonic waves propagate throughout the crystal and the second harmonic term has an intensity proportional to the fundamental intensity squared, meaning that the second harmonic intensity increases quadratically over the interaction length L and its wavelength dependent with the term Δk the wave vector mismatch. If Δk is non-zero, the second harmonic intensity is modulated throughout the crystal, reducing the conversion efficiency hence phase matching (i.e. quasi-phase matching) is needed. The phase matching condition for SHG is:

$$\Delta k = k_{2\omega} - 2k_{\omega} = 0 \quad 1\text{-}5$$

Where k_{ω} and $k_{2\omega}$ are the wavevectors of the fundamental and frequency doubled waves.

1.5.2 Quasi-phase matching

Quasi-phase matching is a technique in order to correct the phase mismatch in the nonlinear process at regular intervals without completely matching the phase velocities. This can be achieved by using a periodic modification of the properties of the medium [9]. QPM does not rely in birefringence, thus under the appropriate design of the device, it is able to use the largest available 2nd order nonlinear coefficient, as in the case of lithium niobate.

Designing a periodic structure where the sign of the nonlinear coefficient *d* is inverted with period Λ in the direction of the wave propagation, we can compensate for nonzero wavevector mismatch Δk. The period Λ of the alternation of the crystalline axis must been set equal to twice the coherent build-up length l_c of the nonlinear interaction.

Such structure can be a periodically poled material, in which the orientation of one of the crystalline axes, often the z-axis of a ferroelectric material like lithium niobate, is inverted

periodically as a function of position within the material. This inversion of the z-axis is responsible for inverting the sign of the nonlinear coefficient *d*.

The nature of this effect is illustrated in Figure 1.4, where a comparison of relative phase-matching efficiencies for non-phase matching (NPM), perfect phase matching (PPM) and quasi-phase matching (QPM) is shown.

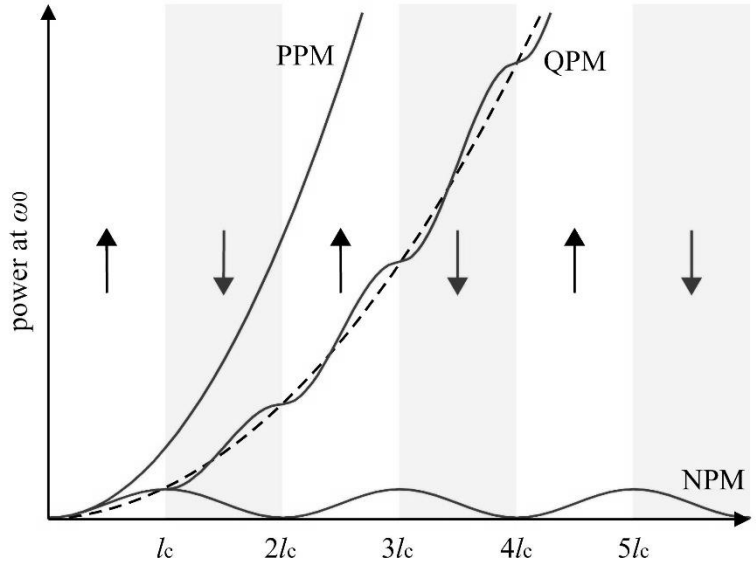

Figure 1.4 Comparison of relative phase-matching efficiencies for non-phase matching (NPM), perfect phase matching (PPM) and quasi-phase matching (QPM). The arrows indicate the direction of the spontaneous polarisation.

In the NPM trace the power of ω_0 oscillates sinusoidally with the travelled distance through the nonlinear crystal at a period of $2l_c$. Power flows from the fundamental to the 2nd harmonic until they experience a relative π phase shift between them at a distance of one coherence length. After this distance, the power flows back from the output waves to the input waves over the next l_c. This process repeats along the length of the nonlinear medium, preventing the growth of SHG waves. In PPM trace the phase matching condition is perfectly satisfied, and consequently the power at ω_0 grows linearly with the propagation distance. In the QPM trace, each time the power at ω_0 of the generated wave is about to begin to decrease as a consequence of the wavevector mismatch, a reversal of the sign of *d* occurs, which allows the power to continue to grow monotonically. Because the phases of the waves are not perfectly matched throughout the material, this technique is referred as quasi-phase matching.

Therefore, the phase matching condition becomes:

$$k_3 = k_2 + k_1 + K_g \tag{1-6}$$

$$\Delta k = k_3 - k_2 - k_1 - K_g = 0 \tag{1-7}$$

where $K_g = 2\pi q / \Lambda$ is the grating vector and $\Lambda = 2l_c$ is the fundamental period.

1.6 Physical properties

1.6.1 Linear electro-optic effect

The electro-optic effect, also called Pockels effect, is the change in the refractive index of a crystal when an electric field is applied. Like all second order nonlinearities, this effect is present due to the lack of crystal symmetry and is commonly used in the fabrication of optical modulators for applications in optical telecommunications.

In order to describe the electro-optic effect a definition of the 'index ellipsoid' must be given first. In optics, an index ellipsoid is a diagram of an ellipsoid that depicts the orientation and relative magnitude of refractive indices in a crystal and is generated by the equation:

$$\frac{Z_1^2}{n_1^2} + \frac{Z_2^2}{n_2^2} + \frac{Z_3^2}{n_3^2} = 1 \tag{1-8}$$

where Z_1, Z_2, and Z_3 are the principal axes, and n_1, n_2, and n_3 are the principal refractive indices. Eq. 1-8 indicates that the optical indicatrix in the absence of an electric field is an ellipsoid.

For optically uniaxial crystals like LN with $n_1=n_2=n_o$ (also called ordinary index) and $n_3=n_e$ (also called extraordinary index) the indicatrix can be written as:

$$\frac{1}{n_o^2}(Z_1^2 + Z_2^2)\frac{1}{n_e^2}Z_3^2 = 1 \tag{1-9}$$

When an electric field is applied, a corresponding change in the refractive index occurs. In order the above equation remain applicable new values of x, y, z need to be found. These new values x′, y′, z′ are related to the old x, y, z values by a third rank tensor with 27 elements. Symmetry conditions can then be used to reduce this tensor having just four independent elements. In the reduced subscript notation the tensor for lithium niobate can be expressed as

$$r_{ijk} = \begin{pmatrix} 0 & -r_{22} & r_{13} \\ 0 & r_{22} & r_{13} \\ 0 & 0 & r_{33} \\ 0 & r_{51} & 0 \\ r_{51} & 0 & 0 \\ -r_{22} & 0 & 0 \end{pmatrix} \qquad 1\text{-}10$$

Therefore, the linear EO effect in LN can be described by only four independent coefficients, r_{13}, r_{22}, r_{51} and r_{33}. The measured values of these coefficients depend on the mechanical constraints imposed on the crystal (if the crystal is unclamped the stress in the crystal is zero, if the crystal is clamped the strain in the crystal is zero) [4], on the temperature of the crystal and the wavelength of light [26]. The electro-optic coefficients of $LiNbO_3$ are: r_{33} = 32.6 pm/V, r_{31} = 10 pm/V, r_{22} = 6.8 pm/V at low frequency and r_{33} = 30.8 pm/V, r_{31} = 8.6 pm/V, r_{22} = 3.4 pm/V at high electric frequency [27].

The general relationship that describes the electro-optical effect can be written as $\Delta n \sim rE$, where *r* is the effective coefficient of the electro-optic tensor that links the specific refractive indices in the x, y, and z directions with the directions of the applied electric field.

When the applied electric field is along the z direction for example, from the indicatrix notation the actual value of Δn can be deduced as:

$$\begin{cases} \Delta n_o(E_z) = -\frac{1}{2} r_{13} n_o^3 E_z \\ \Delta n_e(E_z) = -\frac{1}{2} r_{33} n_e^3 E_z \end{cases} \qquad 1\text{-}11$$

1.6.2 Pyroelectric effect

The pyroelectric effect in LN is a well-known phenomenon that generates dynamic changes in spontaneous polarisation as a function of temperature [28]. For small temperature change δT, the relation between temperature change and polarization change is linear:

$$\delta P_i = p_i \delta T \qquad i = 1, 2, 3 \qquad 1\text{-}12$$

where the change of the spontaneous polarisation is δP_i and p_i is a pyroelectric tensor. This effect is a result of the motion of the Li and the Nb atoms relative to the oxygen octahedra for the LN case. Because these atoms movement is along the direction parallel to the z-axis only, the pyroelectric tensor is of the form:

$$p_i = \begin{bmatrix} 0 \\ 0 \\ p_3 \end{bmatrix} \qquad 1\text{-}13$$

The pyroelectric coefficient p_3 for LN is $p_3 = -4\times10^{-5}\mathrm{CK}^{-1}\mathrm{m}^{-2}$ [29].

1.6.3 Piezoelectric effect

Piezoelectricity refers to the linear connection between the electric polarisation and mechanical stress (direct piezoelectric effect) or between mechanical strain and applied electric field (converse piezoelectric effect).

The direct piezoelectric effect is described by the relationship between the induced polarisation and the stress and is expressed as:

$$P_i = d_{ijk}\sigma_{jk} \qquad 1\text{-}14$$

where d_{ijk} is a third-rank piezoelectric tensor (not to be confused with the second order susceptibility coefficient) and σ_{jk} is the second-rank stress tensor. Due to thermodynamic arguments it becomes that the stress tensor is symmetric ($\sigma_{jk} = \sigma_{kj}$), which leads the piezoelectric tensor with eighteen elements. Since LN has a 3m point symmetry, the piezoelectric stress tensor can be further reduced to having only four independent coefficients, namely d_{15}, d_{22}, d_{31} and d_{33} [26]. Measured values of these quantities are presented in Table 1.2 as gathered by Weiss [4]

d_{15}	d_{15}	d_{15}	d_{15}	**Ref.**
6.95	2.08	-0.085	0.6	[30]
6.8	2.1	-0.1	0.6	[31]
7.4	2.1	-0.087	1.6	[32]

Table 1.2 Piezoelectric strain coefficients [$\times10^{-11}$ C/N]

The converse piezoelectric effect, describes the mechanical deformation (strain ε) which is produced due an applying electric field (E). It can be shown through a thermodynamic argument that the coefficients connecting the induced strain and the applied E-field are identical to those connecting

the induced polarisation and the applied stress in the direct piezoelectric effect [33] and therefore can be expressed in tensor form as:

$$\varepsilon_{ij} = d_{ijk} E_k \qquad 1\text{-}15$$

Applications in which LN is used taking advantage of its piezoelectric properties are mostly in acoustics and more specifically in creation of either bulk or surface acoustic waves (SAW) in interdigitated transducers (IDTs) [34], bulk wave resonators [35] and more recently in acoustic superlattices (ASLs) [12], [36]. A variety of methods for domain imaging, especially scanning probe microscopy techniques (i.e. piezoresponse force microscopy (PFM)), rely on the converse piezoelectric effect [37].

1.7 Domain Engineering

Ferroelectric domain inversion is the process of reversing the direction of the spontaneous polarization of a ferroelectric material, thus inverting the sign of the $\chi^{(2)}$ nonlinear co-efficient. As illustrated in Figure 1.5, in order to change the direction of the electric dipole moment, lithium and niobium ions must undergo a transition within the oxygen lattice which is accompanied by a) a small displacement of the Nb from an asymmetric position along the optical axis (z-axis) within the same octahedron and (b) a corresponding motion of the Li from one octahedron to the adjacent vacant octahedron. This kind of transition requires a very large force, which can be created by the application of an electric field across the z-axis. The direction of motion of these cations defines the positive end of the spontaneous polarisation, P_s. Given that there are only two permitted directions along z (± z), only two possible domain orientations can exist, ± P_s.

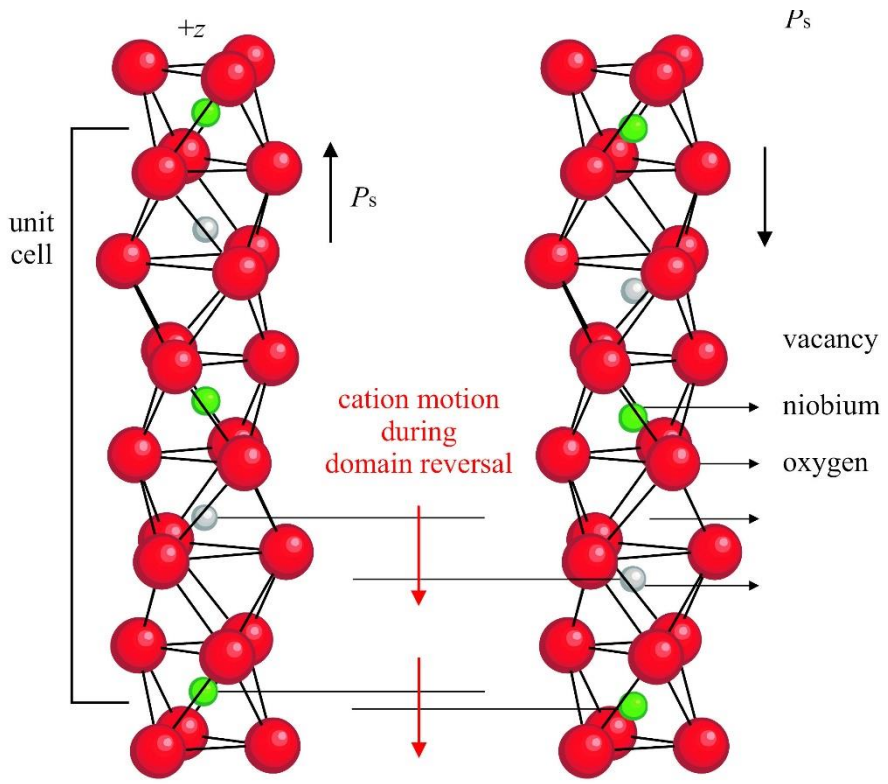

Figure 1.5 The unit cell of $LiNbO_3$ for +Ps and –Ps domains. Reprinted by Ref. [20]

The electric field which is required to invert the half of the dipoles is called *coercive field* and the process of reversing the direction of the spontaneous polarization of a ferroelectric material is called *domain inversion* or *poling* [20].

Domain inversion occurs not only for the z-axis but for the y-axis as well. Observing the dashed arrows along the z-axis of Figure 1.6, which illustrates a layer of crystal lattice of (a) virgin and (b) domain-inverted LN, it is shown the reversal along the original +z direction: from the virgin state of {Nb, V, Li, Nb, V, Li, ...} to the domain inverted state of {Nb, Li, V, Nb, Li, V, ...}. Moreover, the reversal of the cation order in the +y direction is being revealed too. The dashed arrows along the +y direction indicate that the order of cations and vacancies filling the oxygen octahedral interstices changing from virgin state of {Nb, Li, V, Nb, Li, V, ...} to domain inverted state of {Nb, V, Li, Nb, V, Li, ...}. Therefore, domain reversal from $+P_s$ to $-P_s$ can be considered as a twofold rotation operation of the unit cell about one of the x-axes (rotation of 180° about x-axes).

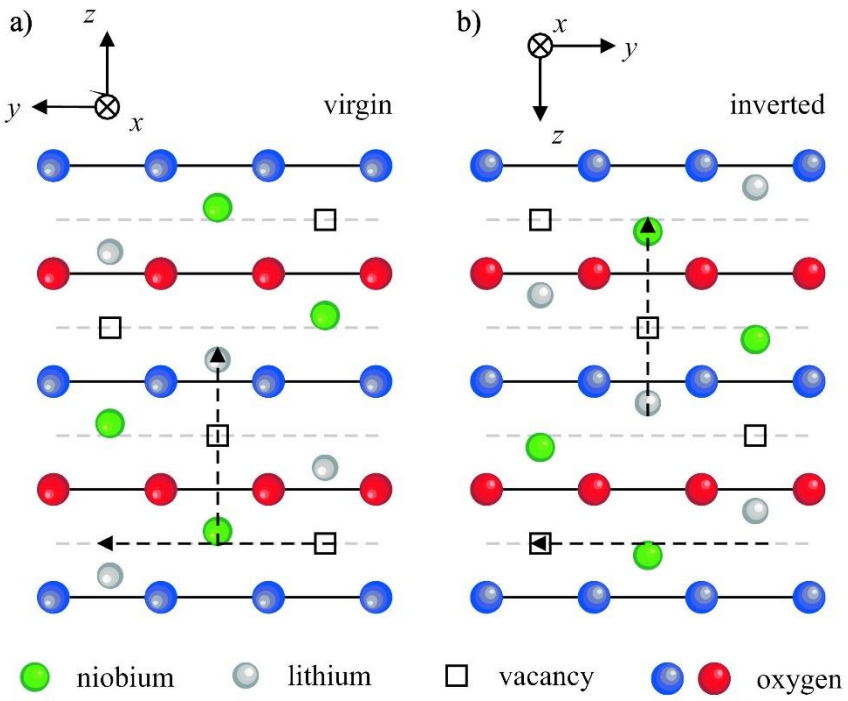

Figure 1.6 A layer of crystal lattice of (a) virgin and (b) domain-inverted LN replotted from Ref. [38]. The order of cation ions and vacancies is reversed along both y and z direction as indicated by the dashed arrows.

1.8 Electric-field poling

Electric-field poling has become the most commonly used and reliable method for domain engineering, particularly in the LN crystals. It enables the spatially preferential domain inversion through patterned electrodes usually defined by photolithography.

In this thesis work, EFP is used without the photolithography step since the domains are predefined by a UV illumination as will be explained in detail in following section. Figure 1.7 illustrates the EFP setup used in the experiments. The LN sample is mounted with two silicon O-rings between two transparent fused silica plates and contacted via water electrodes to apply an electric field along the z-axis. Using a white light source, a CCD camera and a pair of linear polarizers the domain inversion process can be observed in real time because of the strain induced different refractive indices between the antiparallel +z and –z domains due to the external electric field [39].

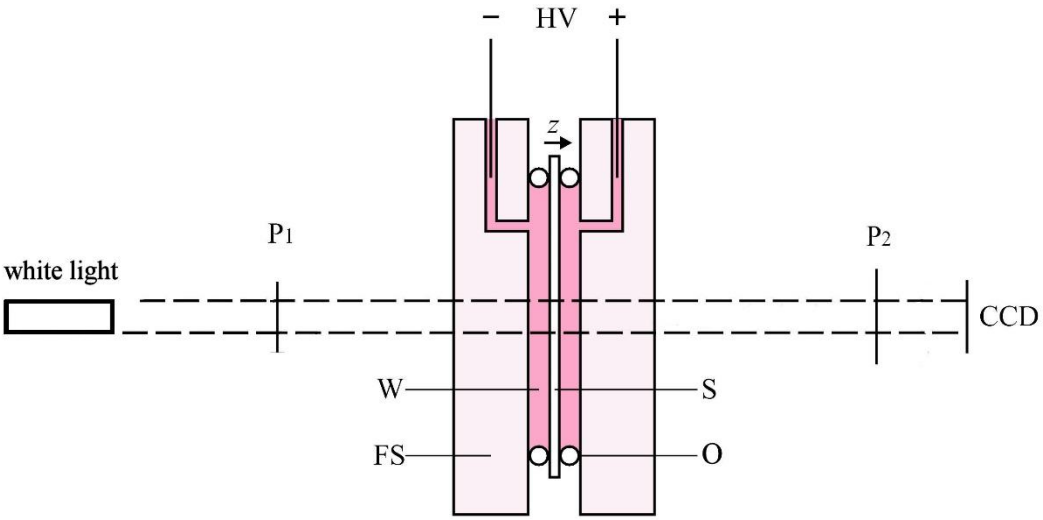

Figure 1.7 Electric field poling setup. The white light is of low intensity and used only for visualisation of the poling process via the crossed polarisers and CCD camera. (P1, P2 indicates the polarisers; HV the high voltage; W the water; S the LN sample; FS the fused silica and O the O-ring.)

1.9 Domain visualisation

In order to control the written domain structures, it is clear that the visualization of ferroelectric domains is essential. Depending on the particular requirements like image size, lateral resolution, dimensionality of imaging, and temporal resolution, a range of different detection mechanisms has been developed. Some of these methods have been reviewed in [37], [40]. Domain visualisation using one technique cannot promise secure results about the observed domain structure. Therefore, several visualisation methods must be used to verify the domain-nature of the written structure. The visualisation methods that were used in our experiments consist of 1) optical methods, 2) wet etching, 3) piezoresponse force microscopy, and 4) scanning electron microscopy (SEM).

1.9.1 Optical Techniques

Simple optical microscopy techniques are incapable of distinguishing domains of opposite orientations in ideal crystals since the later ones alter the sign of the second order susceptibility coefficient $\chi^{(2)}$ in Eq. 1-1 but not $\chi^{(1)}$,which remains unaffected and as a result no refractive index difference exists between these domains. However, in reality the inversion of the domain symmetry forces a stress-induced birefringence at the domain walls due to the photoelastic effect making possible the visualisation using crossed polarizers in an optical microscope [41], although this contrast can be eliminated by subsequent annealing [42].

A variety of optical methods for visualization of the ferroelectric domains or domain boundaries have proposed in literature taking advantage of being non-contact, non-invasive and most of them allowing a real-time observation of the domain-formation process. The diffraction-limited lateral resolution which is of about 1μm is a serious weakness although attempts to overcome this limitation have been suggested with, for instance, scanning confocal microscopy and scanning near-field microscopy. These techniques use different methods such as homogeneous illumination of the sample with light of wavelengths ranging from X-rays to the near infrared, second-harmonic generation employment or simple imaging of the topography that is altered by the presence of antiparallel domains.

1.9.2 Wet etching

The most common technique, although destructive, for high-resolution (<0.1μm) visualization of domain structures is chemical etching. The method is based on the different etch rates for the positive and negative ends of ferroelectric dipoles, thus it's also called differential etching. This preferential etching of the -z face may be due to weaker bond strengths in both the LiO_6 and NbO_6 octahedra [43] and wider oxygen triangle [44] on the −z side. The benefit of this technique is that it replaces the problem of the imaging of the domain structures with imaging topographical features. Subsequent etching, direct observation with an optical microscope, scanning electron microscopy, atomic force microscopy (AFM) or other surface-profiling methods can be applied. A schematic of the selective etching process is shown in Figure 1.8.

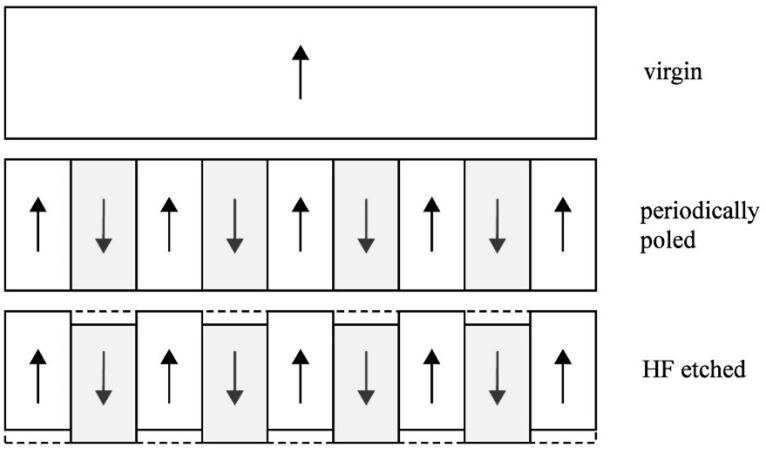

Figure 1.8 Schematic of a cross-section of LN crystal upon HF etching along c direction. The arrows indicate the direction of the polarization states: ↑ for +Ps and ↓ for –Ps domains.

The y faces also exhibit a similar etch characteristic, with the -y face etching much faster than the +y face in HF acid [45]. The x-face, on the other hand, doesn't etch since in x-face domain

inversion doesn't occur. Comparisons of room-temperature etch rates in pure HF for the y- and z-faces is shown in Table 1.3.

	Etch rate (μm/hr)		
Axis	**- face**	**+ face**	**Ref.**
z	0.8	nil	[46]
y	0.08-0.11	0.04-0.05	[38]

Table 1.3 Etching rates of LN in 48% HF acid at room temperature.

Sones et al. [46] suggested that the etching mechanism is initiated by surface protonation. It explains some of the qualitative observations that 1) the negative face is etched faster due to easier absorption of the positively charged proton, and 2) the etch rate increases with increasing concentration of acidic protons.

Although etching was developed for revealing of ferroelectric domain patterns, it has also become a significant tool for micro-structuring ferroelectric materials. Single tips for scanning probe applications [13], ridge waveguides [47] and free-standing cantilevers have been fabricated [14].

wedge polishing

In order to investigate the depth of the resulting PI domains, wedge polishing of the crystal surface has been used in this study. The polished wedge is performed using a Logitech polishing machine (PM2A) and a chemo-mechanical colloidal silica polishing suspension (with a pH 10.5, and particle size of 0.03μm) at an angle of approximately 5°, which results in stretching of the depth profile by a factor of 1/tan(5°) = 11.43. We then briefly etched the sample in HF to enable subsequent scanning electron microscopy SEM imaging. Figure 1.9 shows a schematic of the wedge polishing geometry.

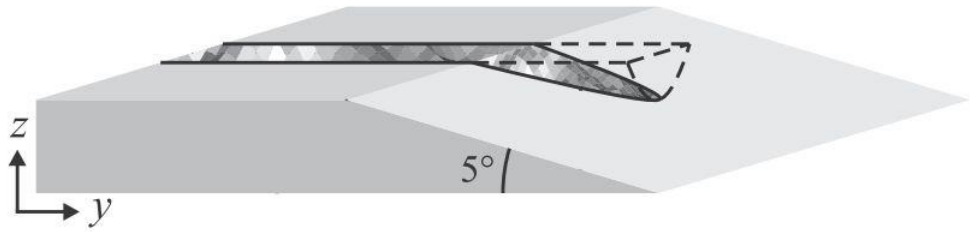

Figure 1.9 Schematic of the wedge polishing geometry.

1.9.3 Scanning electron microscopy

Imaging ferroelectric domains with SEM is challenging because all ferroelectrics are by nature dielectric materials that are highly insulating [48]. However, 180° domain patterns in LN and other ferroelectric materials have been observed in the secondary electron emission mode [49] by operating the SEM with low acceleration voltage. The possible explanation for the domain contrast is not yet clear. Most of them that have been proposed are based on: electrostatic interaction, converse piezoelectric effect and pyroelectric effect. In this thesis work, SEM for ferroelectric domain visualisation was used only after HF etching.

1.9.4 Piezoresponse force microscopy

Piezoresponse force microscopy provides a way for ferroelectric domain visualization. The PFM device is a modified force microscope that monitors the piezoresponse of the surface by applying an electric field to the surface through a conductive tip which subsequently measures the surface expansion due to the inverse piezoelectric effect. A schematic of the PFM set-up is shown in Figure 1.10.

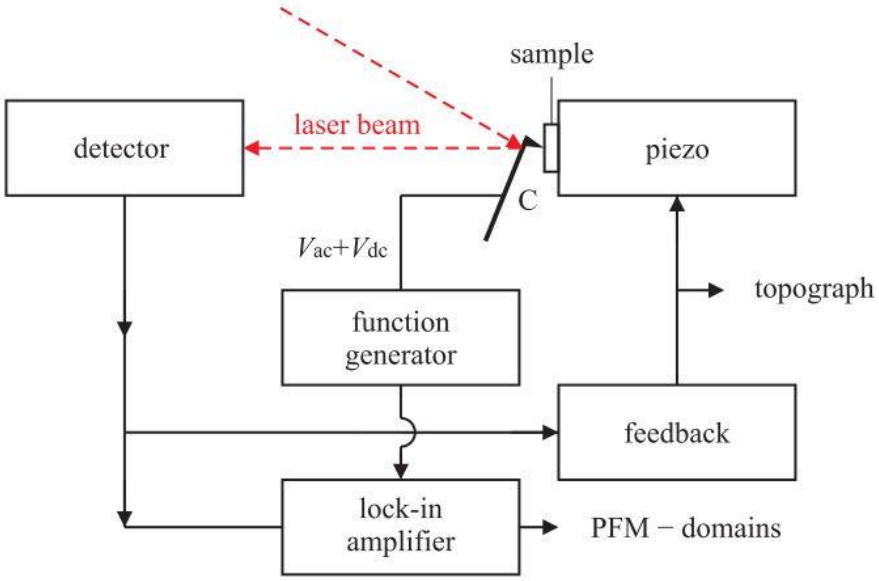

Figure 1.10 PFM measurement set-up reprinted from [37]. An alternating voltage with an optional offset is applied to the conducting tip. The back side of the sample is grounded. A contact-mode feedback is used. The domain signal is read out with a lock-in amplifier operating at the frequency of the alternating voltage that is applied to the tip. (C = Cantilever.)

The anisotropy of the crystal changes when the electric field is applied to the crystal because of the converse piezoelectric effect inducing strain which is measured by the tip deflection. The relationship between the strain and the applied electric field in piezoelectric materials is described

by the third-rank tensor as shown in section 1.6.3. In the case of the 180° walls in LN, the external field is applied along the z-axis. When the conducting tip is electrically contacted, a modulated alternating voltage $V_{ac}\cos(\omega t)$ with an optional offset voltage V_{dc} is applied:

$$V_{tip} = V_{dc} + V_{ac}\cos(\omega t) \qquad 1\text{-}16$$

where V_{tip} is the voltage applied on the tip, V_{ac} is the amplitude of the AC voltage applied on the tip, ω is the angular frequency of the modulation voltage with and t is the time.

The advantages of PFM are 1) high resolution of nanometres, and 2) in most cases it's a non-destructive technique. However, it has limited depth resolution of ~1.7 µm and therefore cannot differentiate between surface and bulk domain structures. All the PFM measurements which are presented in this thesis work were performed by our collaborator Dr. Elisabeth Soergel and her group at the University of Bonn in Germany.

1.10 References

[1] A. A. Ballman, “Growth of Piezoelectric and Ferroelectric Materials by the Czochralski Technique,” *J. Am. Ceram. Soc.*, vol. 48, no. 2, pp. 112–113, 1965.

[2] W. H. Zachariasen, “Untersuchungen äuber die kristallstruktur von sesquioxydenund verbindungen ABO3,” *Mat Naturv Klasse*, vol. 4, p. 312, 1928.

[3] B. Matthias and J. Remeika, “Ferroelectricity in the шlmenite ытructure,” *Phys. Rev.*, vol. 76, no. 12, pp. 1886–1887, Dec. 1949.

[4] R. S. Weis and T. K. Gaylord, “Lithium niobate: Summary of physical properties and crystal structure,” *Appl. Phys. A Mater. Sci. Process.*, vol. 37, no. 4, pp. 191–203, 1985.

[5] E. L. Wooten, K. M. Kissa, a. Yi-Yan, E. J. Murphy, D. a. Lafaw, P. F. Hallemeier, D. Maack, D. V. Attanasio, D. J. Fritz, G. J. McBrien, and D. E. Bossi, “A review of lithium niobate modulators for fiber-optic\ncommunications systems,” *IEEE J. Sel. Top. Quantum Electron.*, vol. 6, no. 1, pp. 69–82, 2000.

[6] L. Arizmendi, “Photonic applications of lithium niobate crystals,” *Phys. Status Solidi*, vol. 201, no. 2, pp. 253–283, Jan. 2004.

[7] M. Yamada, N. Nada, M. Saitoh, and K. Watanabe, “First-order quasi-phase matched $LiNbO_3$ waveguide periodically poled by applying an external field for efficient blue second-harmonic generation,” *Appl. Phys. Lett.*, vol. 62, no. 5, pp. 435–436, 1993.

[8] A. Oliner, “Waveguides for surface waves,” *Acoust. Surf. Waves*, vol. 24, pp. 187–223, 1978.

[9] J. A. Armstrong, N. Bloembergen, J. Ducuing, and P. S. Pershan, “Interactions between Light Waves in a Nonlinear Dielectric,” *Phys. Rev.*, vol. 127, no. 6, pp. 1918–1939, Sep. 1962.

[10] D. Janner, D. Tulli, M. García-Granda, M. Belmonte, and V. Pruneri, “Micro-structured integrated electro-optic $LiNbO_3$ modulators,” *Laser Photonics Rev.*, vol. 3, no. 3, pp. 301–313, Apr. 2009.

[11] H. Gnewuch, N. K. Zayer, C. N. Pannell, G. W. Ross, and P. G. Smith, “Broadband monolithic acousto-optic tunable filter.,” *Opt. Lett.*, vol. 25, no. 5, pp. 305–307, Mar. 2000.

[12] D. Yudistira, S. Benchabane, D. Janner, and V. Pruneri, “Surface acoustic wave generation in ZX-cut $LiNbO_3$ superlattices using coplanar electrodes,” *Appl. Phys. Lett.*, vol. 95, no. 5, p. 052901, 2009.

[13] I. E. Barry, G. W. Ross, P. G. R. Smith, R. W. Eason, and G. Cook, “Microstructuring of

lithium niobate using differential etch-rate between inverted and non-inverted ferroelectric domains," *Mater. Lett.*, vol. 37, no. 4–5, pp. 246–254, 1998.

[14] C. Sones, S. Mailis, V. Apostolopoulos, I. E. Barry, C. Gawith, P. G. R. Smith, and R. W. Eason, "Fabrication of piezoelectric micro-cantilevers in domain-engineered $LiNbO_3$ single crystals," vol. 12, pp. 53–57, 2002.

[15] T. Mitsui, "Ferroelectrics and Antiferroelectrics," in *Springer Handbook of Condensed Matter and Materials Data*, W. Martienssen and H. Warlimont, Eds. Springer Berlin Heidelberg, 2005, pp. 903–938.

[16] V. Gopalan, K. Schepler, V. Dierolf, and I. Biaggio, "Ferroelectric Materials," in *The Handbook of Photonics, Second Edition*, CRC Press, 2006, pp. 6–66.

[17] M. Lines and A. Glass, *(The International series of monographs on physics) Malcolm E. Lines, Alastair M. Glass-Principles and applications of ferroelectrics and related materials-Clarendon Press (1977).pdf*. Clarendon Press, 1977.

[18] K. Nassau, H. J. Levinstein, and G. M. Loiacono, "The Domain Structure and Etching of Ferroelectric Lithium Niobate," *Appl. Phys. Lett.*, vol. 6, no. 11, pp. 228–229, Jun. 1965.

[19] S. C. Abrahams and P. Marsh, "Defect structure dependence on composition in lithium niobate," *Acta Crystallogr. Sect. B Struct. Sci.*, vol. 42, no. 1, pp. 61–68, Feb. 1986.

[20] V. Gopalan, V. Dierolf, and D. a. Scrymgeour, "Defect–Domain Wall Interactions in Trigonal Ferroelectrics," *Annu. Rev. Mater. Res.*, vol. 37, no. 1, pp. 449–489, Aug. 2007.

[21] O. F. Schirmer, O. Thiemann, and M. Wöhlecke, "Defects in $LiNbO_3$—I. experimental aspects," *J. Phys. Chem. Solids*, vol. 52, no. 1, pp. 185–200, Jan. 1991.

[22] S. Kim, V. Gopalan, K. Kitamura, and Y. Furukawa, "Domain reversal and nonstoichiometry in lithium tantalate," *J. Appl. Phys.*, vol. 90, no. 6, pp. 2949–2963, 2001.

[23] V. Gopalan, N. A. Sanford, J. A. Aust, K. Kitamura, and Y. Furukawa, *Chapter 2 - Crystal growth, characterization, and domain studies in lithium niobate and lithium tantalate ferroelectrics*. Elsevier, 2001.

[24] V. Gopalan and M. C. Gupta, "Origin and characteristics of internal fields in $LiNbO_3$ crystals," *Ferroelectrics*, vol. 198, no. 1, pp. 49–59, Jun. 1997.

[25] N. Zotov, F. Frey, H. Boysen, H. Lehnert, a. Hornsteiner, B. Strauss, R. Sonntag, H. M. Mayer, F. Güthoff, and D. Hohlwein, "X-ray and neutron diffuse scattering in $LiNbO_3$ from 38 to 1200 K," *Acta Crystallogr. Sect. B Struct. Sci.*, vol. 51, no. 1958, pp. 961–972, Dec. 1995.

[26] R. E. Newnham, *Properties of materials*. Oxford University Press, 2005.

[27] K. K. Wong, "Electro-Optic Coefficients of $LiNbO_3$," in *Properties of Lithium Niobate*, Institution of Engineering and Technology, 2002.

[28] M. Bass, L. S. Weichman, S. Vigil, and B. K. Brickeen, "The temperature dependence of Nd^{3+} doped solid-state lasers," *IEEE Journal of Quantum Electronics*, vol. 39, no. 6. pp. 741–748, 2003.

[29] A. Savage, "Pyroelectricity and spontaneous polarization in $LiNbO_3$," *J. Appl. Phys.*, vol. 37, no. 8, pp. 3071–3072, 1966.

[30] R. T. Smith and F. S. Welsh, "Temperature Dependence of the Elastic, Piezoelectric and Dielectric Constants of Liqthium Tantalate and Niobate," *J. Appl. Phys.*, vol. 42, no. 6, pp. 2219 – 2230, 1971.

[31] A. W. Warner, "Determination of Elastic and Piezoelectric Constants for Crystals in Class (3m)," *J. Acoust. Soc. Am.*, vol. 42, no. 6, p. 1223, 1967.

[32] T. Yamada, N. Niizeki, and H. Toyoda, "Piezoelectric and elastic properties of lithium niobate single crystals," *Japanese J. Appl.*, vol. 151, 1967.

[33] S. Haussühl, *Physical Properties of Crystals: An Introduction*, vol. 2nd. Oxford: Clarendon Press, 2008.

[34] R. M. White and F. W. Voltmer, "Direct Piezoelectric Coupling To Surface Elastic Waves," *Appl. Phys. Lett.*, vol. 7, no. 12, p. 314, 1965.

[35] C. K. Campbell, "Applications of surface acoustic and shallow bulk acoustic wave devices," *Proc. IEEE*, vol. 77, no. 10, pp. 1453–1484, 1989.

[36] I. P. Crystal, Y. Lu, Y. Zhu, Y. Chen, and S. Zhu, "Optical Properties of an Ionic-Type Phononic Crystal," *Science*, vol. 284, no. June, pp. 1822–1824, Jun. 1999.

[37] E. Soergel, "Visualization of ferroelectric domains in bulk single crystals," *Appl. Phys. B*, vol. 81, no. 6, pp. 729–751, Oct. 2005.

[38] C. E. Valdivia, "Light-Induced Ferroelectric Domain Engineering in Lithium Niobate & Lithium Tantalate," 2007.

[39] J. F. Schooley, W. R. Hosler, and M. L. Cohen, "Superconductivity in semiconducting $SrTiO_3$" *Phys. Rev. Lett.*, vol. 12, no. 17, pp. 474–475, Oct. 1964.

[40] V. Bermúdez, A. Gil, L. Arizmendi, J. Colchero, A. M. Baró, and E. Diéguez, "Techniques of observation and characterization of the domain structure in periodically poled lithium

niobate," *J. Mater. Res.*, vol. 15, no. 12, pp. 2814–2821, 2011.

[41] V. Gopalan and M. C. Gupta, "Origin of internal field and visualization of 180° domains in congruent $LiTaO_3$ crystals," *J. Appl. Phys.*, vol. 80, no. 11, p. 6099, 1996.

[42] S. Kim and V. Gopalan, "Optical index profile at an antiparallel ferroelectric domain wall in lithium niobate," *Mater. Sci. Eng. B*, vol. 120, no. 1–3, pp. 91–94, Jul. 2005.

[43] D. Xue and K. Kitamura, "Origin of Differential Etching Rates of the + Z and - Z Faces of Lithium Niobate Crystal," *Ferroelectr. Lett. Sect.*, vol. 29, no. 5–6, pp. 89–93, 2002.

[44] X. Zhang, D. Xue, and K. Kitamura, "Domain characteristics and chemical bonds of lithium niobate," *Mater. Sci. Eng. B*, vol. 120, no. 1–3, pp. 21–26, 2005.

[45] N. Niizeki, T. Yamada, and H. Toyoda, "Growth Ridges, Etched Hillocks, and Crystal Structure of Lithium Niobate," *Jpn. J. Appl. Phys.*, vol. 6, no. 3, p. 318, 1967.

[46] C. L. Sones, S. Mailis, W. S. Brocklesby, R. W. Eason, and J. R. Owen, "Differential etch rates in z-cut $LiNbO_3$ for variable HF/HNO_3 concentrations," *J. Mater. Chem.*, vol. 12, no. 2, pp. 295–298, Jan. 2002.

[47] C. L. Sones, P. Ganguly, C. Y. J. Ying, E. Soergel, R. W. Eason, and S. Mailis, "Poling-inhibited ridge waveguides in lithium niobate crystals," *Appl. Phys. Lett.*, vol. 97, no. 15, p. 151112, 2010.

[48] R. Le Bihan, "Study of ferroelectric and ferroelastic domain structures by scanning electron microscopy," *Ferroelectrics*, vol. 97, no. 1, pp. 19–46, 1989.

[49] R. Le Bihan, D. Averty, D. Pain, A. L. Aleksandrovski, and I. I. Naumova, "Study of lithium niobate with periodically reversed domains," *Ferroelectrics*, vol. 172, no. 1, pp. 181–186, 1995.

Chapter 2: UV laser-induced poling-inhibition in CLN

2.1 Introduction

UV laser-induced poling inhibition provides a new approach for domain engineering in lithium niobate. Continuous wave laser irradiation at 305-244nm wavelength on the +z face of undoped and MgO-doped congruent lithium niobate single crystals has been observed to inhibit ferroelectric domain inversion directly beneath the illuminated regions during a subsequent EFP step. The effect, which is referred to as *poling-inhibition*, was first investigated by Sones et al.[1]. The PI domain inversion has been investigated by differential HF etching [1] and piezoresponse force microscopy [2]. The spatially selective irradiation of the +z face of the crystal produces a multi-domain region, where the previously irradiated areas of the surface maintain their original +z polarity within a poled –z domain background. The effect has been examined in detail by previous works showing that the depth of the pole-inhibited domains is of ~ a few μm and depends upon the UV exposure conditions [3]. The proposed model for PI domain formation is based on the migration of lithium ions due to (i) diffusion in the temperature gradients [4] that are formed as a consequence of the strong UV laser absorption within a thin layer of the crystal and (ii) a drift in the pyro-electric field [5] which is again a consequence of the heating of the crystal during the UV irradiation process. This mechanism, which will be discussed in detail in a following section, is also responsible for a local increase of the extraordinary refractive index (n_e) that leads to the formation of optical waveguides in LN [6], [7].

The width of the PI domains corresponds roughly to the laser beam width and is not restricted by the crystal symmetry allowing the fabrication of arbitrarily shaped domains. Additionally, differential etching of domain-engineered crystals allows for surface micro-structuring [8], [9]. Wet etching of these poling- inhibited domain structures in HF acid produces surface-relief structures such as ridges, which can support optical guided-wave propagation because of the inscribed refractive index change [10].

A brief introduction of the UV laser-induced poling inhibition in LN crystals will be given that will form the basis for investigation of the ability to manipulate the width and depth of the PI domains, which forms the subject of this chapter. It will be shown here that the PI domain size restrictions that are imposed by the laser beam can be overcome by overlapping irradiated tracks that hence produce larger domains. Finally, it will be shown that it is possible to influence the depth of the PI domains by repeated irradiation of the same area of the crystal that pushes the lithium distribution deeper into the crystal. Periodic domain structures of limited depth have been shown to be suitable for the generation of surface acoustic waves [11]. Such structures have been fabricated here using the PI domain method.

2.2 Fabrication and characterization of UV laser-induced PI domains

Fabrication: The first step of the fabrication of PI domains is the direct UV laser writing. UV laser writing at 244 nm [6], [7], which is a wavelength where LN exhibits strong absorption, on the +z face of the crystal was performed using the setup shown in Figure 2.1. Sets of parallel lines were drawn on the +z faces of the crystals along the crystallographic y-direction using a wide range of conditions (writing speed and power).

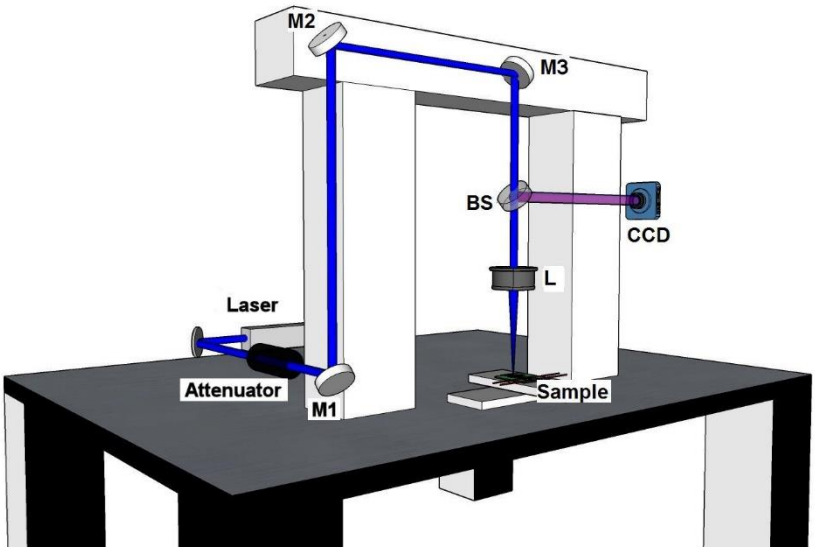

Figure 2.1 Schematic of the laser writing set-up. The sample is mounted on a two axis computer-controlled stage. M1, M2, M3 indicates the mirrors, BS the beam splitter, L the focusing lens and CCD the camera.

The second step includes electric field poling in order to uniformly pole the crystals apart from the UV pre-illuminated regions, where poling has been inhibited. Applying an external electric field, using the EFP setup described in Ref. [12], results in a set of parallel stripes of +z polar surface embedded in a uniform –z polar surface background [10]. A slow forward poling is conducted at the lowest possible poling voltage ensuring that the domain inversion process is slow, in terms of domain wall velocity [13]. The term *slow poling* is being further discussed at section 2.4. In addition, a thorough description of the UV laser-induced PI method can be found in Ref. [10].

Characterization: In order to measure the depth of the resulting PI domains, scanning electron microscopy is used on "wedge polished" samples which have been etched for ~1min to reveal the presence of inverted ferroelectric domains due to differential etching between opposite polar surfaces [14]. Wedge polishing of the crystal surface is used to magnify the depth of the resulting domains by projecting them on the slightly inclined polished plane, which still maintains the domain sensitive differential etching property in HF acid. In that way, the measurements of the domains are taken with better accuracy. Figure 2.2 shows a schematic of the wedge polishing geometry (top) and an SEM

image of the stretched (due to wedge polishing) depth profile of a UV laser-induced PI domain made visible by brief HF acid etching (bottom).

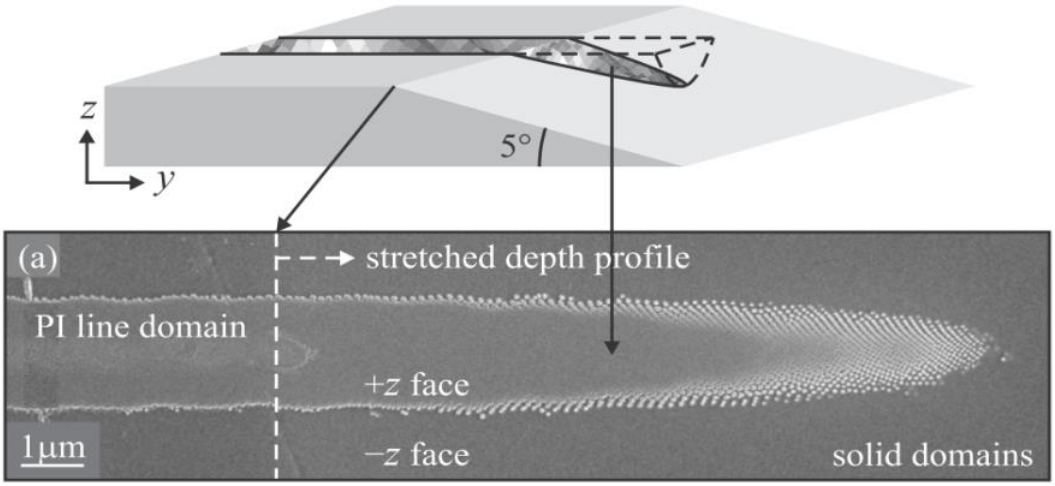

Figure 2.2 top: schematic of the wedge polishing geometry. Bottom: SEM image of the stretched depth profile of a PI domain [15].

The process for obtaining PI domains requires tight focussing of the UV laser beam in order to achieve sufficiently high temperatures that are required for the lithium to diffuse away and modify the refractive index and hence the coercive field. As a consequence the width of the PI domains is a function of the irradiating spot size, which defines the resolution to fabricate arbitrary domain/surface structures. The size (depth and the width) of the PI domains depends also on the UV laser exposure conditions: laser intensity and scan time of the irradiating beam, which are controlled by the scanning speed. It has been shown that the depth of individual isolated domain tracks varies between 2.5μm and 5μm depending upon irradiation conditions [16]. Domain depth can be controlled as well with multi-pass exposures, as will be shown in section 2.5.2.

2.3 PI mechanism

The mechanism, which has been proposed for the explanation of poling-inhibition, is the following. The strong absorption of UV radiation within a small volume close to the surface of the crystal heats the crystal locally. The temperature, which on the surface is as high as the melting point ~1250^{o}C, is reduced rapidly in depth, producing a large temperature gradient [4]. Under this temperature distribution Li ions i) diffuse under the influence of the diffusivity gradient [1], and ii) drift under the influence of the pyroelectric effect. The migration of Li ions during the heating process results in two Li deficient regions, one located close to the surface and the second at some distance below the surface. Due to the fact that Li deficiency is related with a higher coercive field in LN [17]

(a higher coercive field corresponds to a lower Li ion concentration), the Li deficient region inhibits the domain wall propagation during poling.

2.4 Kinetics of Domain Inversion

The amplitude of the applied electric field must ensure that domain inversion occurs slowly, which is desirable since the kinetics of the domain wall motion are seen to influence greatly the shape and quality of the resultant structures. We will denote this type of domain formation by *slow poling*. The necessity for a slow domain growth process comes directly from the fact that if the domain wall grows so fast that the domain wall energy is sufficient to overcome the energy barrier built by the frozen charges, the inhibited domain may not be solid or even survive. The widths of domains formed with slow poling are wider as compared to those formed with fast poling [5].Moreover, complex domain structures with two separated domains on the surface and in depth along the c-axis has been observed, owing to the fast poling process with higher domain wall energy to reveal the detail Li concentration distributions.

2.5 Ferroelectric domain building blocks for photonic and nonlinear optical microstructures in $LiNbO_3$

The experimental work which is presented in this section investigates the ability to manipulate the size and depth of poling-inhibited domains, which are produced by UV laser irradiation on the +z face of lithium niobate crystals followed by electric field poling. It is shown that complex domain structures, much wider than the irradiating laser spot, can be obtained by partially overlapping the subsequent UV laser irradiated tracks. The result of this stitching process is one uniform domain without any remaining trace of its constituent components thus increasing dramatically the utility of this method for the fabrication of surface microstructures as well as periodic and aperiodic domain lattices for nonlinear optical and surface acoustic wave applications. Finally, the impact of multi exposure on the domain characteristics is also investigated indicating that some control over the domain depth can be attained.

2.5.1 Impact of domain proximity

During the first step of PI domain fabrication the +z face of the crystal was irradiated with a c.w. UV laser beam (λ=244nm) focussed to a spot size ranging between 1.5-3 μm. Laser irradiated tracks were written on the +z face of 500 μm thick congruent LN crystal samples(Crystal Technology, USA) by scanning them in front of the focussed laser beam using a set of computer-

controlled two axes translation stage (Aerotech ABL1500) which feature nanometre resolution, at a constant writing speed of 0.1mm/s. The laser intensities used in these experiments were within the range of 0.10-0.20 MW/cm^2. However, the intensity range between 0.13 MW/cm^2 and 0.16 MW/cm^2, which is close but below the threshold for surface damage produces PI domains of the best quality (solid and deep).

The second step requires the application of a uniform electric field along the z-direction of the crystal. The amplitude of the applied electric field was kept around ~19.5kV/mm ± 100V/mm which ensured that the domain inversion process was slow, in terms of domain wall velocity[18].

The depth of the resulting PI domains can be measured using scanning electron microscopy on wedge polished samples which had been etched for ~1 min to reveal the presence of inverted ferroelectric domains due to differential etching between opposite polar surfaces[14]. Wedge polishing of the UV laser irradiated and poling-inhibited crystal surface was used to magnify the depth of the resulting domains by projecting them on the slightly inclined polished plane, which still maintains the domain sensitive differential etching property in HF acid. A shallow wedge angle of ~5º was achieved by using a special polishing jig fitted to a Logitech PM2A polishing apparatus. The stretch factor for the depth as a result of this procedure is 1/sin(5º) =11.47. The polishing compound used was a chemical-mechanical colloidal silica polishing suspension (with a pH 10.5, and particle size of 0.03μm).

In order to investigate the impact of the proximity between two adjacent PI domains on their depth, ten pairs of UV-exposed track were prepared with different centre-to-centre separations ranging from 1 μm to 10 μm. This UV laser irradiation arrangement was repeated for different laser intensities.

Figure 2.3 shows a set of SEM images of the stretched depth profiles for selected PI domain track pairs with centre to centre separations: 1 μm, 3 μm, 5 μm, 7 μm and 9 μm which were fabricated using identical UV writing conditions (laser intensity of 0.16 MW/cm^2 and writing speed of 0.1mm/s). These images suggest that there is no obvious dependence of the domain proximity on the domain depth. Similar results were observed for all UV-writing conditions.

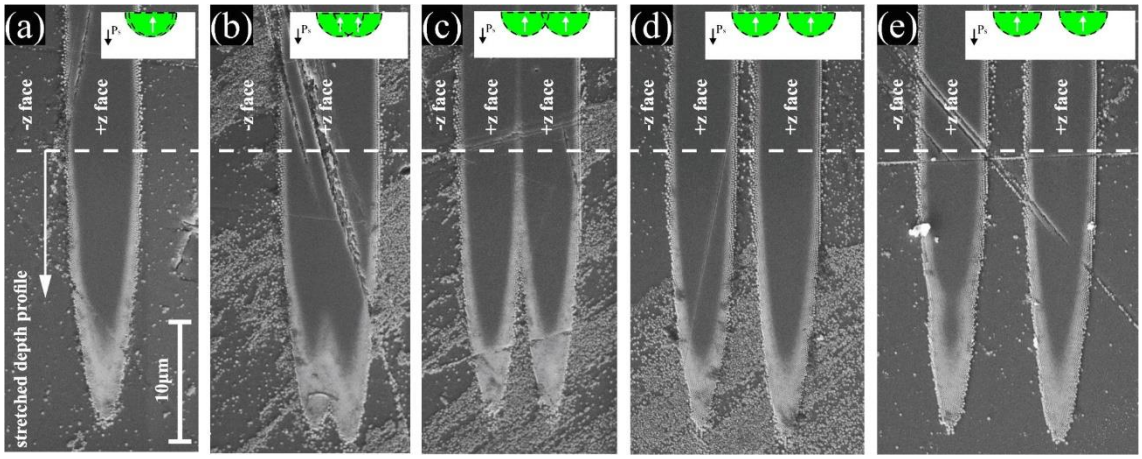

Figure 2.3 SEM images of wedge-polished/HF etched domain pairs fabricated by a UV laser beam under the same writing conditions. The centre-to-centre distances between the adjacent domains are: a) 1 μm, b) 3 μm, c) 5 μm, d) 7 μm, e) 9 μm. The dashed lines indicate the edge where the slope changes due to wedge polishing and above each stretched depth profile a schematic of the cross section of each adjacent PI domain is illustrated.

The measurements of the domain depths as a function of the domain proximity for different laser intensities are summarized in Figure 2.4. Again the results suggest that there is no indication of a specific trend. The depth fluctuations are attributed to the stochastic nature of domain growth. These results indicate the possibility of combining individual PI domains to produce larger complex domain structures.

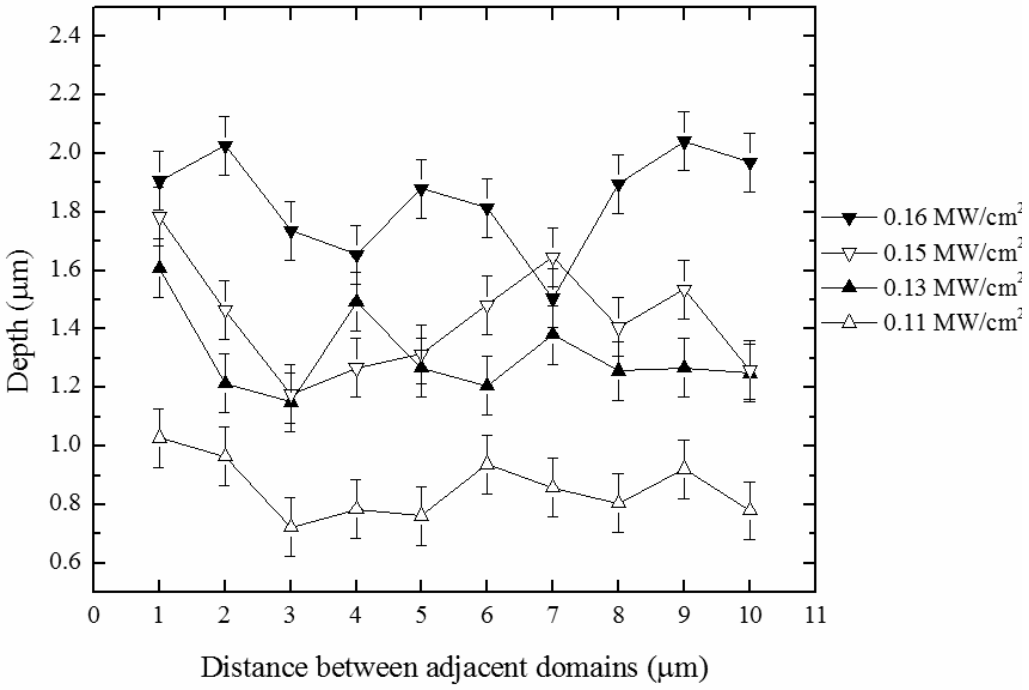

Figure 2.4 Depth of PI domain pairs as a function of the separation between UV laser exposed tracks for different irradiating laser intensities.

2.5.2 The impact of repeated exposures on the domain depth

The depth of the PI domains, as a result of a single pass laser irradiation has been investigated as a function of the irradiation conditions (laser intensity and scanning speed of the beam) in previous publications [5], [12]. Here the impact of multi-pass irradiation will be investigated in order to explore the possibility of controlling the domain depth using laser intensities that are well below the UV laser damage threshold. The number of superimposed laser tracks ranged from 1 to 4. The multi-pass exposures were repeated using different laser intensities.

Figure 2.5 shows SEM images of a set of wedge-polished cross sections of PI domains generated by superimposed UV laser irradiated tracks ranging from a single track (a) to 4 superimposed irradiated tracks (d). The individual UV laser exposures were performed at UV laser intensity of 0.16 MW/cm^2. These images show that the domain depth increases with repeated exposures, which is an encouraging result suggesting some degree of domain depth control without risk of damaging the crystal surface.

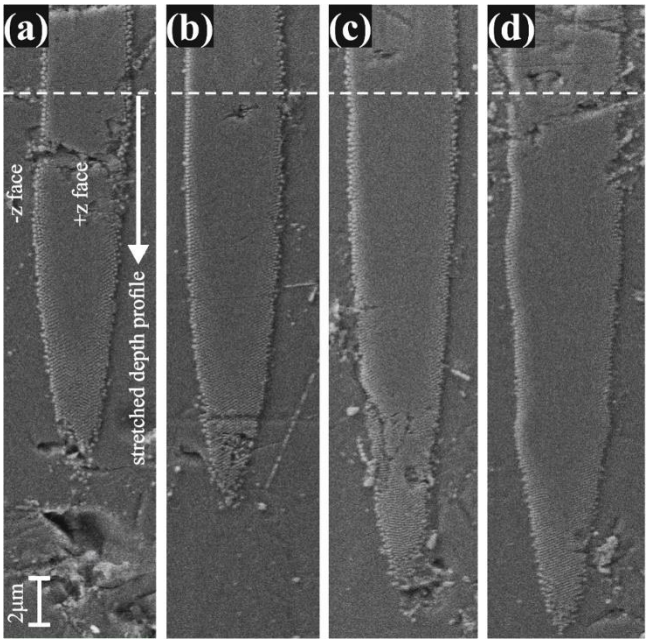

Figure 2.5 SEM images of wedge-polished and HF etched domains fabricated by repeated laser irradiated tracks along the same area. From left to right the numbers of superimposed laser tracks are: a) 1, b) 2, c) 3 and d) 4. The horizontal dashed lines indicate the position where the slope changes due to wedge polishing

A summary of the multi-pass poling inhibition results for different laser intensities is shown in the plot of Figure 2.6. These measurements show that deeper domains can be formed as a result of superimposed UV laser irradiated tracks. The domain depth increased up to 42% in the case of four passes (the maximum number of passes used in our experiments) at an intensity of 0.16 MW/cm^2. As the PI process is attributed to the migration of lithium under the influence of the temperature gradient and pyro-electric field that is being produced by the strong absorption of UV laser radiation it is expected that subsequent exposures push the lithium ions a hint further. An indication of the cumulative effect of subsequent exposures is given by the widening of the PI domain tracks that corresponds to multi pass exposures observed in Figure 2.5. However, the extension of the temperature gradients that are induced by the UV laser absorption is limited and it is expected that the domain depth increase will eventually saturate after a number of superimposed irradiations. The saturation depth is a function of the irradiating laser intensity, meaning that for lower intensities it would be shallower. This behaviour can be observed in the graph of Figure 2.6 where the depth increase that corresponds to the lowest intensity (0.10 MW/cm^2) shows signs of saturation after just 4 passes.

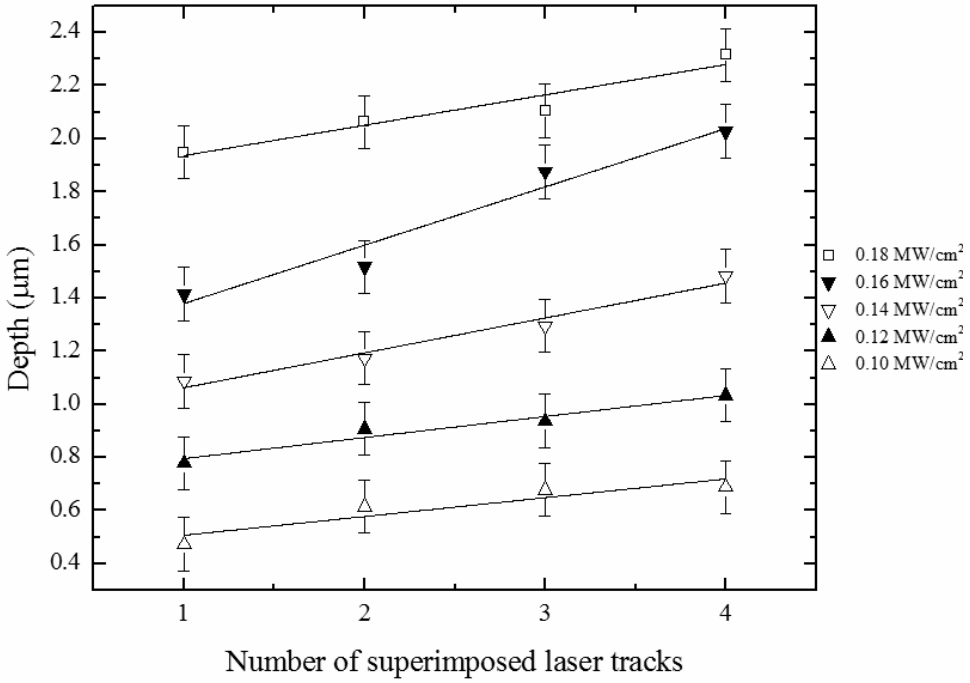

Figure 2.6 Depth versus number of superimposed laser tracks for UV-induced PI domains fabricated by a focused UV laser beam under different irradiating laser intensities.

2.5.3 Surface micro-structuring

Etching the PI domains for longer periods of time in HF acid produces surface superstructures with higher aspect ratio. The etching rate of LN, in 48% HF acid at room temperature, is ~1 μm/hr [14]. This etch rate determines the etching time, which is required to achieve the desired height of the structure. In section 2.5.1 it was shown that combining sequential offset UV laser irradiation can produce continuous larger PI domains without obvious impact on the domain depth. This combinational aspect of the PI process will be used in this section to demonstrate the ability to fabricate complex surface structures on the z-face of LN crystals, which consist of spatial arrangements of individual UV tracks. The x-y linear positioning system that was used in these experiments allowed very precise control of the laser irradiation enabling the fabrication of ring and disc structures by combining individual UV tracks. The resulting structures are shown in Figure 2.7.

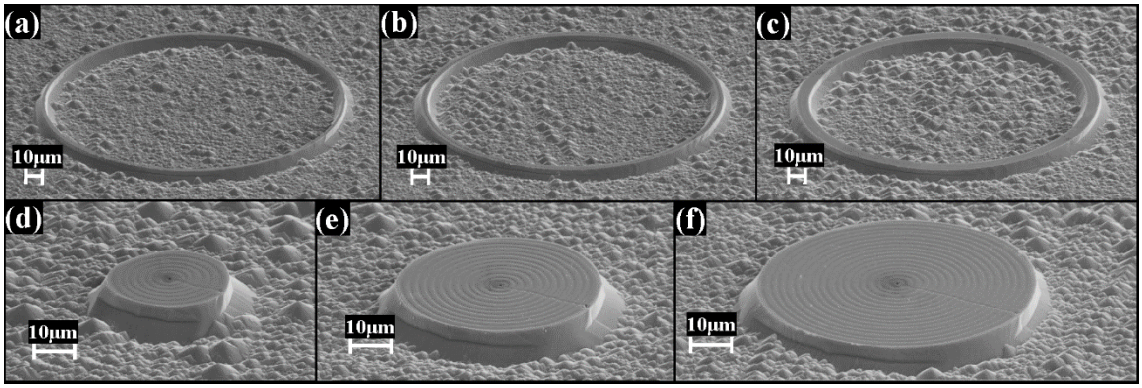

Figure 2.7 SEM images of HF-etched PI domain ring combinations that form ring shapes with variable width (images a-c) and disc structures with varying diameter (images d-f). Rings on images (a-c) consist of combinations of 1, 2 and 4 adjacent PI domains, respectively. Discs on images (d-f) consist of combinations of 7, 12 and 17 adjacent PI domains, respectively.

Each one of the rings and discs, which are shown in Figure 2.7, consists of a different number of concentric ring-shaped domains. The width of each constituent ring is fixed (~ 2.2 μm), and is a function of the width of the irradiating UV laser beam. The range of laser intensities, which have been used to fabricate these structures, was: 0.16-0.17MW/cm^2. This characteristic width represents the elementary building block for the fabrication of the composite structures and is the narrowest structure possible under these fabrication conditions. The width of the composite structure, in this case the ring or disc will be a multiple of the elementary width. The rings that are shown in Figure 2.7 consist of combinations of one (a), two (b) and four (c) adjacent PI domains while the discs consist of combinations of seven (d), twelve (e) and seventeen (f) adjacent domains. The overall width of the discs of Figure 2.7d-f is ~30 μm, 50 μm and 70 μm respectively.

PI domains can be fabricated in close proximity the precision of which is determined by the accuracy of the positioning system that is used to perform the laser irradiation step. The resultant micro-structures are always very well defined because they are a result of the etching of an inverted domain with well-defined domain boundary. Examples of the capability of this method to fabricate structures with potential photonic functionality are shown as well.

A range of different surface structures with potential photonic functionality is presented in the SEM images which are shown in Figure 2.8. Figure 2.8a shows a set of ridge Mach-Zehnder interferometer structures and Figure 2.8b shows a set of ridge coupler structures. From top left to bottom right, the distance between the two arms of the Mach-Zehnder interferometer ranges from 10 μm to 200 μm. The S-bends design that consist the Mach-Zehnder configuration used were cosine S-bends, based on theoretical works [19], [20], that show that this design exhibit the lowest loss in contrast with other. Although the S-band configuration is a controversial discussion, the choice for

this work was made without taking part on it since the first priority was to show the feasibility of the technique and the optimization was a second thought that would trouble us afterwards.

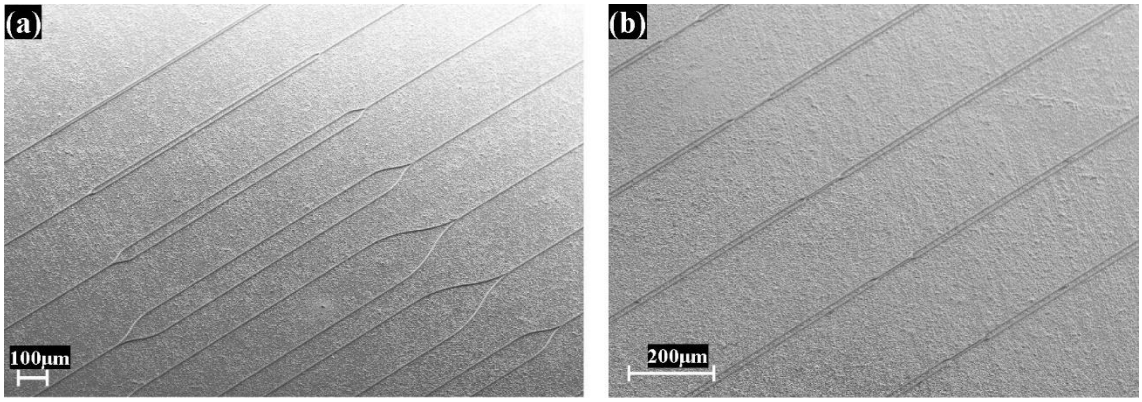

Figure 2.8 SEM images of: a) Mach-Zehnder ridge structures fabricated using 0.15 MW/cm^2 of UV laser intensity and developed from HF etching of PI domains where the distance between the two interferometer arms from top left to bottom right of the image is: 10 μm, 20 μm, 50 μm, 100 μm and 200 μm. b) Coupler structures fabricated under the same writing conditions where the minimum distance between the two arms from top left to bottom right of the image is: 2 μm, 3 μm, 4 μm, 5 μm and 6 μm.

To avoid the occurrence of effects related to translation stage backlash all UV writing relevant to these superstructures was performed in a unidirectional fashion as illustrated in Figure 2.9 where the irradiation sequence for a Mach-Zehnder structure is outlined. The writing started at x=0, tracing the cosine bend to the arm 1, then tracing the cosine bend to the output. At the end of the output channel, the beam was blocked and the stages returned to the beginning of the splitter section at point A. The mirror section (section 2) of the structure was then exposed and the writing process stopped at the merged point of the output channels.

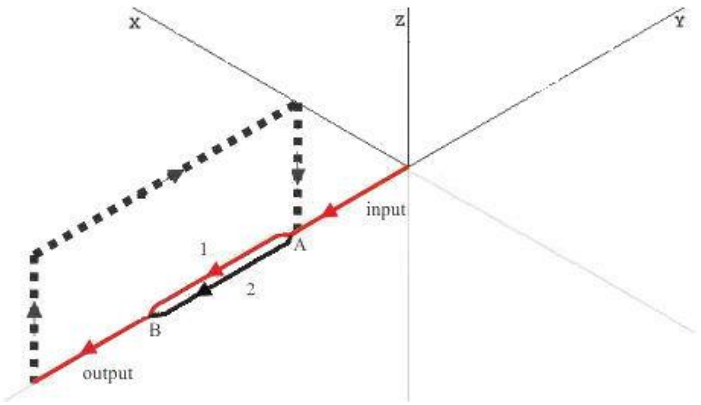

Figure 2.9 Schematic of the Mach-Zehnder structure. The red arrows dictate the direction of the first part of the interferometer, consisting the input, arm 1 and output. The black arrows indicate the second part, consisting of the movement of the stages

back to point A and the writing of arm 2 up to point B where it connects with the first section.

Therefore, the fabrication procedure for the Y-junctions, where the two ridge sections that form the branches of the Mach-Zehnder merge into a single ridge, requires overlapping of subsequently irradiated UV laser tracks because the laser writing is performed in a sequential manner. The high magnification SEM image of a Y-junction, which is shown in Figure 2.10 indicate that there is no visible impact of this particular manner of domain writing in the final structure, as the junction is smooth and continuous.

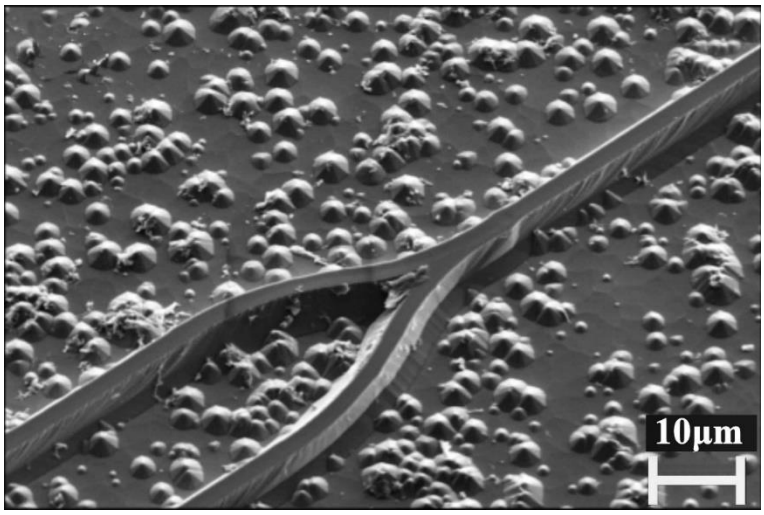

Figure 2.10 SEM image of Y-junction structure developed from HF etching of curved PI domains. The distance between the two interferometer arms is: 20 µm.

Figure 2.11 shows high magnification details of the ridge coupler structures which were shown in Figure 2.8b. The length of the coupling section in these structures is 100 µm. The centre-to-centre separation in the same section of the ridge couplers is: (a) 3 µm, (b) 4 µm and(c) 5µm thus consequently changing the gap between the two ridges as shown in Figure 2.11.

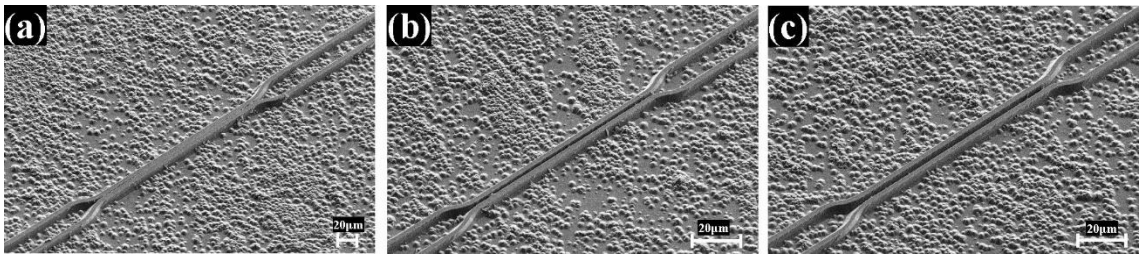

Figure 2.11 SEM images of ridge coupler structures developed from HF etching of PI domains. The distance between the two ridges in the coupler section is: a) 3 µm, b) 4 µm and c) 5 µm.

Lastly, in Figure 2.12a, the distance between the ring and channel structures is 2 μm resulting in overlap. This overlap is significantly reduced when the distance between them is 4 μm as shown in Figure 2.12b.

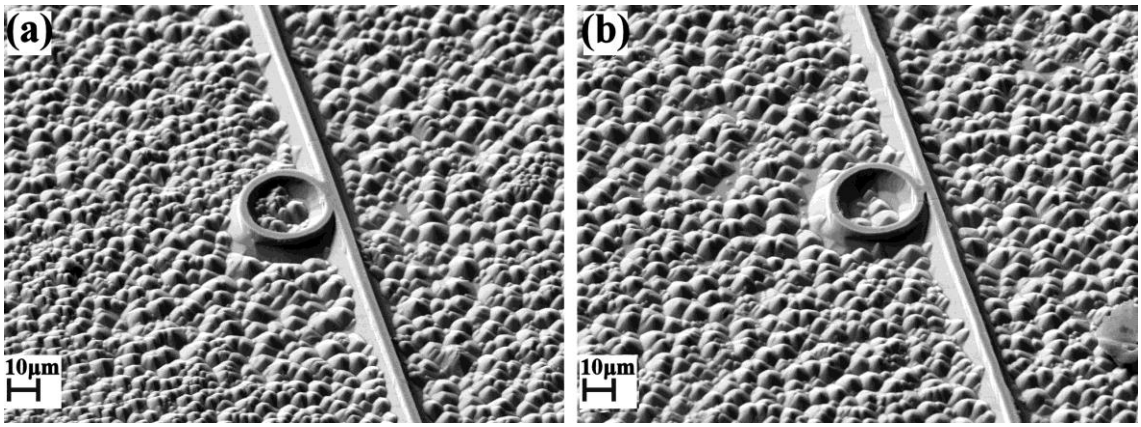

Figure 2.12 SEM images of ring-shaped superstructure near a straight ridge section fabricated using 0.14 MW/cm^2 of UV laser intensity. The distance between the centres of the ring and straight ridge sections is: a) 2 μm, b) 4 μm.

The rough surface background that surrounds the ridges is a consequence of the etching of the planar –z polar surface of the crystal and is characteristic of etching in high concentration HF acid. The rough background is not expected to produce any scattering loss to a waveguide mode that is confined to the top of the ridge; however it can have a negative effect in the fabrication of auxiliary structures such as electrodes etc. Significant reduction of the –z face roughness can be achieved in special mixtures of HF-HNO_3 and ethanol[21]. Further smoothening of any residual roughness can be achieved by surface tension reshaping which can be achieved by annealing the crystal at temperatures close to the melting point[22]. Thermal treatment can produce ultra-smooth surfaces with low scattering loss, while maintaining the crystalline properties of the LN.

2.6 Acoustic Superlattice transducers for SAW generation by poling inhibition

Acousto-optic effects in piezoelectric optical crystals has led to the development of devices such as optical modulators/switches deflectors, frequency shifters, to name a few, which are routinely used for applications in optical telecommunications [23] and biomedical sensing [24]. The acoustic wave that is responsible for the AO interaction is usually generated by an AC field applied via interdigitated transducers deposited on piezoelectric substrates. In this way it is possible to generate surface acoustic waves which if overlapped with optical waveguides they can modify the way that

light propagates in them. However, the metallic electrodes constituting the IDTs that covers the optical waveguide produces an increase in optical losses [25]. Recently, a new approach for SAW excitation has been reported, using periodically poled lithium niobate (PPLN) in combination with coplanar RF electrodes, the so-called acoustic superlattice (ASL) [26] which allows the propagation of the optical wave through an electrode-free path. As UV-laser induced poling inhibition offers an alternative approach for domain engineering in LN, here we will apply this technique in order to generate SAWs through the use of a piezoelectric acoustic superlattice.

2.6.1 Background

ASL structures are based on ferroelectric crystals with periodically inverted domains where by the use of uniform electrodes, instead of periodic electrodes, as in IDTs, acoustic waves can be generated by the modulated piezoelectric response of the material as a result of the periodic ferroelectric domain orientation. Because of the domain inversion, all odd rank tensors like the piezoelectric tensors switch sign, while all even tensors like refractive index remain unaltered. Therefore, by applying a uniform electric field, a periodic strain arises as a result of the periodic change of piezoelectric coefficient generating an elastic wave. As demonstrated in [27] the SAW frequency is inversely proportional to the period of the domain-inverted gratings which presents an advantage in comparison with IDTs. This is because in ASLs the wavelength of the elastic perturbation is given by the period Λ of the domain grating ($\lambda_R = \Lambda$), whereas in IDTs is $\lambda_R = 2\Lambda$. The expression of the acoustic frequency f_R is:

$$f_R = v_R / \lambda_R \qquad 2\text{-}1$$

where, v_R is the SAW velocity. That means that for the same grating period, the operating frequency of the ASL is twice the frequency that can be achieved by IDT. Typical velocities of acoustic waves range from 3000m/s to 6000m/s for ferroelectric crystals as LN [28]. A schematic illustration of the ASL transducer which was proposed in [27] is shown in Figure 2.13. In the schematic Λ is the period of the lattice, $L_e=N\Lambda$ is the total length, W_L and W_R the left and right electrode width and W_G the width of the gap between the two electrodes.

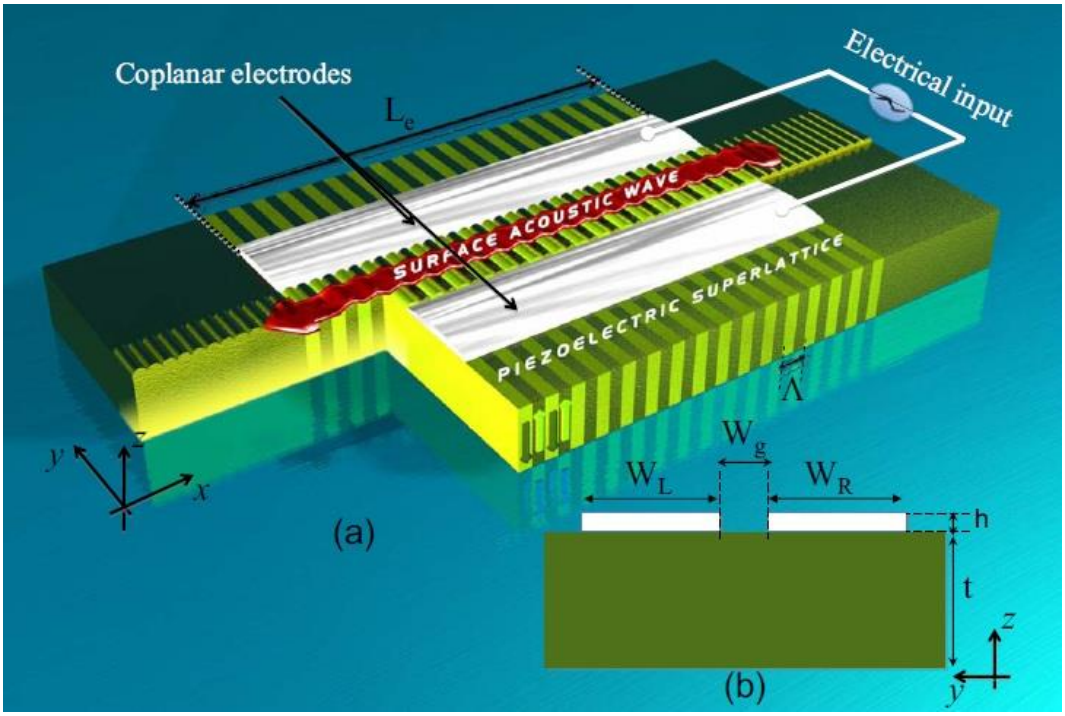

Figure 2.13 a) Schematic of the basic structure of ASL based transducer in PPLN with coplanar electrodes configuration. b) Side-view (yz-plane). Reprinted from Ref. [27].

The fabrication procedure of ASL structure is achieved using the standard lithography process followed by EFP on a 500μm thick z-cut LN substrate. Lattice periods that have been tested are between 15μm and 25μm, but the overall length is 10mm for all cases. Subsequently, a pair of aluminium coplanar electrodes with thickness of h=0.2μm is deposited on the x direction upon the ASL using lithography as well. The gap width W_G between the electrodes is 100μm and the electrode width W_L, W_R 100μm. Several overall lengths have been investigated (4-10mm) also. For such a configuration with a period Λ=15 μm and total length of L_e=10 mm on a 500 μm thick LN substrate, the expected resonance frequency is about 253 MHz for a SAW velocity of 3795 m/s [29].

The bulk nature of the ferroelectric linear lattice is not however a strict requirement because the coplanar character of the electrodes means that the electric field rapidly decays in strength with depth. Here the use of surface domain gratings is proposed to substitute the bulk domains that have been used in the ICFO demonstrators. The surface domains that can be manufactured using UV laser induced PI have a depth of a few microns below the surface of the crystal which should be sufficient for the generation of SAWs. The modified device is illustrated in Figure 2.14.

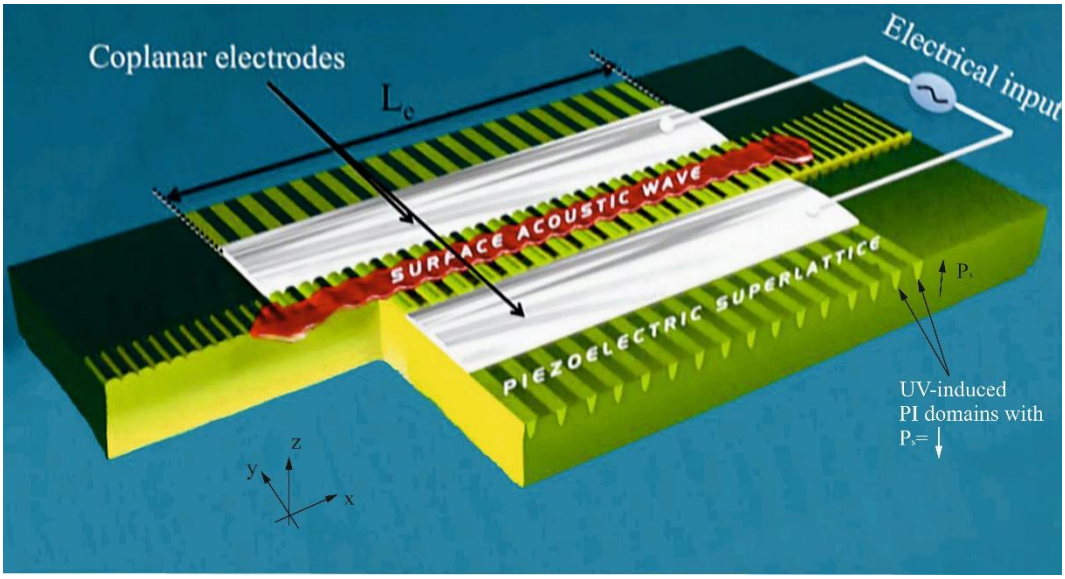

Figure 2.14 Schematic of the basic structure of an ASL transducer using a PI domain grating in lithium niobate with coplanar electrodes.

PI domains offer additional flexibility regarding the departure from crystallographic limitations that apply to the formation of bulk domains using E-field poling and produces finer domain periods that will shift the performance of these devices to even higher frequencies.

2.6.2 Experimental procedure

The ferroelectric domain gratings were fabricated using the PI experimental procedure as shown in section 2.2. The spot size of the irradiated laser beam was ~2 μm and the laser intensities were ranging from 0.10 MW/cm^2 to 0.16 MW/cm^2. Two different domain grating periods, 10 μm and 20 μm, were produced with domain length of 200 μm. Figure 2.15 shows optical microscopy images of fabricated UV-induced PI gratings with period of 10 μm with UV different laser intensities: a) 0.10 MW/cm^2, b) 0.12 MW/cm^2, c) 0.14 MW/cm^2 and d) 0.16 MW/cm^2. In the end of the process, all the samples were briefly etched in a HF solution concentration for 30 sec in order to reveal the inverted domains. Revealing the domains was performed for making easier the alignment in the lithography process for electrode fabrication.

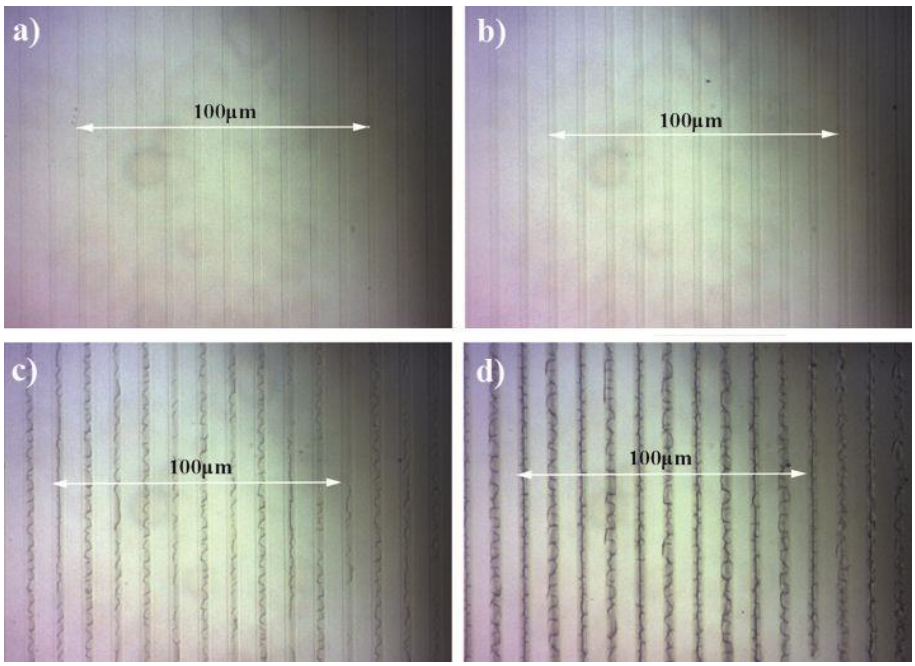

Figure 2.15 Microscope images of fabricated UV-induced PI gratings of period of 10µm with different UV laser powers: a) 0.10MW/cm^2, b) 0.12MW/cm^2, c) 0.14MW/cm^{2}and d) 0.16MW/cm^2. a) and b) are solid domain with no laser damaged surface. c) and d) are solid domains with laser-damaged surface.

The feasibility of direct SAW excitation on PI domain based ASL transducers devices is a work still on progress and will be assessed by RF excitation measurements using a network analyser to detect the RF reflection parameters as a function of the excitation frequency. These measurements will be performed by the group at ICFO - The Institute of Photonic Sciences in Barcelona, which is being collaborating with us.

2.7 Conclusions

The ability to fabricate large composite domain structures in LN crystals that consist of a spatial arrangement of individual PI domains has been demonstrated. The individual PI domains are thus used as elementary building blocks to compose larger arbitrary continuous domain structures. The individual PI domains correspond to spatially selective UV irradiation of the +z face of the crystal, which is performed in a sequential manner along tracks with width defined by the UV laser beam spot size. It was shown that the proximity between adjacent UV irradiated tracks does not affect the depth of the corresponding individual or composite PI domains. However, repeated UV irradiation along the same track was shown to result in some moderate depth increase. More specifically, the domain depth can be increased up to 42% in the case of four passes while using laser intensity of 0.16 MW/cm^2. This significant change of the depth thus can provide a better degree of

control of individual domain depth. Irrespective of their depth the PI composite domains can be used as an etch stop layer when the crystal is subjected to HF acid etching. The utility of this method for the fabrication of structures with potential photonic functionality was demonstrated by using combinations of individual PI domain tracks to produce, after HF differential etching, superstructures such as rings, discs, as well as ridge Mach-Zehnder and coupler structures.

2.8 References

[1] C. L. Sones, a. C. Muir, Y. J. Ying, S. Mailis, R. W. Eason, T. Jungk, Á. Hoffmann, and E. Soergel, "Precision nanoscale domain engineering of lithium niobate via UV laser induced inhibition of poling," *Appl. Phys. Lett.*, vol. 92, no. 7, 2008.

[2] H. Steigerwald, M. Lilienblum, F. von Cube, Y. J. Ying, R. W. Eason, S. Mailis, B. Sturman, E. Soergel, and K. Buse, "Origin of UV-induced poling inhibition in lithium niobate crystals," *Phys. Rev. B*, vol. 82, no. 21, p. 214105, 2010.

[3] F. Johann, Y. J. Ying, T. Jungk, A. Hoffmann, C. L. Sones, R. W. Eason, S. Mailis, and E. Soergel, "Depth resolution of piezoresponse force microscopy," *Appl. Phys. Lett.*, vol. 94, no. 17, p. 172904, 2009.

[4] A. C. Muir, G. J. Daniell, C. P. Please, I. T. Wellington, S. Mailis, and R. W. Eason, "Modelling the formation of optical waveguides produced in $LiNbO_3$ by laser induced thermal diffusion of lithium ions," *Appl. Phys. A*, vol. 83, no. 3, pp. 389–396, 2006.

[5] C. Y. J. Ying, G. J. Daniell, H. Steigerwald, E. Soergel, and S. Mailis, "Pyroelectric field assisted ion migration induced by ultraviolet laser irradiation and its impact on ferroelectric domain inversion in lithium niobate crystals," *J. Appl. Phys.*, vol. 114, no. 8, p. 083101, 2013.

[6] S. Mailis, C. Riziotis, P. G. R. Smith, J. G. Scott, and R. W. Eason, "Continuous wave ultraviolet radiation induced frustration of etching in lithium niobate single crystals," *Appl. Surf. Sci.*, vol. 206, no. 1–4, pp. 46–52, 2003.

[7] P. Ganguly, C. L. Sones, Y. Y. Ying, H. Steigerwald, K. Buse, E. Soergel, R. W. Eason, and S. Mailis, "Determination of refractive indices from the mode profiles of UV-written channel waveguides in $LiNbO_3$ - crystals for optimization of writing conditions," *Light. Technol. J.*, vol. 27, no. 16, pp. 3490–3497, 2009.

[8] I. E. Barry, G. W. Ross, P. G. R. Smith, R. W. Eason, and G. Cook, "Microstructuring of lithium niobate using differential etch-rate between inverted and non-inverted ferroelectric domains," no. 98, pp. 246–254, 1998.

[9] C. Sones, S. Mailis, V. Apostolopoulos, I. E. Barry, C. Gawith, P. G. R. Smith, and R. W. Eason, "Fabrication of piezoelectric micro-cantilevers in domain-engineered $LiNbO_3$ single crystals," *Journal of Micromechanics and Microengineering*, vol. 12, pp. 53–57, 2002.

[10] C. L. Sones, P. Ganguly, C. Y. J. Ying, E. Soergel, R. W. Eason, and S. Mailis, "Poling-inhibited ridge waveguides in lithium niobate crystals," *Appl. Phys. Lett.*, vol. 97, no. 15, p. 151112, 2010.

[11] D. Yudistira, A. Boes, A. R. Rezk, L. Y. Yeo, J. R. Friend, and A. Mitchell, "UV direct write Metal Enhanced Redox (MER) domain engineering for realization of surface acoustic devices on Lithium Niobate," *Adv. Mater. Interfaces*, vol. 1, no. 4, 2014.

[12] C. L. Sones, a. C. Muir, Y. J. Ying, S. Mailis, R. W. Eason, T. Jungk, Á. Hoffmann, E. Soergel, and A. Hoffmann, "UV laser radiation inhibits domain inversion in lithium niobate," *Appl. Phys. Lett.*, vol. 92, no. 7, p. 072905, 2008.

[13] V. Gopalan, T. E. Mitchell, and K. E. K. Sicakfus, "Switching kinetics of 180° domains in congruent $LiNbO_3$ and $LiTaO_3$ crystals," *Solid State Commun.*, vol. 109, no. 2, pp. 111–117, 1998.

[14] C. L. Sones, S. Mailis, W. S. Brocklesby, R. W. Eason, and J. R. Owen, "Differential etch rates in z-cut $LiNbO_3$ for variable HF/HNO_3 concentrations," *J. Mater. Chem.*, vol. 12, no. 2, pp. 295–298, 2002.

[15] C. Y. J. Ying, a. C. Muir, C. E. Valdivia, H. Steigerwald, C. L. Sones, R. W. Eason, E. Soergel, and S. Mailis, "Light-mediated ferroelectric domain engineering and micro-structuring of lithium niobate crystals," *Laser Photon. Rev.*, vol. 6, no. 4, pp. 526–548, 2012.

[16] C. L. Sones, P. Ganguly, Y. J. Ying, F. Johann, E. Soergel, R. W. Eason, and S. Mailis, "Spectral and electro-optic response of UV-written waveguides in $LiNbO_3$ single crystals," *Opt. Express*, vol. 17, no. 26, pp. 23755–64, 2009.

[17] V. Gopalan, T. E. Mitchell, Y. Furukawa, and K. Kitamura, "The role of nonstoichiometry in 180° domain switching of $LiNbO_3$ crystals," *Appl. Phys. Lett.*, vol. 72, no. 16, p. 1981, 1998.

[18] V. Gopalan, T. E. Mitchell, and K. E. Sicakfus, "Switching kinetics of 180° domains in congruent $LiNbO_3$ and $LiTaO_3$ crystals," *Solid State Commun.*, vol. 109, no. 2, pp. 111–117, 1998.

[19] F. J. Mustieles, E. Ballesteros, and P. Baquero, "Theoretical S-bend profile for optimization of optical waveguide radiation losses," *IEEE Photonics Technol. Lett.*, vol. 5, no. 5, pp. 551–553, 1993.

[20] A. Kumar and S. Aditya, "Performance of S-bends for integrated-optic waveguides," *Microw. Opt. Technol. Lett.*, vol. 19, no. 4, pp. 289–292, 1998.

[21] H. Hu, R. Ricken, W. Sohler, and R. B. Wehrspohn, “Lithium Niobate Ridge Waveguides Fabricated by Wet Etching,” *Photonics Technol. Lett. IEEE*, vol. 19, no. 6, pp. 417–419, 2007.

[22] C. Y. J. Ying, C. L. Sones, A. C. Peacock, F. Johann, E. Soergel, R. W. Eason, M. N. Zervas, and S. Mailis, “Ultra-smooth lithium niobate photonic micro-structures by surface tension reshaping,” *Opt. Express*, vol. 18, no. 11, pp. 11508–13, 2010.

[23] Y. N. Korkishko and V. a. Fedorov, “Relationship between refractive indices and hydrogen concentration in proton exchanged $LiNbO_3$ waveguides,” *J. Appl. Phys.*, vol. 82, no. 3, p. 1010, 1997.

[24] K. Gallo, Corin B.E Gawith, J. Prawiharjo, N.G.R. Broderick, P. Smith, S. Mailis, R.W.Eason, D.J. Richardson, "UV-written channel waveguides in proton-exchanged lithium niobate," in *Lasers and Electro-Optics (CLEO). Conference*, 16-21 May 2004

[25] D. Yudistira and D. Janner, “Integrated acoustic and acousto-optic filters using domain inversion,” vol. 1, pp. 3–4.

[26] D. Yudistira, D. Janner, S. Benchabane, V. Pruneri, I. D. C. Fotoniques, and M. T. Park, “Integrated acoustic and acousto-optic superlattices filters based on domain inverted $LiNbO_3$: modeling , design and experimental validation,” vol. 112, no. 1999, pp. 107–112, 2004.

[27] D. Yudistira, S. Benchabane, D. Janner, and V. Pruneri, “Surface acoustic wave generation in ZX-cut $LiNbO_3$ superlattices using coplanar electrodes,” *Appl. Phys. Lett.*, vol. 95, no. 5, p. 052901, 2009.

[28] D. Yudistira, “Micro-structured ferroelectric superlattice for efficient acousto-optic devices,” PhD thesis, *Technical University of Catalonia*, 2012

[29] D. Yudistira, D. Janner, S. Benchabane, and V. Pruneri, “Integrated acousto-optic polarization converter in a ZX-cut $LiNbO_3$ waveguide superlattice.,” *Opt. Lett.*, vol. 34, no. 20, pp. 3205–7, 2009.

Chapter 3: Local enhancement of the electro-optic coefficient in poling inhibited CLN channel waveguides.

3.1 Introduction

Lithium niobate crystal is widely used in the photonics industry due to its large 2^{nd} order optical nonlinearity and wide transparent window. Its significant electro-optic response also enables the fabrication of low-voltage operation, high speed integrated optical modulators that are routinely used in optical telecommunication and integrated optics. Channel waveguides are the basic elements of integrated optical circuits which are commonly fabricated by Ti-diffusion or proton exchange in LN [1]. Recently, a UV laser method for direct writing of optical channel waveguides has been reported [2], which is suitable for rapid prototyping of photonic devices. The UV laser written channel waveguide characteristics as a function of the fabrication conditions and their electro-optic (EO) performance can be found in [3] and [4] respectively.

Since its inception, the UV directly written waveguide procedure has held considerable promise because of its single-step nature, which is well suited for the fabrication complex micro-optical devices where photolithography for waveguide fabrication becomes challenging [5]. The formation of UV-written waveguides is attributed to the high optical absorption of CLN at ultraviolet wavelengths, which produce steep temperature gradients in the vicinity of the laser irradiated portion of the crystal's surface [6]. Side-diffusion of lithium then takes place under the influence of the temperature gradients, which produces local fluctuations of the concentration of lithium ions that change the value of the extra-ordinary index of refraction locally [7]. This temperature gradient driven diffusion process has been modelled in [6]. Lasers which are operating at wavelengths within the absorption bandwidth of lithium niobate can be used for this purpose; however, it was found that irradiation at wavelengths shorter than 270 nm preserve the important electro-optic response of the processed crystal while longer wavelengths result in degradation of the electro-optic response [3].

The UV irradiation, which is responsible for the waveguide formation, has further consequences on the ferroelectric state of the crystal. It was found that UV laser irradiation leads to direct poling, domain inversion without the application of an external electric field E_f, on the –z and on other non-polar surfaces [8] and can also cause poling inhibition on the +z polar face of the crystal [9]. The latter method produces isolated domain structures that maintain the original domain orientation after uniform poling of the sample, which correspond to the UV irradiated patterns.

Both directly poled and pole inhibited domains have limited depth (typically a few microns) hence these domain engineering tools are suitable for nonlinear optical interactions in waveguides rather than bulk structures as the waveguide propagating modes overlap significantly with individual ferroelectric domains. The poling inhibition effect is schematically illustrated in Figure 3.1 where the step-by-step formation of the photonic structure is shown. In this chapter a ~ 36.7 % enhancement of the electro-optic response is demonstrated when light propagates through a UV written channel waveguide with an overlapping PI domain fabricated in a congruent LN single crystal.

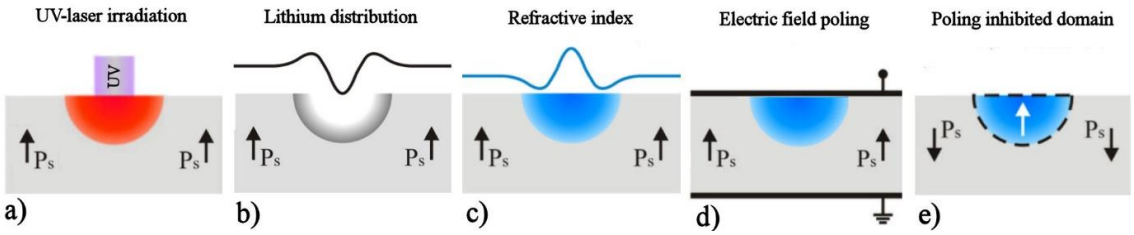

Figure 3.1 Schematic of the cross section of a) the LN crystal during the UV-irradiation process on its +z face where the red region indicates the UV-induced temperature increased volume, b) the lithium ions distribution upon the irradiated region, c) the resulted UV-written waveguide on a single domain substrate where the blue line indicates the refractive index distribution, c) the EFP step and d) the formed PI domain which overlaps with the waveguide.

3.2 Waveguide/domain fabrication process

The single crystal substrates, which were used in the experiments were diced out of a 0.5 mm thick z-cut CLN wafers from Crystal Technology, Inc. (US). Direct laser writing on LN was performed using the setup described in section 2.2, using a Coherent Innova Sabre 300C frequency-doubled (FreD) argon ion laser that delivered continuous wave (CW) output at 244 nm wavelengths. The +z face of the LN crystal sample was irradiated by the UV laser beam, which was focussed down to a spot size of ~ 4.2 μm. The focussed laser beam was scanned across the sample surface using a computer-controlled 2D translation stage, along the crystallographic y-axis at different laser powers. The scanning speed used was constant at 0.1 mm/sec. The power of the UV laser was within the range of 30-50 mW that depending on the chosen spot size corresponds to a range of intensities between 0.10 MW/cm^2 and 0.18 MW/cm^2. The selected range of intensities produced waveguides that were largely free from surface damage. However, some limited surface damage was observed in waveguides that were written at the higher end of the intensity range.

Following UV laser irradiation the crystal is subjected to domain inversion by the application of a uniform electric field along the z direction. More specifically, a slow forward poling was conducted at the lowest possible poling voltage. The poling voltage was ramped at a rate of 5Vsec^{-1}

until domain nucleation was observed and then was kept at that level until the poling process was completed. The final value of the applied electric field that was used for domain inversion was ~19.5kV/mm ± 0.1 kV/mm.

Finally, the irradiated and poled samples were end-face polished to enable coupling of light. Good end-face quality is required to enable efficient optical coupling and therefore, accurate measurement of the electro-optic coefficient. The end-face polishing was achieved using a Logitech polishing machine (PM2A) and a chemo-mechanical colloidal silica polishing suspension (with a pH 10.5, and particle size of 0.03 μm), until no defects were visible under inspection with an optical microscope. In order to perform EO measurements on the domain engineered channel waveguide sample it is necessary to apply an electric field along the z-axis of the crystal. For the purpose of these low frequency EO experiments we deposited metallic electrodes with by sputtering a pair of thin (~20 nm) gold films onto the two opposite z-faces of the waveguide substrate, which completed the fabrication process. The length of these electrodes was 5 mm. A schematic of the sample, ready for an EO measurement can be seen in Figure 3.2.

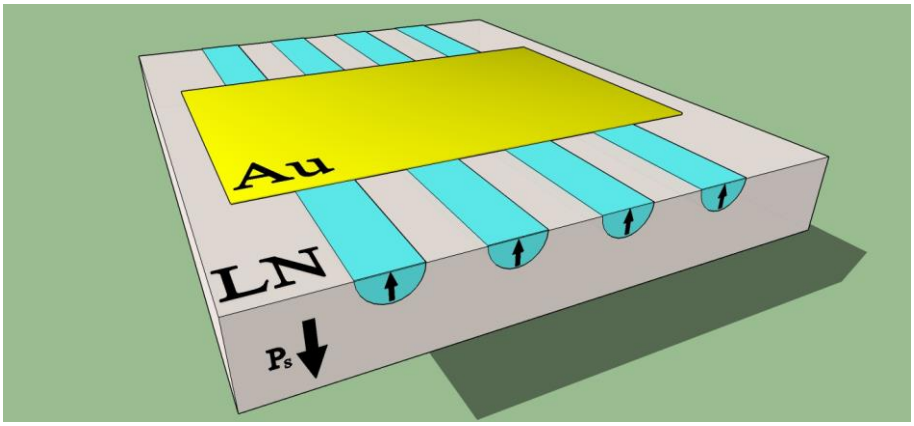

Figure 3.2 Schematic of the PI domains overlapping with the UV-written waveguides (cyan regions) in a LN crystal where gold electrodes have been deposited on the z faces (yellow area). The arrows indicate the polarity

3.3 Superposition of a waveguide channel with an inverted domain

As discussed in Chapter 2, the result of the application of the uniform electric field after the UV laser irradiation is uniform domain inversion of the crystal apart from a shallow volume immediately below the UV irradiated track. The size of this isolated domain that maintains the initial polarity of the crystal is comparable to the size of the n_e distribution that constitutes the waveguide. Actually both effects have the same origin and are relating to a local change in the stoichiometry (variation of the lithium concentration) caused by the local laser heating. In general, the quality and size of PI domains is a function of the irradiation conditions, namely the intensity and dwell time of

the beam which is controlled by the spot size/power and scanning speed respectively. However, in our case it is only dependant on the writing power used since the writing speed was constant. Within the range of laser intensities (0.10-0.20 MW/cm^2) which have been used for the fabrication of PI domains the lower intensity extreme (0.10-0.12 MW/cm^2) produced PI domains regions, which are discontinuous consisting of densely packed nano-domains while the higher intensity extreme (0.16-0.18 MW/cm^2) typically resulted in severe surface damage, which is undesirable for the fabrication of photonic devices as it can cause significant scattering loss. The impact of the irradiating laser intensity on the PI domain size is much more significant as compared with the impact of the dwell time [10]. The maximum depth of the PI domains fabricated with beam spot size of ~ 3 μm was slightly over 4 μm, however a surface damage free, solid PI domain has a depth of ~ 2.5 μm.

An increase of the ordinary refractive index in a newly poled region as a consequence of EFP has been reported before, measured by digital holography [11] and scanning near-field optical microscopy [12]. This increase has been attributed to an internal field, which originates from the presence of frustrated defect clusters in the newly inverted domain region. In the case of PI domain/waveguide structures such a background refractive index increase would reduce the refractive index difference between the core and cladding thus resulting in weaker guiding. It has been however observed that PI waveguide structures show an overall increase in the extraordinary refractive index contrast between core and cladding [13]. As the PI waveguides are surrounded by a domain walls we believe that the surrounding domain wall is responsible for this effect. Interestingly an increase of the ordinary refractive index in the vicinity of a domain wall has been reported in [12].

A comparison of the maximum extraordinary refractive index contrast for waveguides written using different UV laser intensities before and after the EFP is shown in Figure 3.3.

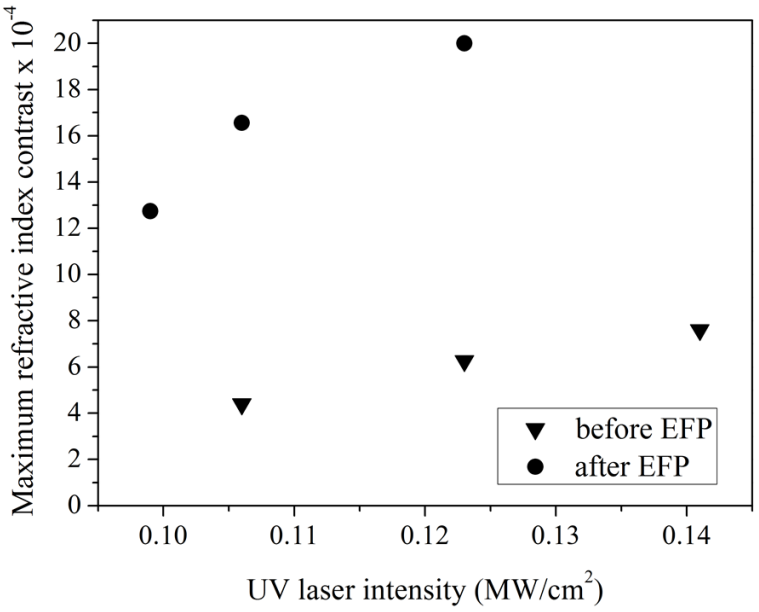

Figure 3.3 Plot of Peak Δn_e as a function of waveguide writing intensity before and after. Reprinted from [13].

It is important to mention at this point that the irradiation conditions for the writing of the channel waveguides and for the formation of the PI domains are within the same range [14], which is expected as both of them have the same physical origin.

3.4 Experimental arrangement for EO measurements

The electro-optic response of the resulting domain engineered channel waveguides was measured using a free space Mach-Zehnder interferometer a schematic of which is shown in Figure 3.4. The domain engineered waveguides which are investigated here are single mode at λ=633 nm hence a He-Ne laser was used as the light source in the setup. The laser beam is divided into the two arms of the interferometer using a cube beam-splitter. The signal arm of the interferometer contains the waveguide sample under investigation. A 10× microscope objective (with a numerical aperture (NA) of 0.25) lens was used to couple light into the waveguide channels and another 40× microscope objective lens (NA=0.65) was used to collect and re-collimate the output from the waveguide. Optical attenuators (variable neutral density filters) were used to balance the optical power transmitted through the individual arms of the interferometer in order to improve the visibility of interference fringes. The re-collimated signal beam was mixed with the beam coming from the reference arm of the interferometer using a second cube beam splitter. The polarization of the He-Ne laser was adjusted to access the extraordinary index of the crystal samples. The interference fringe pattern was then expanded using a third microscope objective lens (20×) and the phase variations between the signal and the reference were monitored by detecting the power variations of light transmitted through a pinhole with diameter of ~ 25 μm using a Si photodiode. The detection arrangement is shown in the schematic of the setup that is presented in Figure 3.4. The phase variation is of course electro-optically induced by applying a voltage between the two electrodes of the waveguide sample. An optical chopper (frequency: ~ 170 Hz) in conjunction with a lock-in-amplifier was used to improve the signal-to-noise ratio of the detection system. Finally, the interferometer setup was vibration isolated and covered to prevent phase noise originating from mechanical vibrations and air currents respectively. LabVIEW code was used to control the application of voltage and to collect the data.

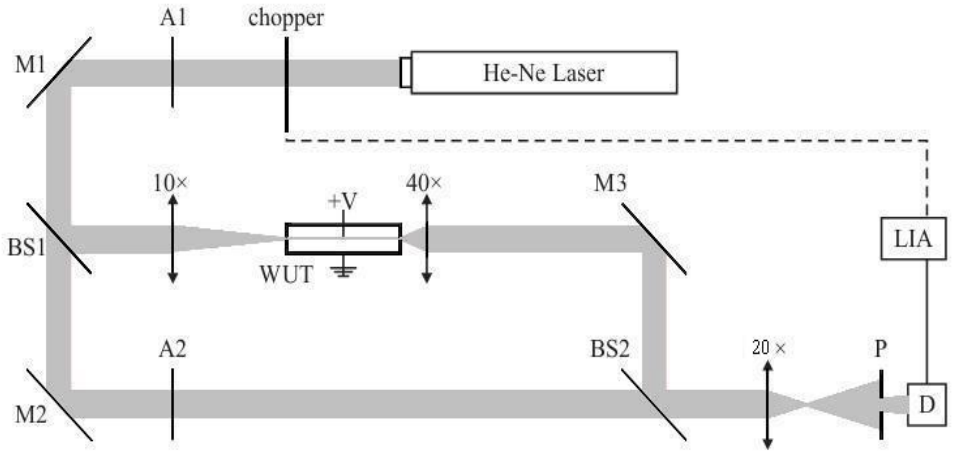

Figure 3.4 Experimental setup for the measurement of electro-optic coefficient of the PI lithium niobate waveguides: A1, A2 correspond to optical attenuators; M1, M2, M3 are mirrors; BS1, BS2 are cube beam splitters; WUT the "waveguide under test"; V the applied voltage; P the pinhole; D the detector and LIA the lock-in amplifier.

Once the sample was mounted into the signal branch of the interferometer, a waveguide was located and then the coupling of the beam was optimized. The waveguide coupling arrangement was visually inspected using a stereo-microscope. The experiment was repeated for a number of waveguides written with different writing conditions.

The EO coefficient of the domain engineered channel waveguides was calculated by using the phase variation data and these values were compared to the EO coefficient obtained from a Ti-diffused LN channel waveguide using the same experimental setup. The electro-optic response of the Ti-diffused waveguides is known to be the same as that of the bulk crystal [15], therefore the Ti-diffused waveguide was used not only as a reference sample but also in order to test the integrity of the experimental setup. A voltage ramp, which was applied between the electrodes deposited on the waveguides, was varied slowly (5 Volts/sec) ranged from -600 V to +600 V (at room temperature) corresponding to a uniformly applied electric field ranging from -1.2 to +1.2 V/μm along the z-axis of the LN crystal. Within this range of applied electric fields more than a full fringe variation could be detected, corresponding to a 2π phase shift, and was recorded. The half-wave voltage V_π, (i.e. the voltage required to produce an electro-optic phase shift of 180°) was extracted from the measurements after the experimental data were processed. The electro-optically induced refractive index change in the particular geometry for the application of the electric field (along the z-axis) is given by:

$$\Delta n_e(E_3) = \frac{1}{2} r_{33} n_e^3 E_3 \qquad 3\text{-}1$$

where n_e is the extraordinary refractive index and r_{33} the relevant element of the electro-optic tensor. The electro-optic phase shift that was measured by monitoring the movement of the interference fringes in the output of the interferometer as a function of the voltage applied to the sample and the effective EO coefficient (r_{33}) of the domain engineered waveguides was then calculated using the expression [16], [17]:

$$r_{33} = \frac{\lambda d}{n_e^3 L V_\pi} \qquad 3\text{-}2$$

where L is the length of the channel waveguide, which is covered by the electrode, and d is the thickness of the waveguide substrate which is 500 μm. Eq. 3-1 assumes 100% overlap of the applied electric field with the waveguide propagation mode, which is a valid approximation in the present configuration [18]. No phase drift due to optical "photorefractive damage" was observed over the duration of the measurements.

3.5 Results and discussion

Typical variations of the measured detector output with applied voltage are presented in Figure 3.5, where a sinusoidal function is fitted to the data points. These data values were collected by ramping the voltage, applied to the z-face electrodes of the sample from 0 to -600 V and from 0 to +600 V. The waveguide used in this occasion was written under laser intensity of 0.18 MW/cm^2 and writing speed of 0.1 mm/sec.

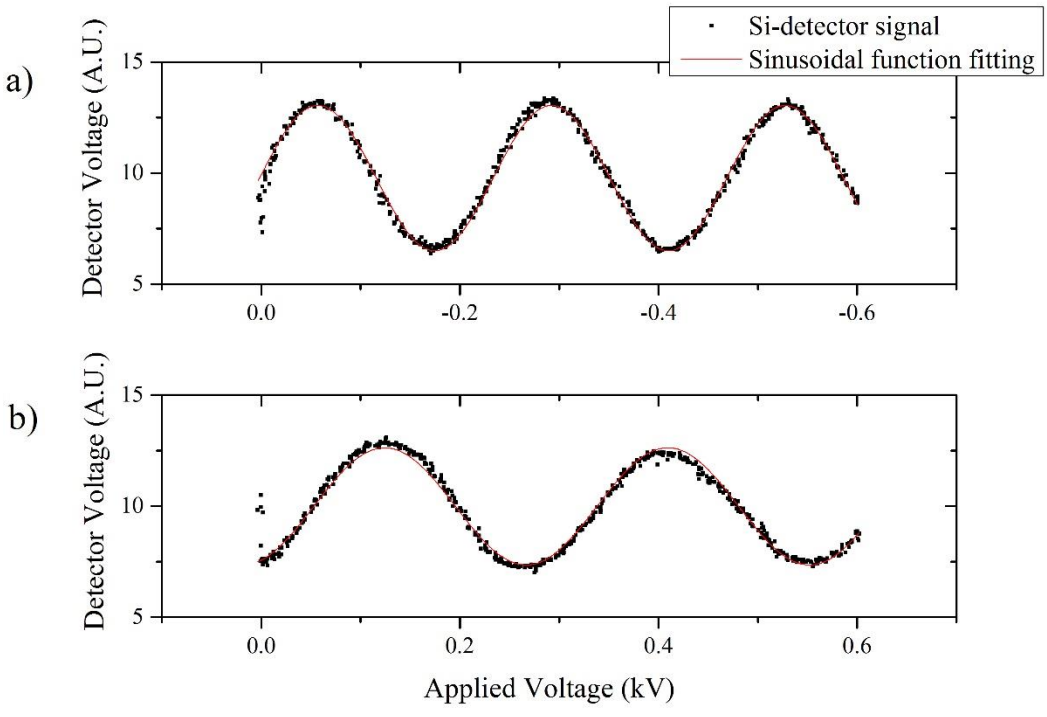

Figure 3.5 Variation of normalised detector output with the a) negative and b) positive applied voltage of a waveguide that overlaps with a PI domain, written under writing intensity of 0.18 MW/cm^2 and speed of 0.1 mm/sec.

In this figure, we can observe that there is a considerable difference between the phase shifts of the Mach-Zehnder transmittance for positive and negative applied voltages. In fact the positive voltage ramp (0 to +600 V) corresponds to a smaller phase change as compared to the negative ramp (0 to -600 V), which means that the negative voltage ramp produces a larger EO response. The corresponding values for the V_π and r_{33} for three individual measurements for each voltage direction of the same waveguide and their average value are shown in Table 3.1.

Applied Voltage	V_π	V_π error	r_{33}	Average r_{33}
0 → + 600V	0.14493	$2.68\times e^{-04}$	37.62456	37.05269
	0.14261	$2.45\times e^{-04}$	38.23665	
	0.14351	$2.62\times e^{-04}$	37.99685	
0 → - 600V	0.11764	$1.24\times e^{-04}$	46.35267	46.08834
	0.11859	$1.45\times e^{-04}$	45.98135	
	0.11872	$1.68\times e^{-04}$	45.931	

Table 3.1 Calculated values of the V_π, V_π error and r_{33} for six different measurements of a waveguide that overlaps with a PI domain, written under writing intensity of 0.18 MW/cm^2 and speed of 0.1 mm/sec. The obtained values are grouped depending on the direction of the applied voltage and the average r_{33} has been calculated for each case.

The above procedure was repeated for all the waveguides that were available for different writing intensities and their calculated average values of r_{33}, for negative and positive voltage ramps, are shown in the two graphs in Figure 3.6, a) and b) respectively. These graphs confirm the observation of Table 3.1, suggesting that the average value of r_{33} is higher for the negative voltage ramp than for the positive and it's valid for all measurements done. Furthermore in all waveguides tested in this sample, the value of r_{33} that was measured with a negative ramp is systematically higher than the value measured in a Ti-diffused reference channel waveguide, which was found to be 33.7 pm/V. The EO response for the positive direction of the voltage ramp is higher only for the waveguide written under the highest writing intensity. It is essential here to not that the average r_{33} measurement obtained on the Ti-diffused channel waveguide appeared to be consistent

regardless the direction of the applied voltage and it is in agreement with the literature values for unclamped crystal condition at wavelength of 633 nm [19].

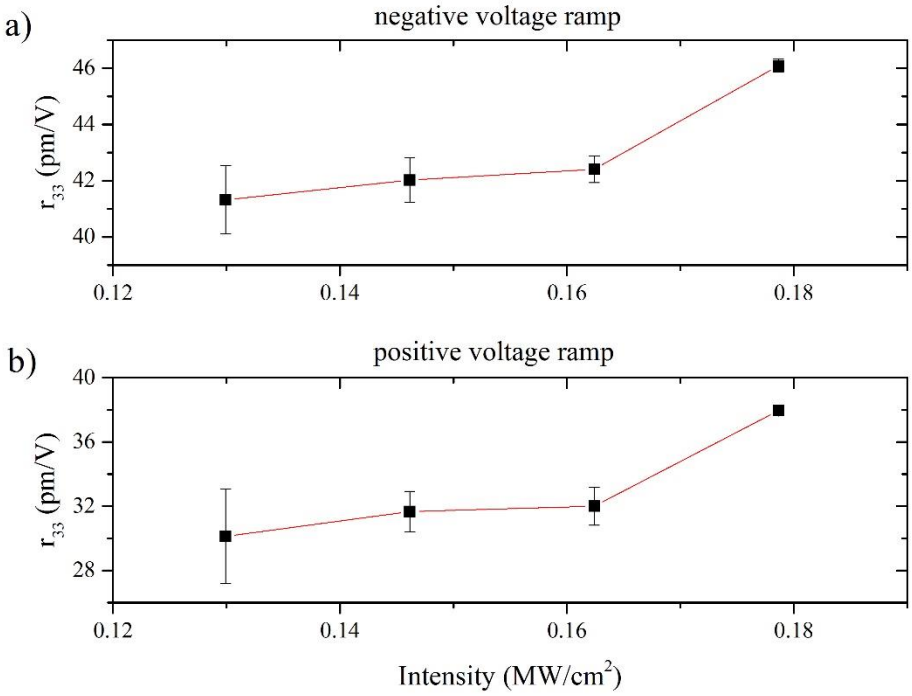

Figure 3.6 Intensity of the UV laser versus the measured r_{33} for: a) negative and b) positive voltage ramp. The red lines are guide to the eye.

The asymmetry in the EO response that has been observed in the measurements of the EO coefficient as a function of the voltage ramp direction provides a clue regarding the origin of the enhancement that was observed. In order to explain this asymmetry it's needed to be remembered that i) there is a domain structure that is superimposed to the channel waveguide and ii) the UV written waveguides are single mode at λ=633 nm and close to cut-off. Consequently, by applying a positive voltage ramp the dielectric contrast between the central domain and the surrounding crystal volume decreases because the refractive index of the PI domain decreases while the refractive index of the rest of the crystal increases thus resulting in worse confinement. The effect is further exaggerated by the fact that the UV written channel waveguides are weakly guiding, close to cut-off, structures which means that the mode size should change significantly by small changes in the refractive index distribution. This kind of asymmetric behaviour has been observed in previous work, where a spectral analysis of UV-written waveguides (without being superimposed with a PI domain) under applied voltages was performed [20]. It was found that the mode depth is expanding for positive applied electric field direction and shrinking for negative, causing a relative asymmetry on the measured maximum refractive index change. The different responses of the waveguides with applied voltage suggest a difference in the relative values of electro-optic coefficient (r_{33}) of the UV-written waveguides as compared to those for the bulk substrate. Changes in the mode size will of

course impact the overlap between the optical mode and the PI domain and ferroelectric structures of this type have been used as cut-off modulators [21].

In total three different samples (named Z5, Z6 and Z7) were fabricated in this experiment using the same writing conditions, containing PI channel waveguides, and the r_{33} was calculated following the experimental procedure as described before, this time only for negative directed voltages, based on the previous observations. The higher values of the effective electro-optic coefficient were observed in waveguides that were fabricated using higher laser intensities, which in principle corresponds to higher refractive index changes (tighter optical confinement) and deeper PI domains. In these waveguides the optical mode is restricted largely within the volume that corresponds to the PI domain that runs along the waveguide channel. Waveguides fabricated at lower UV-laser intensities exhibited lower enhancement of the electro-optic coefficient since it is expected that the overlap between the propagating mode and the PI domain is smaller because the peak refractive index change is smaller [4] and the corresponding PI domains are shallower consisting mostly of an arrangement of nano-domains [10]. The obtained r_{33} values for each sample and writing condition are shown in Table 3.2.

Intensity	**r_{33} (pm/V)**		
	Sample Z5	***Sample Z6***	***Sample Z7***
0.12	41.32521	--	--
0.14	42.02212	42.84724	--
0.16	42.4035	42.50444	43.81557
0.18	46.08834	--	42.0318

Table 3.2 Values of average r_{33} measurements of waveguides on different samples that overlaps with a PI domain, written under different writing intensities and speed of 0.1 mm/sec.

These observations, meaning the dependence of the effective electro-optic coefficient r_{33} with the writing intensity are illustrated in Figure 3.7. The mode depth of four single-mode waveguides, written under different writing intensities, was measured through near-field intensity profiles for TM polarisation at λ=633 nm, without any external application of a voltage. In the same graph, on Figure 3.7a), the depth of the PI domains written under the same conditions is shown in order to demonstrate that the overlap between the waveguide mode and the PI domains is increasing for higher intensities. In Figure 3.7b, the corresponding r_{33} for each waveguide is shown. The PI depth profiles

measurements were taken from previous works, using SEM images of a wedge-polished sample as described in Chapter 1 and Chapter 2.

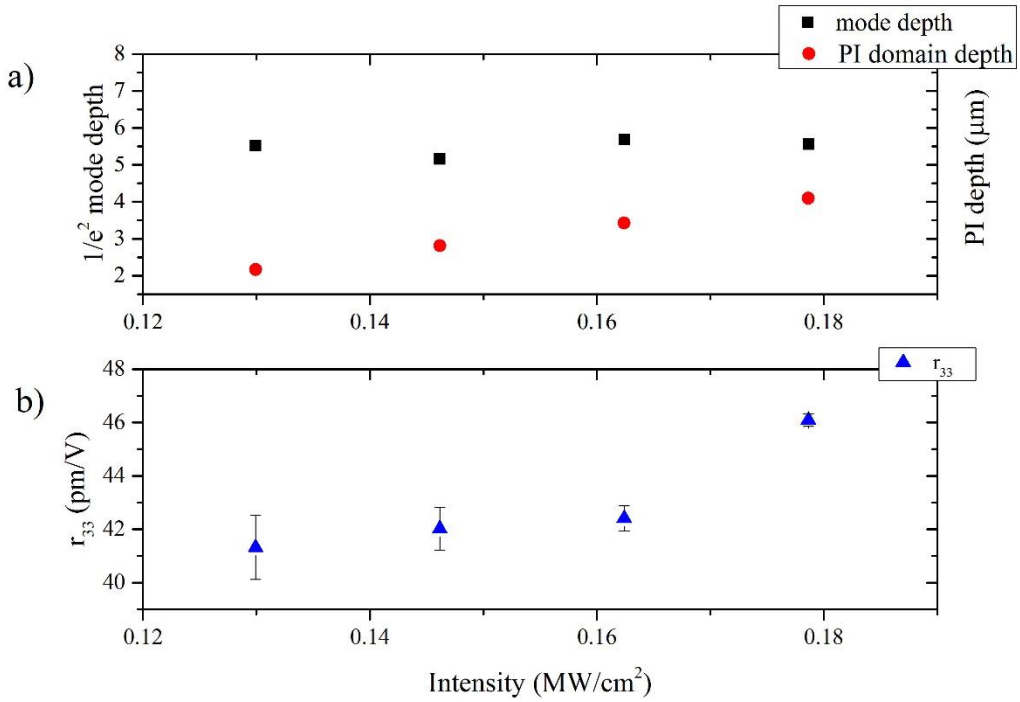

Figure 3.7 a) Comparison between $1/e^2$ measurements of mode depths (for λ=633nm and TM polarisation) and PI domain depth as measured in [22] versus the writing intensity and b) the r_{33} measured for each waveguide.

3.6 Proposed mechanism

According to the illustration of a PI domain formation mechanism that is presented in Figure 3.1 it is expected that the PI domain should overlap with the distribution of refractive index change that is produced by the lithium migration that occurred during the UV laser irradiation step. Consequently the propagating waveguide mode should overlap, to some extent, with the PI domain. The degree of overlap will depend upon the size of the waveguide mode, controlled by the range and magnitude of the refractive index change, and the dimensions and quality of the PI domain. These parameters are controlled by the UV-laser irradiation conditions [2], [22]. Furthermore, as the centre of the refractive index profile coincides with the laser irradiated track there will always be a portion of the propagation mode contained within the domain wall that surrounds the PI domain. In the previous section we have resented strong evidence that suggests that the enhancement of r_{33} is connected to the overlap between the waveguide mode and the PI domain.

Here we will argue that this enhancement is related to stress, which occurs at the boundary between opposite domains. As there is a PI domain that runs along the length of the UV waveguide

there will be a domain wall containing the optical mode. This wall is an up/down domain boundary either side of the channel and a tail-to-tail domain boundary below the channel (see Figure 3.1). Evidence of stress on the domain boundary and its impact on the photonic properties of the crystal can be found in several reports in the literature. One study in particular, ref. [12] shows numerical modelling of the refractive index reconstruction across a up/down ferroelectric domain boundary. These numerical results shows a sharp variation of the ordinary refractive index centred at the domain boundary.

Some of the data which are presented in [12] are reproduced here for clarity. The refractive index profile across the domain boundary was calculated from NSOM transmission data and the results are shown in Figure 3.8. From this measurement it occurs that there is a refractive index change that is associated with the newly poled area, which corresponds to the shaded area in the graph. This refractive index change is associated with the internal field in congruent crystals and reduces with time (or after thermal annealing) [23], [24]. In addition to this large-scale refractive index change a smaller range but large amplitude refractive index change is also shown in the plot. This short-range refractive index change profile has a width of ~2.5 μm and changes sign either side of the domain wall and is centred at the domain boundary, which is indicated by the arrow in the plot.

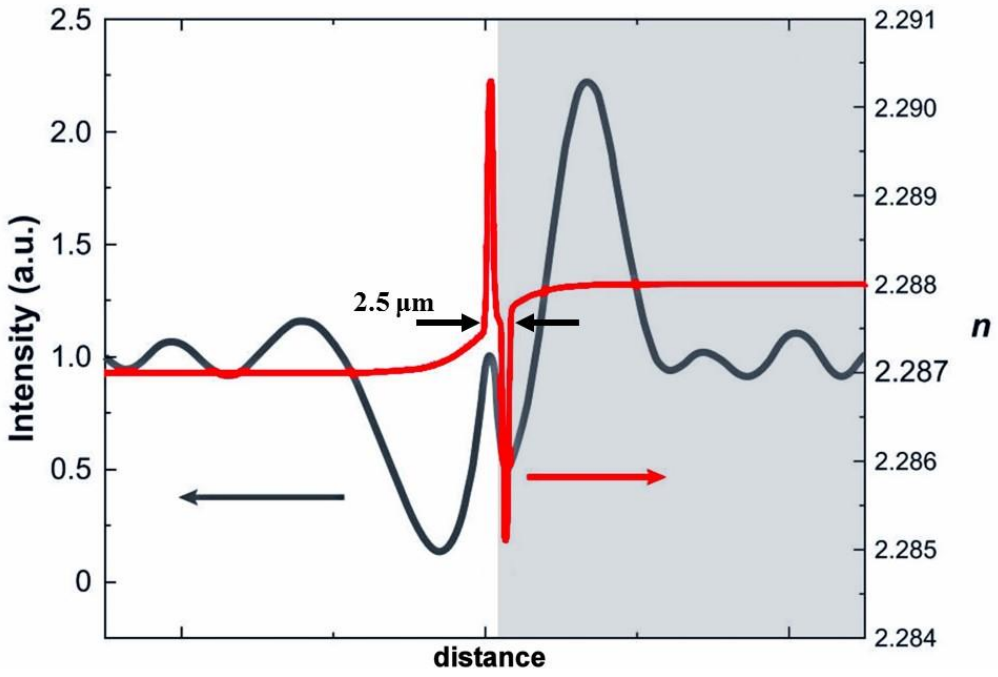

Figure 3.8 Refractive index profile (red line) and the intensity of light (grey line) emerging after propagation through a domain wall in a 500μm thick crystal. The shaded zone indicates the domain inverted region. The vertical arrow indicates the position of the domain boundary. Reprinted from Reference [12]

Ref [13] shows that a ×10 increase of the peak value of the ordinary refractive index is observed in UV written channel waveguides that are subjected to PI. This systematic increase in the peak refractive index is illustrated in Figure 3.3 for waveguides, which were written with different laser intensities. A similar refractive index discontinuity was observed in the domain boundaries that were used as TIR switches/deflectors [25] . Interestingly the refractive index discontinuity, which was reported in [25] persisted thermal annealing. There is sufficient evidence in the literature suggesting that the photonic response in the vicinity of a domain wall is different as compared to the bulk crystal, due to strain that is associated with the domain wall and the crystal non-stoichiometry. We suggest here that this strain that manifests itself through the changes in the refractive index and which extends to several microns away from the domain wall, is also responsible for the increase in the nonlinear/electro-optic response that we observed in our composite structure.

The effects that are described in refs [13], [25] must have the same origin and are related to stress on the domain boundary between the newly poled domain and the virgin crystal. By combining the reports in the literature it is possible to interpret the observation of reference [12] as the result of the fact that a PI domain is essentially an unpoled region, which is embedded in a domain inverted volume. According to the literature the refractive index will increase in the virgin (unpoled) volume within a range of ~2.5 μm from each domain wall while the domain inverted volume of the crystal close to the domain wall will have a lower refractive index. In other words the refractive index of the pre-existing waveguide core will increase while the refractive index of the cladding will decrease making the optical confinement stronger as has been observed in [12].

3.7 Conclusions

The electro-optic effect of UV-written waveguides that overlap with UV-induced poling inhibited domains has been investigated. The waveguide and the overlapping PI domain are both produced by a single UV irradiation process using 244 nm CW laser irradiation and are thus self-aligning. A 36.7 % enhancement of the inherent electro-optic coefficient has been observed. The effect is attributed to the stress field, which is associated with the presence of a domain wall that contains the channel waveguide. Evidence of stress in the vicinity of a domain wall can be found in the literature. Measurement of the EO coefficient enhancement as a function of the UV writing intensity confirms the hypothesis that the overlap between the optical waveguide mode and the PI domain is a crucial factor for the observed EO coefficient enhancement.

An asymmetry of the values of the electro-optic coefficient was also found depending on the direction of the applied voltage ramp (positive/negative). This was attributed to the push pull effect of the applied voltage on the core/cladding refractive index. For positive voltage ramps the dielectric contrast between core and cladding of the PI UV written waveguide reduces resulting in poor

confinement and hence poor overlap between optical mode and PI domain which leads to lower values of the EO coefficient.

These results have technological value as the observed enhancement of the EO coefficient can lead to the fabrication of a lower-voltage operation integrated optical modulators or to shorter devices.

3.8 References

[1] H. Lu, B. Sadani, N. Courjal, G. Ulliac, N. Smith, V. Stenger, M. Collet, F. I. Baida, and M.-P. Bernal, "Enhanced electro-optical lithium niobate photonic crystal wire waveguide on a smart-cut thin film.," *Opt. Express*, vol. 20, no. 3, pp. 2974–81, 2012.

[2] S. Mailis, C. Riziotis, I. T. Wellington, P. G. R. Smith, C. B. E. Gawith, and R. W. Eason, "Direct ultraviolet writing of channel waveguides in congruent lithium niobate single crystals.," *Opt. Lett.*, vol. 28, no. 16, pp. 1433–5, 2003.

[3] C. L. Sones, P. Ganguly, Y. J. Ying, F. Johann, E. Soergel, R. W. Eason, and S. Mailis, "Spectral and electro-optic response of UV-written waveguides in $LiNbO_3$ single crystals," *Opt. Express*, vol. 17, no. 26, pp. 23755–64, 2009.

[4] P. Ganguly, C. L. Sones, Y. Y. Ying, H. Steigerwald, K. Buse, E. Soergel, R. W. Eason, and S. Mailis, "Determination of refractive indices from the mode profiles of UV-written channel waveguides in $LiNbO_3$-crystals for optimization of writing conditions," *Light. Technol. J.*, vol. 27, no. 16, pp. 3490–3497, 2009.

[5] C. Sones, S. Mailis, V. Apostolopoulos, I. E. Barry, C. Gawith, P. G. R. Smith, and R. W. Eason, "Fabrication of piezoelectric micro-cantilevers in domain-engineered LiNbO 3 single crystals," *J. Micromechanics Microengineering*, vol. 12, no. 1, pp. 53–57, 2002.

[6] A. C. Muir, G. J. Daniell, C. P. Please, I. T. Wellington, S. Mailis, and R. W. Eason, "Modelling the formation of optical waveguides produced in $LiNbO_3$ by laser induced thermal diffusion of lithium ions," *Appl. Phys. A*, vol. 83, no. 3, pp. 389–396, 2006.

[7] U. Schlarb. and K. Betzler, "Refractive indices of lithium niobate as a function of temperature, wavelength, and composition: A generalized fit," *Physical Review B*, vol. 48, no. 21, 1993.

[8] F. Johann, Y. J. Ying, T. Jungk, A. Hoffmann, C. L. Sones, R. W. Eason, S. Mailis, and E. Soergel, "Depth resolution of piezoresponse force microscopy," *Appl. Phys. Lett.*, vol. 94, no. 17, p. 172904, 2009.

[9] C. L. Sones, a. C. Muir, Y. J. Ying, S. Mailis, R. W. Eason, T. Jungk, Á. Hoffmann, and E. Soergel, "Precision nanoscale domain engineering of lithium niobate via UV laser induced inhibition of poling," *Appl. Phys. Lett.*, vol. 92, no. 7, 2008.

[10] C. Y. J. Ying, G. J. Daniell, H. Steigerwald, E. Soergel, and S. Mailis, "Pyroelectric field assisted ion migration induced by ultraviolet laser irradiation and its impact on ferroelectric domain inversion in lithium niobate crystals," *J. Appl. Phys.*, vol. 114, no. 8, p. 083101, 2013.

[11] M. de Angelis, S. De Nicola, A. Finizio, G. Pierattini, P. Ferraro, S. Grilli, and M. Paturzo, "Evaluation of the internal field in lithium niobate ferroelectric domains by an interferometric method," *Appl. Phys. Lett.*, vol. 85, no. 14, p. 2785, 2004.

[12] V. Gopalan, V. Dierolf, and D. A. Scrymgeour, "Defect–domain wall interactions in trigonal ferroelectrics," *Annu. Rev. Mater. Res.*, vol. 37, no. 1, pp. 449–489, 2007.

[13] C. L. Sones, P. Ganguly, C. Y. J. Ying, E. Soergel, R. W. Eason, and S. Mailis, "Poling-inhibited ridge waveguides in lithium niobate crystals," *Appl. Phys. Lett.*, vol. 97, no. 15, p. 151112, 2010.

[14] H. Steigerwald, M. Lilienblum, F. von Cube, Y. J. Ying, R. W. Eason, S. Mailis, B. Sturman, E. Soergel, and K. Buse, "Origin of UV-induced poling inhibition in lithium niobate crystals," *Phys. Rev. B*, vol. 82, no. 21, p. 214105, 2010.

[15] R. J. Holmes, Y. S. Kim, C. D. Brandle, and D. M. Smyth, "Evaluation of crystals of $LiNbO_3$ doped with MgO or TiO_2 for electrooptic devices," *Ferroelectrics*, vol. 51, no. 1, pp. 41–45, 1983.

[16] A. Méndez, G. De la Paliza, A. García-Cabañes, and J. M. Cabrera, "Comparison of the electro-optic coefficient r_{33} in well-defined phases of proton exchanged $LiNbO_3$ waveguides," *Appl. Phys. B*, vol. 73, no. 5, pp. 485–488, 2001.

[17] S. Ducharme, J. Feinberg, and R. Neurgaonkar, "Electro-optic and piezo-electric measurements in photo-refractive barium titanate and strontium barium niobate," *IEEE J. Quantum Electron.*, vol. 23, no. 12, pp. 2116–2121, 1987.

[18] E. L. Wooten and W. S. C. Chang, "Test structures for characterization of electrooptic waveguide modulators in lithium niobate," *IEEE J. Quantum Electron.*, vol. 29, no. 1, pp. 161–170, 1993.

[19] K. K. Wong, "Electro-Optic Coefficients of $LiNbO_3$," in Properties of Lithium Niobate, *Institution of Engineering and Technology*, 2002.

[20] C. L. Sones, P. Ganguly, Y. J. Ying, F. Johann, E. Soergel, R. W. Eason, and S. Mailis, "Spectral and electro-optic response of UV-written waveguides in $LiNbO_3$ single crystals", *Opt. Express*, vol. 17, no. 26, pp. 23755–64, 2009.

[21] D. Tulli, D. Janner, M. Garcia-Granda, R. Ricken, and V. Pruneri, "Electrode-free optical sensor for high voltage using a domain-inverted $LiNbO_3$ waveguide near cut-off," *Appl. Phys. B Lasers Opt.*, vol. 103, no. 2, pp. 399–403, 2011.

[22] C. Y. J. Ying, A. C. Muir, C. E. Valdivia, H. Steigerwald, C. L. Sones, R. W. Eason, E. Soergel, and S. Mailis, "Light-mediated ferroelectric domain engineering and micro-structuring of lithium niobate crystals," *Laser Photon. Rev.*, vol. 6, no. 4, pp. 526–548, 2012.

[23] V. Gopalan and M. Gupta, "Observation of internal field in $LiTaO_3$ single crystals: Its origin and time-temperature dependence," *Appl. Phys. Lett.*, vol. 68, February, pp. 1995–1997, 1996.

[24] C. Battle, S. Kim, and V. Gopalan, "Ferroelectric domain reversal in congruent $LiTaO_3$ crystals at elevated temperatures," *Appl. Phys. …*, vol. 76, no. 17, pp. 2436–2438, 2000.

[25] R. Eason, A. Boyland, S. Mailis, and P. Smith, "Electro-optically controlled beam deflection for grazing incidence geometry on a domain-engineered interface in $LiNbO_3$," *Opt. Commun.*, vol. 197, pp. 201–207, 2001.

Chapter 4: UV laser-induced poling inhibition in proton exchanged LN crystals

4.1 Introduction

Ferroelectric domain engineering [1] in congruent lithium niobate is used for a variety of applications such as wavelength conversion by quasi-phase-matching [2], acousto-optic devices [3] and surface/bulk micro-structuring [4]. It can be achieved by the process of EFP, where an external electric field, exceeding the crystal's coercive field E_c, is applied along the polar direction [5]. However, the large aspect ratio, which is required for fine domain period periodically poled LN (PPLN), leads to spreading of the newly formed domain out from the electrodes, which are used for the spatially selective domain switching, making fabrication of fine domains (≤ 2 μm) challenging.

PI induced by UV laser irradiation [6]·[7] in congruent and Mg-doped CLN can overcame EFP's limitations by reducing the aspect ratio of the inverted domains allowing for the fabrication of finer domain structures. This method is capable of producing domains with a moderate that can be controlled, to some extent, by the UV laser exposure conditions [8]. In this method UV laser irradiation of the +z polar surface of the crystal result in a local increase of the coercive field [7] by causing migration of lithium ions due to i) diffusion in the temperature gradients [9] and ii) drift in the pyro-electric field [10]. Consequently a uniform electric field applied along the z direction poles the crystal uniformly apart from the volume, which is affected by the UV laser irradiation, which remains *poling inhibited*. The limited depth of the PI domains suggests that such structures will find applications in optical waveguide systems therefore it is important to establish whether poling inhibition is applicable with established waveguide fabrication methods.

A combination of the UV-induced PI method with the traditional waveguide fabrication technology of proton-exchange could result in a new way for production of nonlinear, electro-optic and acousto-optic devices in lithium niobate. The feasibility of producing PI domains in PE waveguides will therefore be the subject of this chapter. Firstly, an introduction to the proton exchange waveguide formation will be given, followed by a summary of the recent studies on domain engineering in PE/CLN substrates. Afterwards, the experimental procedures and results will be presented.

4.2 Proton Exchange waveguide fabrication

Proton exchange technique is a common method for used for the fabrication of low-loss optical waveguides in LN crystals [11]. It is a simple and effective method for the fabrication of waveguides with a much higher photorefractive damage threshold [12] and much lower process temperatures with respect to the Ti in-diffusion method. However, this method induces changes only on the extraordinary refractive index therefore the waveguides that are produced with this method only guide light that is polarised along the z-axis of the crystal. The process consists the substitution of Li^+ ions with H^+ protons at the surface of the crystal when it is exposed to an acid bath at elevated temperatures. The PE process yields different crystallographic phases of $H_xLi_{1-x}NbO_3$, depending on the value of x. In total there are seven different single crystal phases [13]: α, κ1, κ2, β1, β2, β3, and β4 (in the order of proton concentration increase in the phase). Structure and phase composition of the PE waveguides has a significant influence on their optical characteristics. The implementation of protons causes a change of the lattice parameters of the CLN unit cell relative to the concentration of protons and has as consequence the increase of the refractive index of the crystal [14]-[15]. However, PE waveguides were found to have reduced electro-optic coefficients after formation of the waveguide because of the violent nature of the chemical process that takes place [12], [16], [17]. The reduction of the optical nonlinearity and of the spontaneous polarisation can be restored by subsequently annealing, forming a final graded-index APE waveguide (APE=Annealed Proton-Exchange) [18] for surface waveguides suitable for photonic applications, and APE followed by a reverse proton exchange [19], for buried waveguides. However, even after annealing some residual damage remains in a submicron surface layer.

4.3 Domain engineering in PE:CLN waveguides

Ferroelectric domain engineering in proton exchange waveguides on CLN is an essential method in order to adjust its optical properties, for example to achieve (QPM) [20]. Periodic poling has been successfully obtained in such substrates by performing the poling step before the waveguide fabrication [21], [22]. However this technique requires a suitable, softer, proton-exchange recipe, in order to avoid the detriment of the PPLN structure when modifying the refractive-index profile [23], [24]. Another difficulty is raised by the fact that in certain kinds of proton exchange processes used to create waveguides, the nonlinearity of the crystal is reduced or even eliminated [25].

Another approach for domain engineering in PE:CLN is to perform the poling process after the waveguide formation. It has been reported that the PE layer can actually inhibit the poling on CLN under specific conditions, making possible a PE pattering for PPLN formation without poling current control [17], [26]. Inhibition of poling occurs in PE waveguides that have been fabricated

without the annealing step afterwards, due to the smaller conductivity of the PE layer in contrast with the virgin crystal and hence it's acting as an isolating film in the surface layer when EFP is performed. The phase of the PE waveguide that has been attributed to this effect is the one with the highest Li^+–H^+ substitution ratio (x~70%, β –phase), and is characterized by vanishing nonlinear and electro-optic coefficients [27]. Nevertheless, poling of PE waveguides in CLN have been successfully achieved when using APE waveguides, with slight adjustments (compared to standard CLN) of the electric poling conditions. [28]–[31].

Domain engineering in proton exchange waveguides in CLN has been found to be challenging. The results depend on the chosen fabrication sequence (poling and PE waveguide formation), the selection of the characteristics of the proton-exchange waveguide (α or β phase, PE or APE) and the poling current control (slow or fast). This work aims to investigate whether the process of UV laser-induced poling inhibition can be applied successfully is PE lithium niobate in the same way as it has been applied to CLN and Mg-doped CLN crystals. More specifically the PI process will be applied to APE planar waveguide substrates on CLN and Mg-doped samples. The impact of PI process on the PE itself will also be investigated especially since the UV irradiation step influences the lithium ions concentration in the crystal layer where PE occurs. SEM and PFM measurements are used for the characterisation of the PI domain formation in PE waveguides. The influence of the UV irradiation on the PE waveguide formation is also of interest and will be part of the investigation. Finally, the result of PE process on substrates that have undergone PI domain treatment prior to PE will be presented.

4.4 Investigation of UV-induced poling inhibition in congruent and Mg-doped PE:CLN waveguides

4.4.1 Experimental Procedures

The crystals investigated were 0.5 mm thick, z-cut, optical-grade, undoped CLN (Crystal Technology, Inc., US) and 5 mol% Mg-doped CLN (Yamaju ceramics). A set of proton-exchanged waveguides was prepared on these substrates at the Royal Institute of Technology of Stockholm, Sweden using the APE technique. More specifically, the APE planar waveguides were produced on the ± z faces of the samples by immersing CLN substrates in pure benzoic acid at 158 °C for 15 hours resulting in the replacement of lithium ions by protons from the molten benzoic acid (β-phase $H_xLi_{1-x}NbO_3$) up to a depth of ~ 1 μm or less, increasing the refractive index. The thermal annealing was performed in air temperature of 325 °C for 26 hours, forming a final graded-index APE waveguide with estimated depth of ~1.7μm [32], suitable for photonic applications. However, even after annealing some residual damage remains in a submicron surface layer.

Afterwards, the specimens were exposed to UV laser radiation by scanning the samples in front of the focussed laser beam producing linear irradiated tracks. A c.w. UV laser beam from a frequency doubled argon ion laser (244 nm) was used in these experiments, focused down to a spot size of ~2.5 μm on the +z face of the crystal. The linear tracks were aligned along the crystallographic y-direction using a set of computer controlled two axes translation stage (Aerotech ABL1500), which allows nm resolution. The scanning speed was kept constant at the value of 0.1 mm/sec. The laser powers, which were used in our experiments, were within the range of 15-37 mW which correspond to values of intensities of 0.13-0.36 MW/cm^2.

Following UV laser irradiation the crystal is subjected to domain inversion by the application of a uniform electric field along the z direction. Past experience suggests that good quality, continuous PI domains in CLN can be obtained by maintaining a slow domain wall velocity during the EFP step. The domain wall velocity can be controlled by the amplitude of the applied voltage [33]. In our experiments the amplitude of the applied voltage was ramped up slowly (5 Volts/sec) up to a value around of ~19.5 kV ± 100V/mm on the PE:CLN samples and about ~ 4kV/mm ± 100V/mm on PE Mg-doped CLN, where domain nucleation started to occur. The transparent holder which is used in our poling apparatus enables the real time monitoring of nucleation events and domain wall movements by taking advantage of the stress induced birefringence that occurs at the domain wall. The values of the applied voltage used for the PI process in our PE samples were similar to the ones used for PI in CLN crystals without a PE layer for both congruent LN [6] and Mg-doped LN crystals, where EFP is known to be slower [34], [35], and the poling process performed without any complications.

The depth profile of any PI domain that were formed during the process has been investigated in detail using scanning electron microscopy of the HF etched y-face cross section of the crystal which is perpendicular to the direction of the laser irradiated tracks. However, in order to maximize the resolution of the relatively shallow domain structures the PI sample was wedge-polished at an angle of ~5° with respect to the surface as described in previous chapters. The polished wedge has a substantial z-face component, which provides very high contrast due to significant differential etching as compared to y-face etching [36]. Finally, the large surface area, which corresponds to the wedge, and the absence of a sharp surface discontinuity, is suitable for investigation with piezoresponse force microscopy [37].

Identical samples to the ones used for the depth profiles, used for optical waveguide characterization. Therefore, they were edge-polished until no defects were visible under inspection with an optical microscope reassuring good end-face quality that is required for efficient coupling to the optical waveguides.

4.4.2 PI in PE:CLN waveguides

Depth profiles: Etching with HF acid produces normally a visible contrast between areas with different polarity due to differential etching between opposite z-faces is affected by the acid. By investigating the surface topography along the wedge polished plane, which corresponds largely to a z-face, we expect that any height difference is associated to inhibited domain structures. The surface topography of a UV-exposed and etched wedge polished PE sample is shown in the SEM images of Figure 4.1. Images a, b, c, and d correspond to UV laser tracks irradiated with intensities of 0.13 MW/cm^2, 0.15 MW/cm^2, 0.17 MW/cm^2, 0.19 MW/cm^2 respectively at a laser spot size of ~ 2.5 μm. The wedge polished surface lies on the left of each image as indicated by the arrow while the vertical dash line indicates the change of slope.

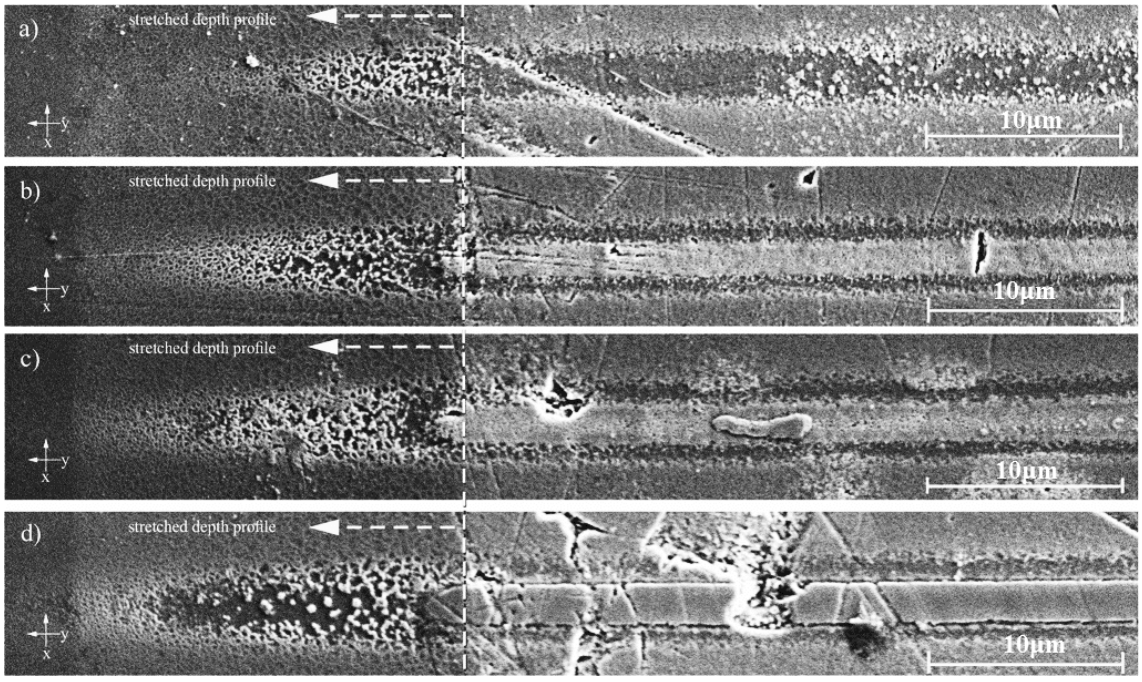

Figure 4.1 SEM images of wedge-polished and HF etched tracks fabricated by UV-laser irradiation followed by EFP. The laser intensities used are: (a) 0.13 MW/cm^2, b) 0.15 MW/cm^2, c) 0.17 MW/cm^2 and d) 0.19 MW/cm^2. The dashed lines indicate the boundary where the slope changes due to wedge polishing.

Before going into the details of the impact of the PI process it is necessary to discuss the differences in the etching quality between the PE waveguide surface and the virgin crystal. Normally, the etching of the virgin crystal is relatively smooth (at least for a few minutes etching). Careful observation of the SEM images of Figure 4.1 reveals that there is a clearly defined zone of increased surface roughness that extends from the point of the sample where the slope changes, due to wedge polishing, to a length of 19.4 μm that corresponds to a depth of ~1.7 μm where it stops abruptly. Interestingly, the area that exhibits a roughness that occur as a result of HF etching correspond to a

depth that is well within the proton rich volume of the crystal which is close to the surface. According to the fabrication conditions of this particular sample the 1/e depth distribution of protons is expected to be around 3 μm. So it is reasonable to conclude that this roughness is associated with high concentration of protons.

Assuming that the observed roughness is associated with the proton concentration we can conclude that an obvious impact of the laser irradiation is the modification of the proton concentration. This conclusion comes from the observation that the etch roughness is reduced immediately below the UV irradiated tracks as it can be seen in Figure 4.1. This effect is becoming more obvious as the laser intensities increasing, from Figure 4.1a to Figure 4.1d. As the intensity becomes higher the effect becomes very pronounced, as seen in Figure 4.2. Images a, b, c, and d correspond to UV laser tracks irradiated with at intensities of 0.25 MW/cm^2, 0.27 MW/cm^2, 0.30 MW/cm^2, 0.31 MW/cm^2 respectively.

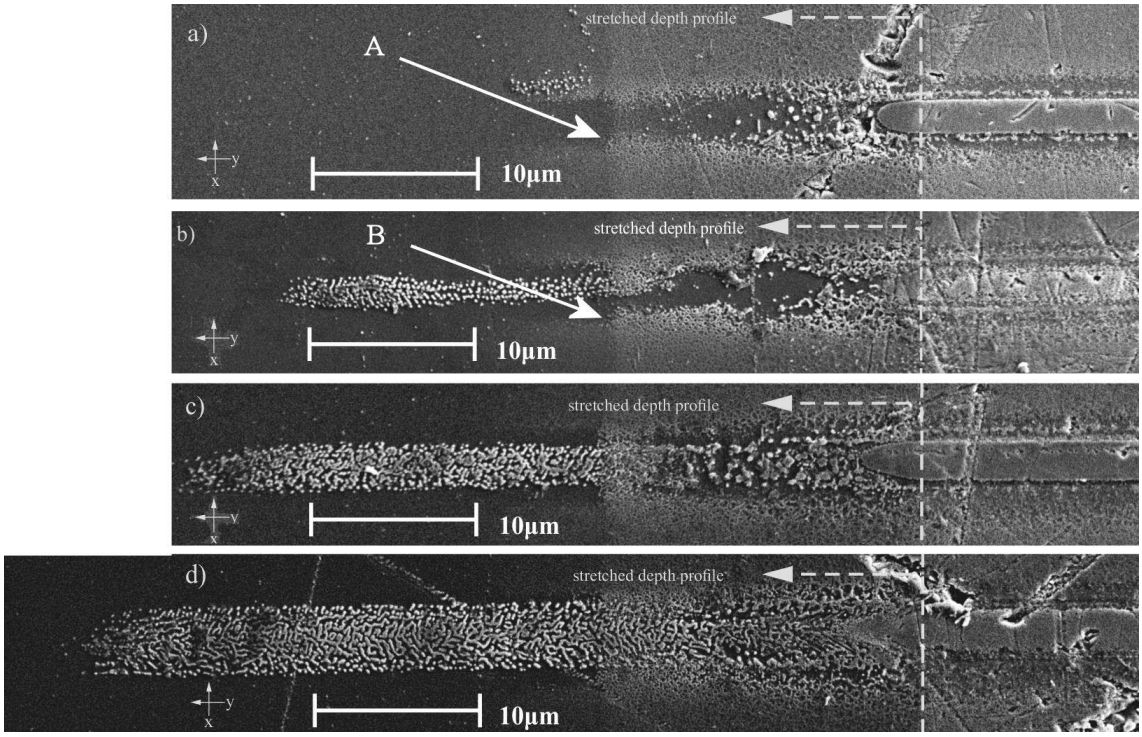

Figure 4.2 SEM images of wedge-polished and HF etched tracks fabricated UV-laser irradiation followed by EFP. The laser intensities used are: (a) 0.25 MW/cm^2, b) 0.27 MW/cm^2, c) 0.30 MW/cm^2 and d) 0.31 MW/cm^2. The dashed lines indicate the boundary where the slope changes due to wedge polishing

The SEM images presented in Figure 4.2 show some laser-induced surface damage, which can be seen along the laser irradiated tracks on the original z-surface which is to the right of the vertical dash line. The depth profile of the volume that is immediately below the UV laser irradiated tracks consists of grainy etch resistant features, which is a characteristic of isolated nano-domains, which

have formed within the heat affected zone [10] that extends deeper into the crystal with increasing irradiating laser intensity. These features are characteristic of PI domain formation, however, at these irradiation conditions these domains as not solid as in the case of CLN crystals. Furthermore, from these images, we can also conclude that the concentration of protons immediately bellow the laser tracks has been reduced. Also, the proton distribution has changed around the deeper end of the proton rich zone and around the edges of the laser track. More specifically it seems that proton concentration have increased deeper into the crystal i.e. at positions A and B. It seems therefore that the temperature distribution, which is the result of UV laser irradiation, has pushed protons away outside that heated volume to the side and deeper into the crystal. Furthermore, in the lower intensity range (Figure 4.2b), the etch resistant PI feature appear below the 1.7 μm deep, proton rich zone. This trend is also observed at higher intensities (Figure 4.2c,d), however within this range of laser intensities some PI features appear closer to the surface. The conclusions that can be drawn from these observations are; a) UV laser irradiation affects the proton concentration hence interferes with the integrity of the PE waveguide and b) poling inhibition is discouraged in the proton rich layer.

Evidently, the UV laser irradiation conditions, which were used successfully for the production of PI domains with congruent crystals while minimizing the surface damage caused by the UV laser beam have proven largely ineffective in the case of PE crystals. By further increasing the irradiating laser intensity to 0.36 MW/cm^2 the etch profile of the wedge polished section changes dramatically. In this high intensity irradiation case a solid etch resistant feature has formed, shown in the SEM image, which is presented in Figure 4.3a, that is reminiscent of PI domains observed in CLN crystals. The ferroelectric identity of the revealed etch-resistant feature was interrogated using piezoresponse force microscopy (PFM). The result of the PFM scan is shown in Figure 4.3b, which reveals that the piezoresponse contrast of the etch resistant feature is characteristic of a ferroelectric domain with opposite polarity with respect to the background crystal. Further examination of the PFM and SEM images indicate that at this intensity level there is significant surface damage and the formation of a possibly non-ferroelectric zone that corresponds to peak of the temperature distribution, which is established by the absorbed UV laser radiation.

The formation of PI domains in congruent crystals has been attributed to the redistribution of lithium ions under the influence of the UV laser induced temperature gradients [6]·[7]·[10]. In the case of the PE crystal a similar mechanism is considered, which however relies in the redistribution of protons as well as lithium ions under the same driving force of temperature-gradient driven diffusion.

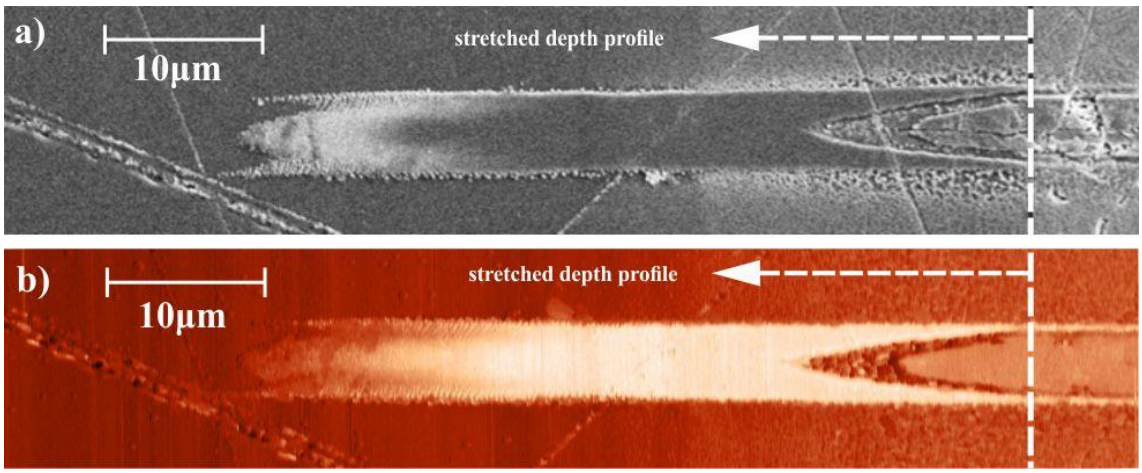

Figure 4.3 SEM image (a) and PFM scan (b) of the depth profile of an UV-induced PI domain in PE sample. The UV-laser intensity used was 0.36 MW/cm^2. The dashed lines indicate the boundary where the slope changes due to wedge polishing

Measurements of the PI domain profile as revealed by wedge polishing yielded a plot of the depth and width of the domains as a function of the laser intensity, as shown in Figure 4.4. From the SEM images the UV irradiated tracks can be grouped into 3 different types as a function of their surface and depth quality as shown in Figure 4.1, Figure 4.2 and Figure 4.3: (Figure 4.1a-d and Figure 4.2a) − PE modification, (Figure 4.2b-d) − scattered nano-domains, and (Figure 4.3a) − solid domains with a laser-damaged surface.

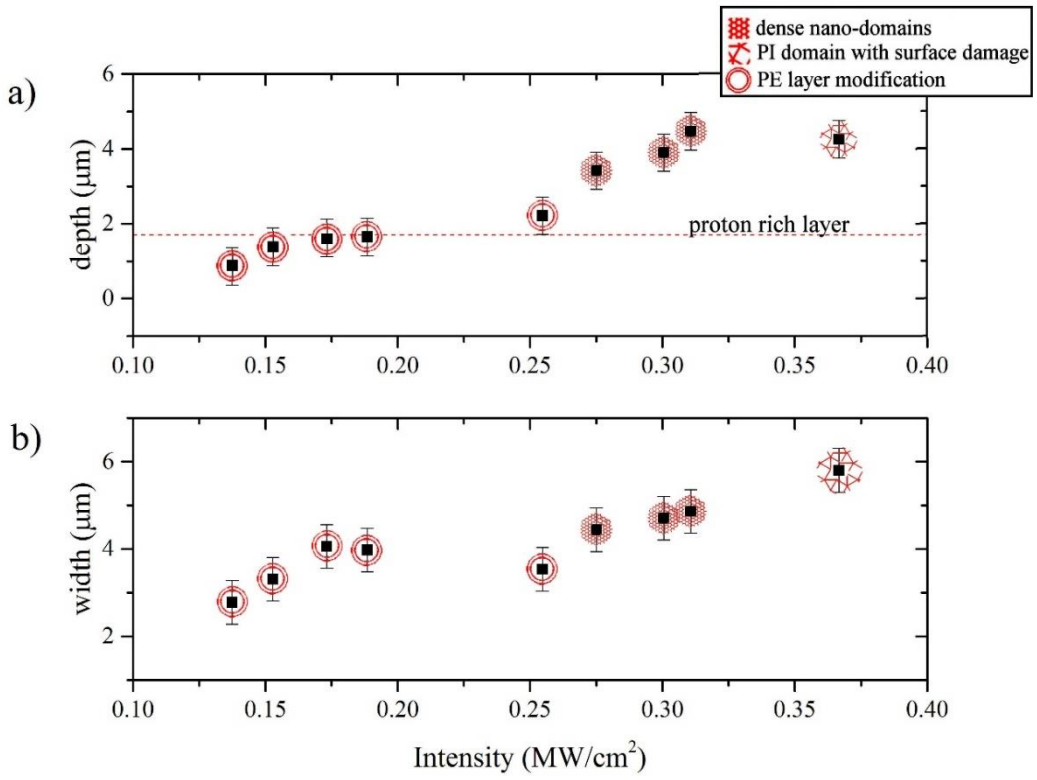

Figure 4.4 The depth (a) and width (b) of UV-laser tracks in a PE undoped CLN (as measured from the SEM images of wedge polished samples) plotted as a function of

the laser intensity. The red symbols correspond to various surface and depth qualities and the red dashed line corresponds to the depth of the high proton exchange layer.

In general, it seems that there is not a window of exposure conditions that can provide solid domains with no surface damage in our samples while at the lower limit of laser intensity there in no observation of PI domain formation. However, our results suggest that that the formation of the PI solid domains is dependant of the PE waveguide characteristics. Samples with thinner PE layer or weak PE could possibly require reduced laser intensities in order to achieve the redistribution of protons and therefore no surface damage.

Evidence of proton concentration changes due to UV-laser irradiation has been provided by the etched depth profiles of the UV-laser irradiated PE crystals. Moreover, redistribution of protons implies a variation of the PE waveguide profile. Waveguide transmission experiments were therefore conducted to verify this hypothesis. A CLN sample was uniformly proton exchanged on its +z face to form a planar waveguide supporting TM modes [14],[38]. The UV laser tracks were exposed on the +z-face and along the y-direction to reproduce the conditions that were used for the PI experiments. Finally, both y-faces of the crystal sample were edge polished in order to couple light into the PE optical waveguide. A He-Ne beam, with the appropriate polarization to excite TM modes, was focussed by a microscope objective onto the polished edge of the PE waveguide. The near field intensity profile of the propagating mode was imaged on a CCD camera by a second microscope objective. The schematic, which is shown in Figure 4.5 illustrates the experimental arrangement that was used for the waveguide propagation experiment. By translating the sample it was possible to investigate any changes on the propagating planar waveguide mode that were caused by the PI process in the vicinity of the UV irradiated tracks.

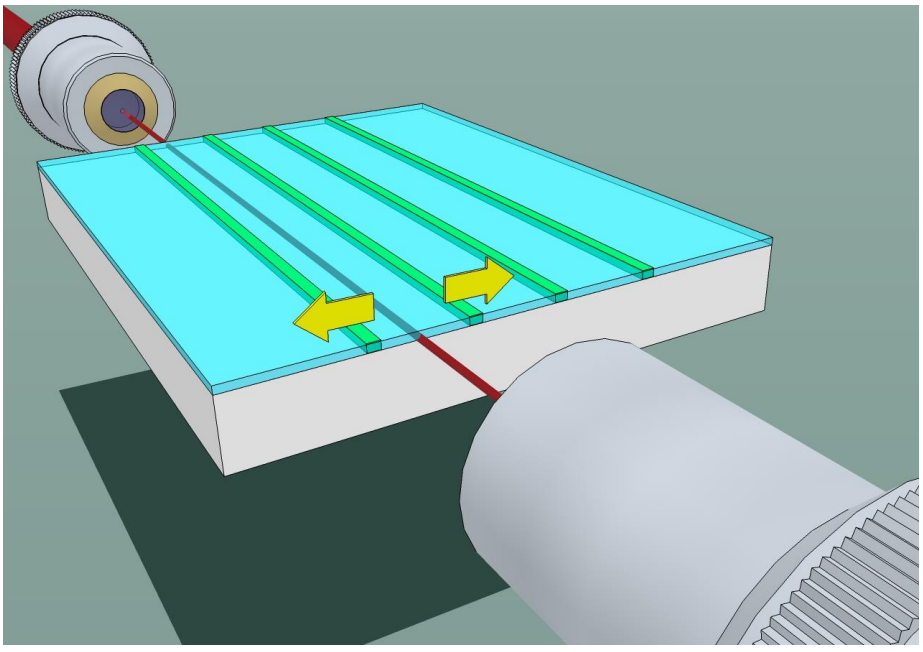

Figure 4.5 Schematic of the waveguide coupling experiment. A 633nm He-Ne laser beam is coupled into the PE waveguide and coupled out through two objectives. The

waveguide coupling point is able to move anywhere between the UV-laser irradiated tracks.

Using this experimental arrangement the following observations were made depending on the light coupling position; when the coupling point to the sample (waveguide) lies anywhere between two adjacent laser tracks, which are separated by ~100 μm, a planar waveguide mode profile is observed at the output facet. The near field intensity pattern of the waveguide mode in this case is shown in Figure 4.6a where it can be also observed that the mode exhibits some structure of the lateral intensity profile, which is evidence of lateral confinement.

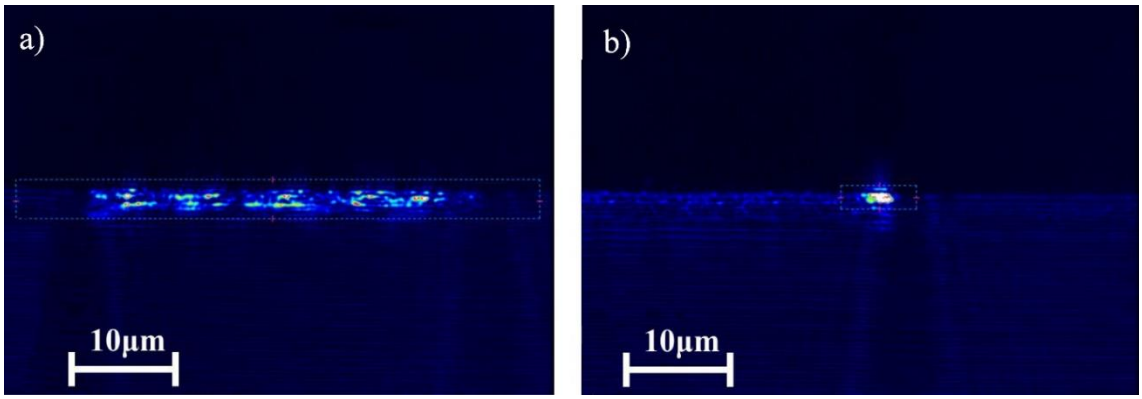

Figure 4.6 Near-field intensity profiles of two UV-induced PI domains on the PE:CLN surface planar waveguide, fabricated by a UV-laser beam focused to a spot size of ~ 2.5μm at intensity of 0.36 MW/cm^2 Incident coupling point of the He-Ne beam is located a) between the two adjacent irradiated tracks and b) right of the centre of the track.

When the coupling point is located right at the edge of the laser track the output appears to be that of a single mode *channel waveguide* (Figure 4.6b) while no waveguide propagation was observed when the coupling point is aligned with the laser track.

These waveguide propagation results suggest that the original planar waveguide has been modified by the laser-irradiation. The absence of propagation when the coupling point overlaps with the end of the laser track can be justified by a local reduction of the refractive index due to the displacement of protons combined with an increase of scattering loss due to laser-induced surface damage. The protons that were displaced due to diffusion caused by the temperature gradients, which are formed due to the strong laser absorption, will produce a proton rich channel adjacent to the track hence producing a linear section with increased refractive index right next to the laser track which justifies the channel waveguide formation that was observed. Finally, light that propagates in the 100 μm wide section of the original planar waveguide which lies between two tracks will experience

lateral confinement due to the refractive index modulation that is associated with the redistribution of protons. This lateral confinement justifies the lateral mode structure that was observed in our experiments.

Investigation on the near-field intensity profiles of the rest UV-induced PI domains on the PE:CLN planar waveguide, which were written under lower intensities and shown no formation of a solid PI domain was performed as well. The results obtained are similar as for the highest laser intensity used and discussed earlier. For instance, in Figure 4.7 a channel which was written under the lowest intensity used of 0.13 MW/cm^2 is shown for incident coupling point of the He-Ne beam located a) as close as possible to the surface and b) deeper in the crystal. This track corresponds to the SEM image of Figure 4.1a. For reminder purposes, these irradiated conditions caused modification on the proton concentration, mainly on the surface (~ 1-2 μm), with no hint of the PI effect.

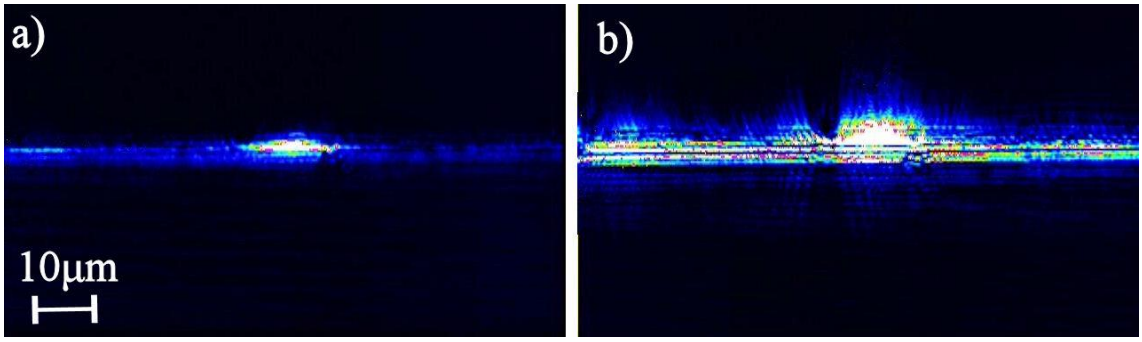

Figure 4.7 Near-field intensity profiles of a UV- irradiated track on the PE:CLN surface planar waveguide. The UV laser intensity used was 0.13 MW/cm^2. The coupling point of the He-Ne beam is located: a) as close as possible to the surface and b) deeper in the crystal.

At Figure 4.7a, where the incident beam is positioned at the surface of the sample, a single-mode channel waveguide appears, while a Figure 4.7b where the incident beam is deeper, the PE planar waveguide can be seen. From Figure 4.7b, the position of the track is well defined through the diffracted pattern and it's clearly right next of the increased refractive index enhanced intensity profile, hence observing the same effect for both lateral and vertical scopes under different writing conditions.

4.4.3 Mg-doped PE:CLN waveguides

PI domain formation was successfully achieved in Mg-doped PE:CLN waveguides as can be seen in Figure 4.8. Similar to the PI domain fabrication in the undoped crystal, the best conditions found to be the ones with the highest laser intensity (0.36 MW/cm^2). Analogous etch roughness up to a depth of ~1.9 μm.

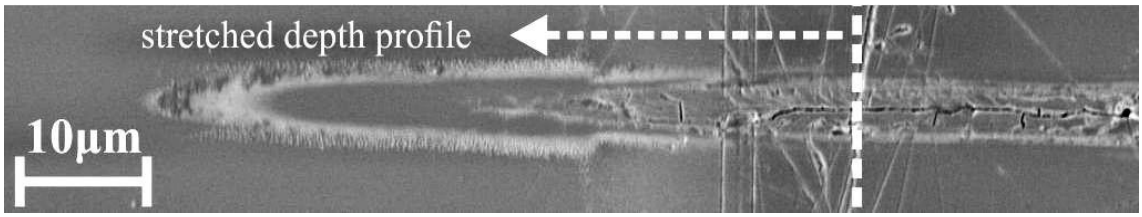

Figure 4.8 SEM image of the depth profile of a UV-induced PI domain in Mg-doped PE. The UV-laser intensity used was 0.36 MW/cm^2. The dashed lines indicate the boundary where the slope changes due to wedge polishing.

In further comparison with the PI domain in undoped PE:CLN samples of Figure 4.4a, the scattered nano-domains appeared to be more dense in Mg-doped case, and surrounding the solid PI domain. Another interesting observation is that the PI domain becomes wider below the rich proton layer (~1.4µm), meaning that the electrostatic barrier which is formed as a result of laser irradiation is stronger in the low proton concentration. This effect have not been observed in PI domains formed in undoped PE:CLN waveguides, where the PI width found to be well confined along the depth of the sample. Nevertheless, the measured overall depth of the PI domains on the Mg-doped PE:CLN found to be similar with the PI depth measured in undoped PE:CLN, which is ~ 4.5µm. This is an encouraging result as previous work on non PE samples shown that Mg-doped CLN crystals produced shallower domains than in CLN for the same UV laser irradiation conditions [10].

Inspection of the effect while using lower laser intensities in the Mg-doped PE:CLN samples was also performed, showing no formation of a solid PI domain, but instead of scattered nano-domains as shown in Figure 4.9, where the track corresponds for laser intensity of 0.25 MW/cm^2. Again, these results are in agreement with the undoped samples.

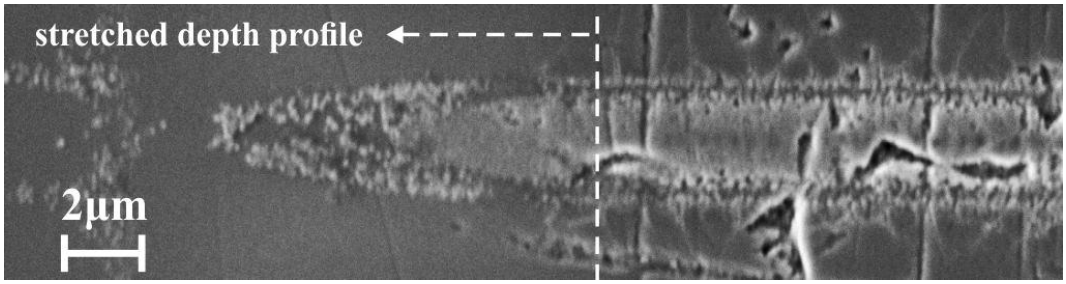

Figure 4.9 SEM image of the depth profile of scattered nano-domains of an UV laser track in Mg-doped PE sample followed by EFP. The laser intensity used was 0.25 MW/cm^2. The dashed lines indicate the boundary where the slope changes due to wedge polishing.

4.5 Investigation of PE after UV-induced PI domains in CLN

This second approach included the formation of the PI domains before the waveguide fabrication. The objective of this work was to investigate whether the development of the PE waveguide is being affected by the pre-irradiation of the sample and the presence of the PI domains and also if the PE process affects the integrity PI domains. The PE waveguide was designed to be near the cut-off (at 633 nm). In this way slight variations of the proton concentration would have a significant impact on the propagating mode.

4.5.1 Experimental Procedures

The crystals investigated were 0.5 mm thick, z-cut, undoped CLN (Crystal Technology, Inc., US). UV irradiation was performed on the +z face of the crystals, along the crystallographic y-direction with a spot size of ~2.5 μm. The writing speed was kept constant at 0.1 mm/sec and the laser intensity was within the range of 0.13- 0.36 MW/cm^2.After the UV illumination step, the crystals were uniformly poled by EFP with the applied voltage ramped at a rate of 5 Volts/sec to a value of ~19.5 kV. Slow domain wall speed during the EFP step was ensured. The last processing step was the PE waveguide formation.

PE was performed afterwards on all samples in benzoic acid to obtain a PE layer of thickness ~300nm and then they were annealed at 330^{o}C. The final planar APE effective refractive index at 633nm found to be n_{eff}=2.2313.

One of the processed samples was wedge-polished at an angle of ~5° with respect to the surface and was briefly etched in HF acid to reveal a magnified view of the domain depth profile in order to check the quality of the PI domains after the PE waveguide formation. The rest of the samples were edge-polished for waveguide transmission experiments.

4.5.2 Results and discussion

The UV-induced PI domains after the PE process can be seen in the SEM images of Figure 4.10. These images show the wedge polished and briefly etched (1 min) areas of the substrate that corresponds to the UV exposed tracks. The vertical dashed line indicates the point where the slope changes and the arrow indicated the direction of the depth profile section. These four figures illustrate the results, which correspond to UV-laser irradiation conditions of writing speed of 0.1mm/sec and laser intensity of a) 0.13 MW/cm^2, b) 0.15 MW/cm^2, c) 0.17 MW/cm^2, d) 0.19 MW/cm^2 and e) 0.36 MW/cm^2. Difference in the etching quality between the PE waveguide region and the virgin non PE crystal was observed as in Section 4.4.2, but mostly on the surface of the crystal since the PE waveguide was very shallow. Therefore, the PE process doesn't appear to have an impact on the PI domain, persisting their initial characteristics.

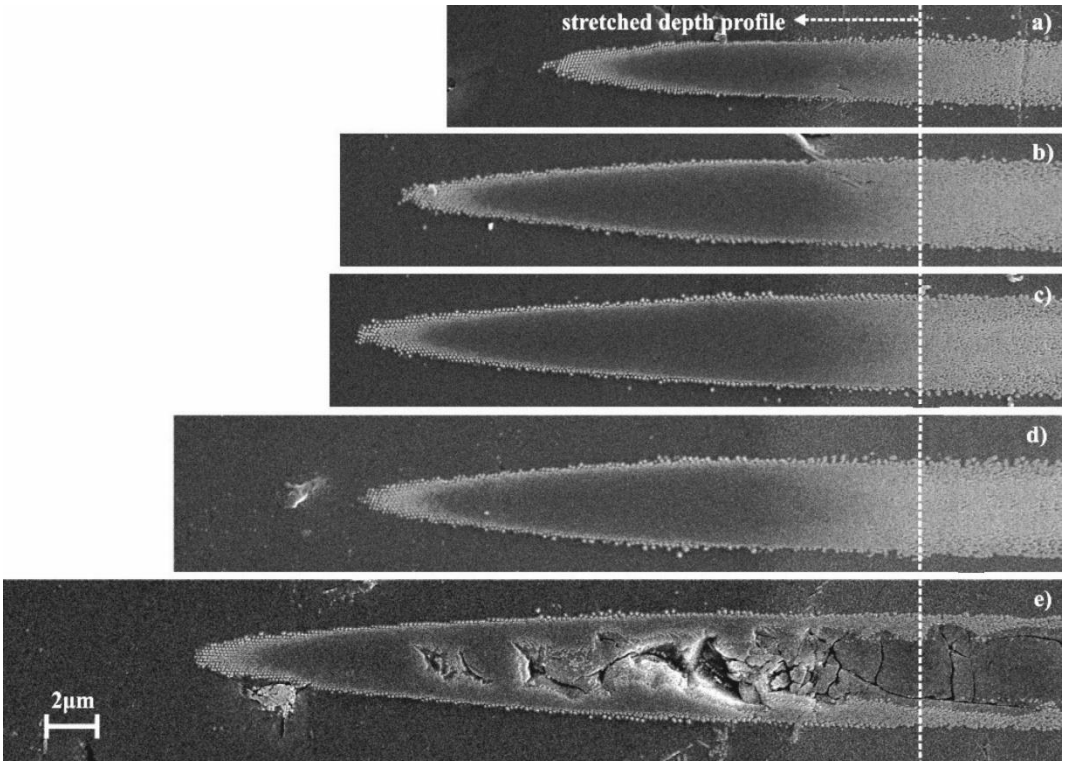

Figure 4.10 SEM images of the depth profile of UV-induced PI domain in a CLN sample were PE waveguide formation was performed afterwards. The UV-laser intensity was: a) 0.13 MW/cm^2, b) 0.15 MW/cm^2, c) 0.17 MW/cm^2, d) 0.19 MW/cm^2 and e) 0.36 MW/cm^2. The dashed lines indicate the boundary where the slope changes due to wedge polishing

Using the optical setup, which was described in n previous sections, near-field intensity profiles of the APE:$LiNbO_3$ surface planar waveguide were taken. The waveguide transmission was influenced by the distance between the coupling position and the location of a UV-laser irradiated track in this case as well. When the coupling position lies anywhere between two adjacent laser tracks, which are separated by 100 µm, the lateral profile shows a multimode behaviour as shown in Figure 4.10.

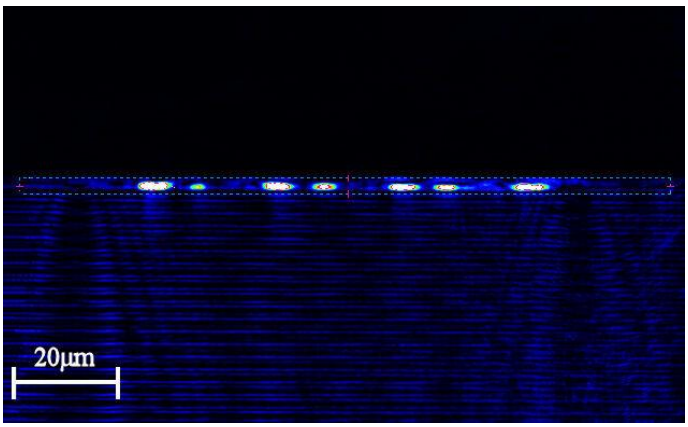

Figure 4.11Near-field intensity profile of an APE:CLN surface planar waveguide between two adjacent UV-induced PI domains.

No propagation was observed when the coupling point is located on the laser track indicating that the UV-laser irradiation cause a local decrease of the refractive index in the PE layer. Bearing in mind that the planar waveguide was designed to be right at the cut-off point for propagation at λ=633 nm the effect can be attributed to lower concentration of protons in the UV irradiated areas.

4.6 Conclusions

In summary, a study of ferroelectric domain inversion in proton exchanged congruent and Mg-doped lithium niobate crystals using irradiation of a continuous wave UV-laser (λ=244 nm) was presented. Two different approaches were investigated depending on the sequence of the fabrication steps. The first one implies firstly the PE waveguide formation and subsequently the UV irradiation and the poling step. It was found that UV-irradiation under specific conditions of post proton exchanged crystals modifies the proton concentration and consequently the associated waveguide. The results were confirmed using differential etching in HF acid and PFM. More specifically, the experiments indicate that PI does not occur in the proton rich layer of the waveguide for low laser intensities, however using high UV-laser intensities the local proton concentration reduces sufficiently to allow for the formation of PI domains. The UV laser induced redistribution of protons consequently modifies the refractive index profile of the original waveguide providing lateral confinement for the propagating light.

The second investigated approach consists the fabrication of UV-induced poling inhibited domains firstly, and the PE waveguide process step afterwards. The results revealed that the PE waveguide formation is altered in the PI regions which causes transformation in its refractive index profile. Nevertheless, the PE process doesn’t have an impact on the PI domains.

4.7 References

[1] V. Y. Shur, "Domain engineering in Lithium Niobate and Lithium Tantalate: Domain wall motion," *Ferroelectrics*, vol. 340, no. 1, pp. 3–16, 2006.

[2] G. D. Miller, R. G. Batchko, W. M. Tulloch, D. R. Weise, M. M. Fejer, and R. L. Byer, "42%-efficient single-pass c.w. second-harmonic generation in periodically poled lithium niobate," *Opt. Lett.*, vol. 22, no. 24, pp. 1834–1836, 1997.

[3] R. V. Schmidt and I. P. Kaminow, "Acousto-optic Bragg deflection in $LiNbO_3$ Ti-diffused waveguides," *Quantum Electron. IEEE J.*, vol. 11, no. 1, pp. 57–59, 1975.

[4] C. Sones, S. Mailis, V. Apostolopoulos, I. E. Barry, C. Gawith, P. G. R. Smith, and R. W. Eason, "Fabrication of piezoelectric micro-cantilevers in domain-engineered $LiNbO_3$ single crystals," *J. Micromechanics Microengineering*, vol. 12, no. 1, pp. 53–57, 2002.

[5] M. Yamada, N. Nada, M. Saitoh, and K. Watanabe, "First-order quasi-phase matched $LiNbO_3$ waveguide periodically poled by applying an external field for efficient blue second-harmonic generation," *Appl. Phys. Lett.*, vol. 62, no. 5, p. 435, 1993.

[6] S. Mailis, A. C. Muir, Y. J. Ying, C. L. Sones, R. W. Eason, T. Jungk, Á. Hoffmann, and E. Soergel, "UV laser radiation inhibits domain inversion in lithium niobate," *Conf. Lasers Electro-Optics*, vol. 92, no. 7, pp. 1–2, May 2008.

[7] H. Steigerwald, M. Lilienblum, F. von Cube, Y. J. Ying, R. W. Eason, S. Mailis, B. Sturman, E. Soergel, and K. Buse, "Origin of UV-induced poling inhibition in lithium niobate crystals," *Phys. Rev. B*, vol. 82, no. 21, p. 214105, 2010.

[8] G. Zisis, C. Y. J. Ying, E. Soergel, and S. Mailis, "Ferroelectric domain building blocks for photonic and nonlinear optical microstructures in $LiNbO_3$," *J. Appl. Phys.*, vol. 115, no. 12, p. 124102, Mar. 2014.

[9] A. C. Muir, G. J. Daniell, C. P. Please, I. T. Wellington, S. Mailis, and R. W. Eason, "Modelling the formation of optical waveguides produced in $LiNbO_3$ by laser induced thermal diffusion of lithium ions," *Appl. Phys. A*, vol. 83, no. 3, pp. 389–396, 2006.

[10] C. Y. J. Ying, G. J. Daniell, H. Steigerwald, E. Soergel, and S. Mailis, "Pyroelectric field assisted ion migration induced by ultraviolet laser irradiation and its impact on ferroelectric domain inversion in lithium niobate crystals," *J. Appl. Phys.*, vol. 114, no. 8, p. 083101, 2013.

[11] C. E. Rice and J. L. Jackel, "$HNbO_3$ and $HTaO_3$: New cubic perovskites prepared from $LiNbO_3$ and $LiTaO_3$ via ion exchange," *J. Solid State Chem.*, vol. 41, no. 3, pp. 308–314, 1982.

[12] T. Fujiwara, R. Srivastava, X. Cao, and R. V Ramaswamy, “Comparison of photorefractive index change in proton-exchanged and Ti-diffused $LiNbO_3$ waveguides”, *Optics Letters*, vol. 18, no. 5, pp. 633–635, 1993.

[13] Y. N. Korkishko and V. A. Fedorov, “Structural phase diagram of proton-exchanged waveguides in $LiNbO_3$,” in: Properties of Lithium Niobate, *Ed. INSPEC*, IEE, London, UK, pp. 43–49, 1999.

[14] J. L. Jackel, “Proton exchange for high-index waveguides in $LiNbO_3$,” *Appl. Phys. Lett.*, vol. 41, no. 7, p. 607, 1982.

[15] Y. N. Korkishko and V. A. Fedorov, "Ion Exchange in Single Crystals for Integrated Optics and Optoelectronics", *Cambridge Int Science* Publishing, 1999.

[16] F. Riehle, "Frequency Standards: Basics and Applications", *Weinheim, FRG: Wiley-VCH Verlag GmbH & Co*, 2003.

[17] S. Grilli, C. Canalias, F. Laurell, P. Ferraro, and P. De Natale, “Control of lateral domain spreading in congruent lithium niobate by selective proton exchange,” *Appl. Phys. Lett.*, vol. 89, no. 3, p. 032902, 2006.

[18] P. G. Suchoski, T. K. Findakly, and F. J. Leonberger, “Stable low-loss proton-exchanged $LiNbO_3$ waveguide devices with no electro-optic degradation.,” *Opt. Lett.*, vol. 13, no. 11, pp. 1050–2, 1988.

[19] J. L. Jackel and J. J. Johnson, “Reverse exchange method for burying proton exchanged waveguides,” *Electronics Letters*, vol. 27, no. 15. pp. 1360–1361, 1991.

[20] L. E. Myers, R. C. Eckardt, M. M. Fejer, R. L. Byer, W. R. Bosenberg, and J. W. Pierce, “Quasi-phase-matched optical parametric oscillators in bulk periodically poled $LiNbO_3$,” *J. Opt. Soc. Am. B*, vol. 12, no. 11, pp. 2102–2116, 1995.

[21] K. R. Parameswaran, R. K. Route, J. R. Kurz, R. V Roussev, M. M. Fejer, and M. Fujimura, “Highly efficient second-harmonic generation in buried waveguides formed by annealed and reverse proton exchange in periodically poled lithium niobate.,” *Opt. Lett.*, vol. 27, no. 3, pp. 179–81, 2002.

[22] L. Chanvillard, P. Aschiéri, P. Baldi, D. B. Ostrowsky, M. de Micheli, L. Huang, and D. J. Bamford, “Soft proton exchange on periodically poled $LiNbO_3$: A simple waveguide fabrication process for highly efficient nonlinear interactions,” *Appl. Phys. Lett.*, vol. 76, no. 9, p. 1089, 2000.

[23] M. L. Bortz, M. a Arbore, and M. M. Fejer, “Quasi-phase-matched optical parametric amplification and oscillation in periodically poled $LiNbO_3$ waveguides.,” *Opt. Lett.*, vol. 20, no. 1, pp. 49–51, 1995.

[24] K. El Hadi, M. Sundheimer, P. Aschieri, P. Baldi, M. P. De Micheli, D. B. Ostrowsky, and F. Laurell, “Quasi-phase-matched parametric interactions in proton-exchanged lithium niobate waveguides,” *J. Opt. Soc. Am. B*, vol. 14, no. 11, p. 3197, 1997.

[25] M. P. De Micheli, “Fabrication and Characterization of Proton Exchanged Waveguides in Periodically Poled Congruent Lithium Niobate,” *Ferroelectrics*, vol. 340, no. 1, pp. 49–62, Sep. 2006.

[26] M. Manzo, F. Laurell, V. Pasiskevicius, and K. Gallo, “Electrostatic control of the domain switching dynamics in congruent $LiNbO_3$ via periodic proton-exchange,” *Appl. Phys. Lett.*, vol. 98, no. 12, p. 122910, 2011.

[27] Y. N. Korkishko, V. a. Fedorov, and F. Laurell, “SHG-response of different phases in proton exchanged lithium niobate waveguides,” *IEEE J. Sel. Top. Quantum Electron.*, vol. 6, no. 1, pp. 132–142, 2000.

[28] A. N. Smirnova, S. S. Mushinskiy, I. S. Baturin, I. S. Azanova, D. I. Shevtsov, A. R. Akhmatkhanov, A. V. Ievlev, and V. Y. Shur, “Electric field poling of Lithium Niobate crystals after proton-exchanged channel waveguide fabrication,” *Ferroelectrics*, vol. 441, no. 1, pp. 9–16, 2012.

[29] O. Caballero-Calero, M. Kösters, T. Woike, K. Buse, A. García-cabañes, and M. Carrascosa, “Electric field periodical poling of lithium niobate crystals after soft-proton-exchanged waveguide fabrication,” *Appl. Phys. B*, vol. 88, no. 1, pp. 75–78, 2007.

[30] K. Gallo, M. De Micheli, and P. Baldi, “Parametric fluorescence in periodically poled $LiNbO_3$ buried waveguides,” *Appl. Phys. Lett.*, vol. 80, no. 24, p. 4492, 2002.

[31] M. a. Dolbilov, V. Y. Shur, E. I. Shishkin, M. F. Sarmanova, E. V. Nikolaeva, S. Tascu, P. Baldi, and M. P. de Micheli, “Influence of surface layers modified by proton exchange on domain kinetics of Lithium Niobate,” *Ferroelectrics*, vol. 374, no. 1, pp. 14–19, 2008.

[32] K. Gallo, C. B. E. Gawith, I. T. Wellington, S. Mailis, R. W. Eason, P. G. R. Smith, D. J. Richardson, and S. M. Kostritskii, “Ultraviolet writing of channel waveguides in proton-exchanged $LiNbO_3$,” *J. Appl. Phys.*, vol. 101, no. 1, p. 014110, 2007.

[33] V. Gopalan, T. E. Mitchell, and K. E. K. Sicakfus, “Switching kinetics of 180° domains in congruent $LiNbO_3$ and $LiTaO_3$ crystals,” *Solid State Commun.*, vol. 109, no. 2, pp. 111–117, 1998.

[34] A. Kuroda, S. Kurimura, and Y. Uesu, “Domain inversion in ferroelectric MgO: $LiNbO_3$ by applying electric fields,” *Appl. Phys. Lett.*, vol. 69, no. 11, p. 1565, 1996.

[35] K. Nakamura, J. Kurz, K. Parameswaran, and M. M. Fejer, “Periodic poling of magnesium-oxide-doped lithium niobate,” *J. Appl. Phys.*, vol. 91, no. 7, p. 4528, 2002.

[36] C. L. Sones, S. Mailis, W. S. Brocklesby, R. W. Eason, and J. R. Owen, “Differential etch rates in z-cut $LiNbO_3$ for variable HF/HNO_3 concentrations,” *J. Mater. Chem.*, vol. 12, no. 2, pp. 295–298, 2002.

[37] F. Johann, Y. J. Ying, T. Jungk, A. Hoffmann, C. L. Sones, R. W. Eason, S. Mailis, and E. Soergel, “Depth resolution of piezoresponse force microscopy,” *Appl. Phys. Lett.*, vol. 94, no. 17, p. 172904, 2009.

[38] P. Nekvindová, J. Špirková, J. Červená, M. Budnar, A. Razpet, B. Zorko, and P. Pelicon, “Annealed proton exchanged optical waveguides in lithium niobate: differences between the X- and Z-cuts,” *Opt. Mater. (Amst).*, vol. 19, no. 2, pp. 245–253, 2002.

[39] C. Y. Ying and Y. J. Ying, “Light-assisted Domain Engineering, Waveguide Fabrication, and Microstructuring of Lithium Niobate,” PhD thesis, Optoelectronics Research Centre, University of Southampton, 2011.

[40] S. Mailis, C. Riziotis, I. T. Wellington, P. G. R. Smith, C. B. E. Gawith, and R. W. Eason, “Direct ultraviolet writing of channel waveguides in congruent lithium niobate single crystals.,” *Opt. Lett.*, vol. 28, no. 16, pp. 1433–5, 2003.

[41] A. Smirnova and I. Azanova, “Effect of proton exchange waveguide on domain kinetics of lithium niobate,” *XIV International conference on micro/nanotechnologies and electronic devices (EDM)* pp. 234–236, 2013.

[42] M. C. Wengler, B. Fassbender, E. Soergel, and K. Buse, “Impact of ultraviolet light on coercive field, poling dynamics and poling quality of various lithium niobate crystals from different sources,” *J. Appl. Phys.*, vol. 96, no. 2004, pp. 2816–2820, 2004.

Chapter 5: Direct writing of channel waveguides and PI domains in LN using an amorphous silicon absorption layer.

5.1 Introduction

Waveguide fabrication [1], domain engineering [2] and micro-structuring [3], [4] on CLN crystal using the UV direct-writing technique has been proved to be simple, inexpensive and flexible to implement method as shown in the previous chapters of this work. In this part of the thesis, an alternative way to obtain similar outcomes was performed, with the aim of relaxing the requirement for the use of UV lasers. This can be achieved by the use of an over-layer that will serve as an absorber for the laser radiation. The heat that is generated in the absorber can then be coupled to the crystal underneath to create the temperature gradients that are required for all the above-mentioned processes.

The use of a Cr absorbing layer have been reported in [5], [6] to produce directly poled domains using UV and visible lasers. Although the domain inversion was successful it was found there that under laser irradiation and subsequent heating the Cr layer reduced the underlying crystal, which rendered the crystal useless for photonic applications. It was found however, that the Cr layer protected the crystal from laser damage allowing the formation of uniform solid domains.

Here we will investigate the use of amorphous Si (a-Si) as an absorbing layer. We will show that the use of a-Si enables the formation of optical waveguides and ferroelectric domain structures without changing significantly the oxygen content of the underlying crystal volume, which is advantageous for photonic applications. The expectation is that the absorption of the laser light by the a-Si film will cause it to heat up subsequently transferring the heat to the substrate. Due to the poor heat conductivity of CLN steep temperature gradients will form as in the case of direct UV light absorption by the crystal. The temperature gradients is the key ingredient that leads to lithium diffusion and to the modification of the coercive field and refractive index that has been reported before [7], [8].

Interestingly laser irradiation can also induce the crystallization of the original a-Si layer. This laser method has been applied to a-Si filled silica capillaries and was shown to produce record large crystallites and extreme modifications to the band structure of Si [9]. By applying this method to the planar geometry we expect that it will be possible to replicate the results obtained in the capillaries and thus create a hybrid platform for photonics consisting of two very important technological

materials, Si [10] and CLN [11]. However, this work mainly focuses on the thermal effects produced in CLN by the laser absorption from the a-Si layer. The crystallization of Si is beyond the scope of this research.

This chapter is divided in two parts. In the first one, a full investigation of the fabricated waveguides on CLN substrate is described. Waveguides were fabricated using a variety of exposure conditions and were subsequently characterised via propagation loss and mode sizes. In the second part, the results on domain engineering in CLN substrate through this technique are presented. The effect of inhibition of domain inversion is being shown first and the spontaneous domain inversion effect is following.

5.2 Sample preparation and direct laser writing

The crystals substrates used in these experiments were z-cut, undoped CLN (Crystal Technology, Inc., US) with a thickness of 500 μm and the final composite samples (a-Si/CLN) were produced by deposition of a-Si using plasma enhanced chemical vapour deposition (PE-CVD) [12] onto the polar z-faces of the substrates. The thickness of the deposited a-Si film was of order 200-250 nm and was uniform across the surface of the sample.

Direct laser writing on the a-Si coated CLN was realized using a Coherent Innova Sabre 25/7 argon ion laser that delivered continuous wave (CW) output at 488 nm wavelength. The laser beam was focused onto the crystal surface to a spot size of ~3.5 μm using a 36 × microscope objective lens (NA=0.52). Linear laser tracks were written on both z-faces of the crystal (different samples used for each z-face) by scanning the sample via a computer-controlled 2D translation stage, along the crystallographic y-axis in front of the focussed static laser beam. The laser intensities used in these experiments were in the range of 0.2-1.6 MW/cm^2 and the writing speeds used were between 0.01-1mm/sec. A polymer pellicle beam splitter (BS) was used to divert a portion of the back-reflected light towards a CCD camera that enabled imaging of the sample surface prior to laser writing. .

5.3 Optical channel waveguide formation

After laser irradiation the samples were edge polished, following the procedure that was described in previous chapters, in order to investigate the possible formation of waveguide channels below the laser irradiated tracks. It was found that optical channel waveguides were successfully produced on both +z and –z faces of the crystal the characteristics of which will be presented in the following sections. Interestingly, waveguide propagation in both TM and TE modes was observed.

This result is different from the case of UV laser exposure, indicating that the effect is more complex in nature than anticipated. After the initial assessment of the waveguide channels the over-layer was removed using potassium hydroxide (KOH) and the investigation was repeated for comparison.

5.4 Mode profile measurements

The mode profile of the waveguides was measured using a standard free space near-field measurement setup shown in Figure 5.1. Two He-Ne lasers operating at 632.8nm and 1.52μm wavelengths respectively, were used to couple light into the polished end-face of the channel waveguide-carrying sample by means of a microscope objective. The choice of microscope objectives (to maximize the coupling efficiency) depended upon the NA of the waveguides under investigation but the most common were 6.3× (NA=0.20) and 10× (NA=0.25). The laser wavelength could be chosen using a flipping mirror mount as indicated in the schematic. The sample was mounted on a precision 4-axis translation stage in order to achieve the best possible coupling conditions. As both He-Ne lasers were linearly polarized a half wave plate was used to selectively excite TM and TE modes in the waveguides. The light transmitted through the waveguides was collected from the opposite end-face by a second microscope objective lens (40×, NA=0.65) that imaged the output face onto a CCD camera thus providing an image of the near field intensity profile of the mode propagating in the waveguide under investigation.

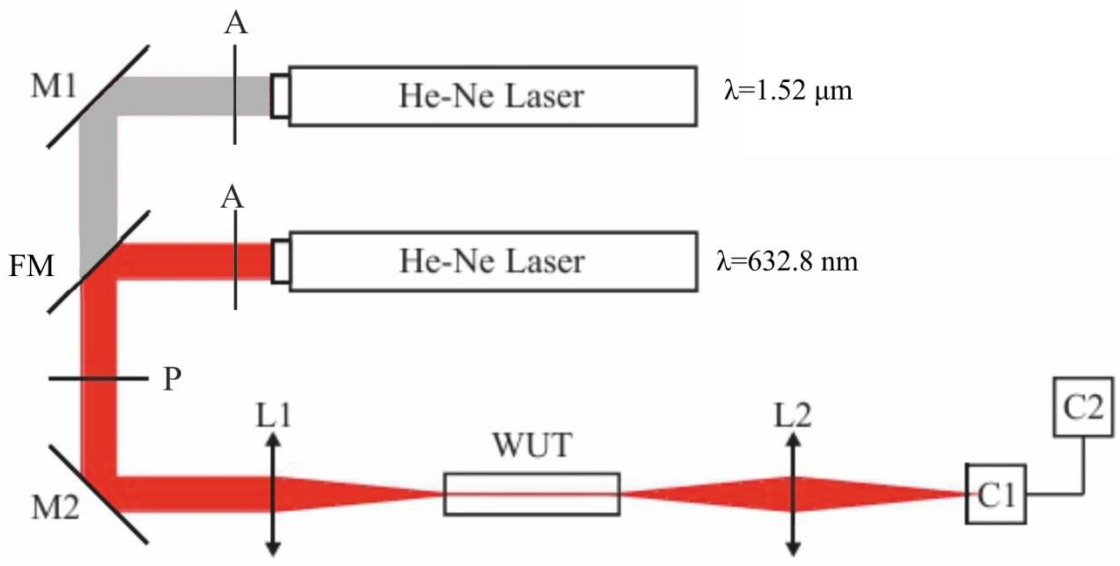

Figure 5.1 Near-field mode intensity profile measurement setup. (M1, M2: mirrors; FM: flipping mirror; A: attenuator; P: polarizer; L1 and L2: objective lenses; WUT: waveguide under test; C1: CCD Camera and C2: the computer.)

Once the image of the mode was recorded the normalised intensity profiles along horizontal (x-axis) and vertical directions (z-axis) were generated using beam-profiling software. A glass graticule (10 μm feature size) was used to calibrate the size of the mode profile captured by the CCD. The depth and with of the waveguide modes were then measured. The waveguides were typically written along the y-direction of the crystal, therefore the lateral direction is along "x" and of course the depth is always along "z" as illustrated in FIG. 7

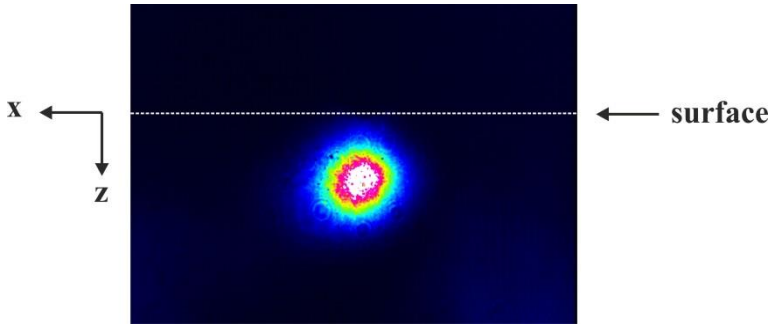

Figure 5.2 Nomenclature of mode profiles used in this thesis with the z direction specifying the crystal depth and x direction the spatial direction equivalent to across the beam. The white dashed line indicates the crystal surface.

5.4.1 Channel waveguides on the +z face of a-Si/CLN

TM modes at λ=633 nm

Near field TM mode intensity profiles for waveguide channels written on the +z of a-Si/CLN are shown in Figure 5.3. These channels were written using increasing writing intensity and a constant writing speed of 1 mm/sec. As the intensity of the laser increases, the profiles become wider, deeper and the propagation becomes multimode. At an intensity of 0.49 MW/cm^2, single mode propagation is observed (Figure 5.3a). The higher order mode propagation that is observed at higher writing intensities suggests that the central region of the waveguide, close to the surface, has suffered damage because the propagating mode seems to avoid that particular volume. As a result of this surface damage the optical mode shifts further into the bulk. For laser intensities lower than 0.49 MW/cm^2 the induced refractive index is too small to support a propagating mode and lossy diffuse mode profiles are observed (not shown here).

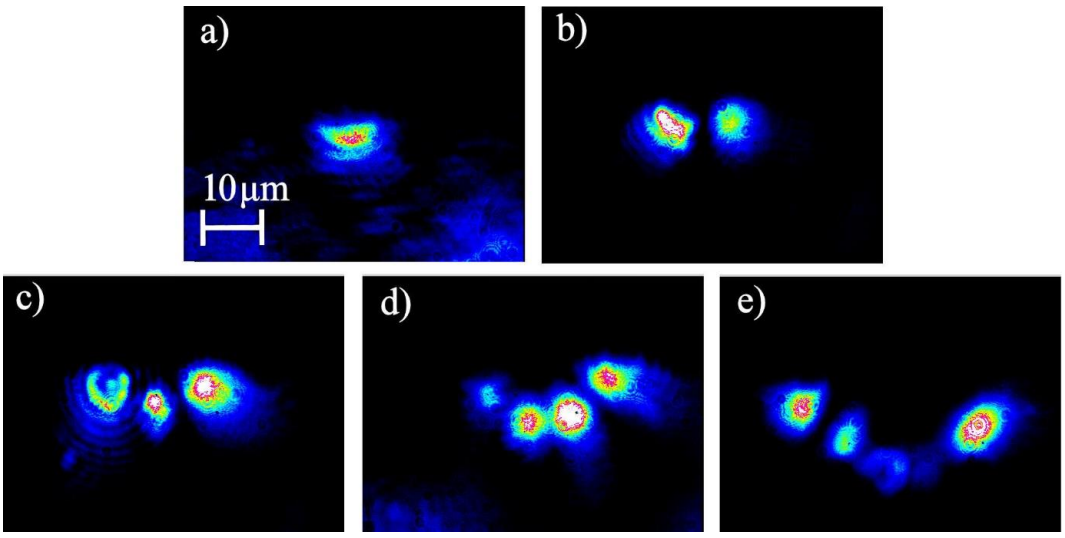

Figure 5.3 Near field waveguide mode profiles for channels written on the +z face at wavelength of 633nm, TM polarisation written under different writing intensities at 1mm/sec. Intensities used: a) 0.49 MW/cm^2, b) 0.63 MW/cm^2, c) 0.70 MW/cm^2, d) 0.77 MW/cm^2 and e) 1.12 MW/cm^2.

The 1/e^2 intensity mode widths and depths for all writing conditions were measured and the results are shown in Figure 5.4. The SM notation indicates the single mode waveguides. The mode widths (Figure 5.4a) and the mode depths (Figure 5.4b) increase with increasing intensity as the propagation changes from single to multimode.

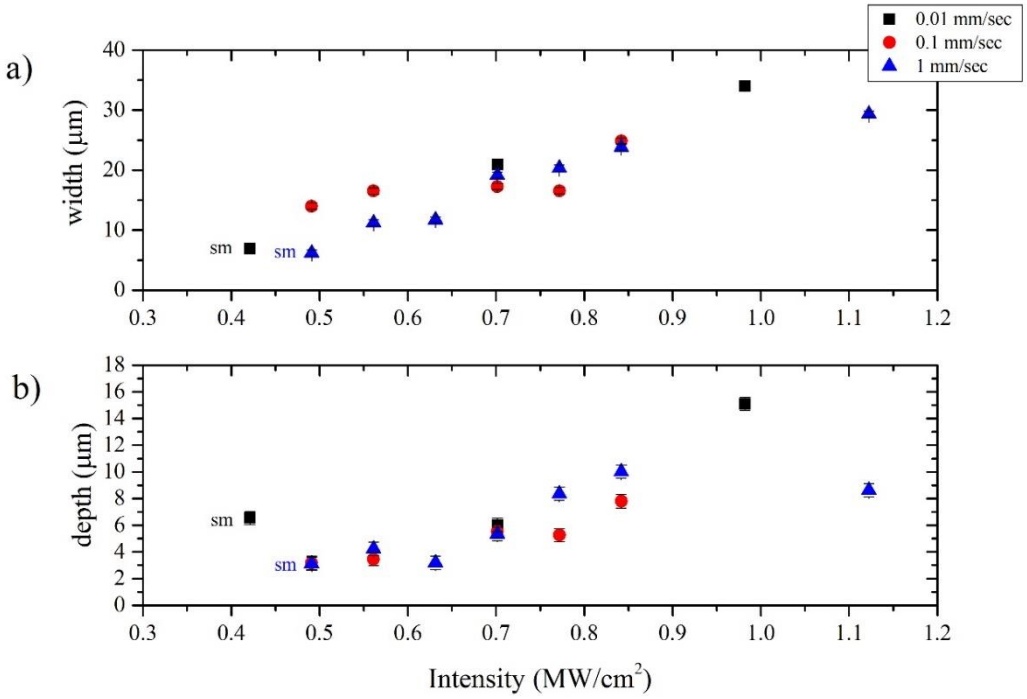

Figure 5.4 a) mode width and b) mode depth at λ=633 nm of TM polarisation corresponding to waveguides written under different writing intensities and writing speeds. The SM notation indicates the single mode waveguides.

Another observation from this graph is that the writing velocity has a much smaller effect on the optical characteristics of the written waveguides compared to the writing intensity.

TE modes at λ=633 nm

In previous reports of laser writing of waveguides in lithium niobate using UV laser irradiation only TM modes could be excited [13], which corresponds to a change in the extra-ordinary refractive index (n_e). In this case however, we could also observe waveguide propagation in the TE polarisation which indicates an increase of the ordinary refractive index (n_o) at λ=633 nm.

Figure 5.5 shows the near-field intensity profiles of three waveguides written under the following conditions: writing speed of 1mm/sec, spot size of ~3.5 μm and laser intensities of a) 0.77 MW/cm^2, b) 0.84 MW/cm^2 and c) 1.12 MW/cm^2. Note that all the waveguides modes correspond to the fundamental order. At lower intensities, below 0.77 MW/cm^2, no waveguide propagation was observed. These observations regarding the propagation mode and the intensity range where TE waveguides were observed suggests that the n_o refractive index change is smaller as compared to the n_e change.

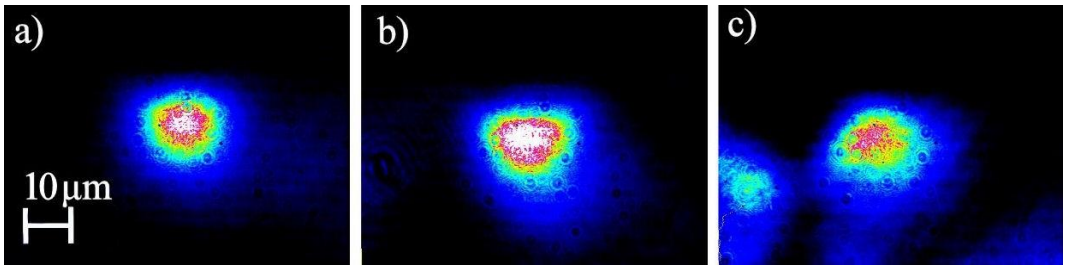

Figure 5.5 Mode profiles for +z a-Si/CLN waveguides at wavelength of 633nm of TE polarisation, written under different writing intensities at 1mm/sec. Intensities are: a) 0.77 MW/cm^2, b) 0.84 MW/cm^2 and c) 1.12 MW/cm^2.

Measurements of the near-field intensity profiles, plots of the mode width and depth versus the writing intensities was obtained as shown in Figure 5.6, representing that the mode size of the waveguides is not changing significantly as the laser intensity increases.

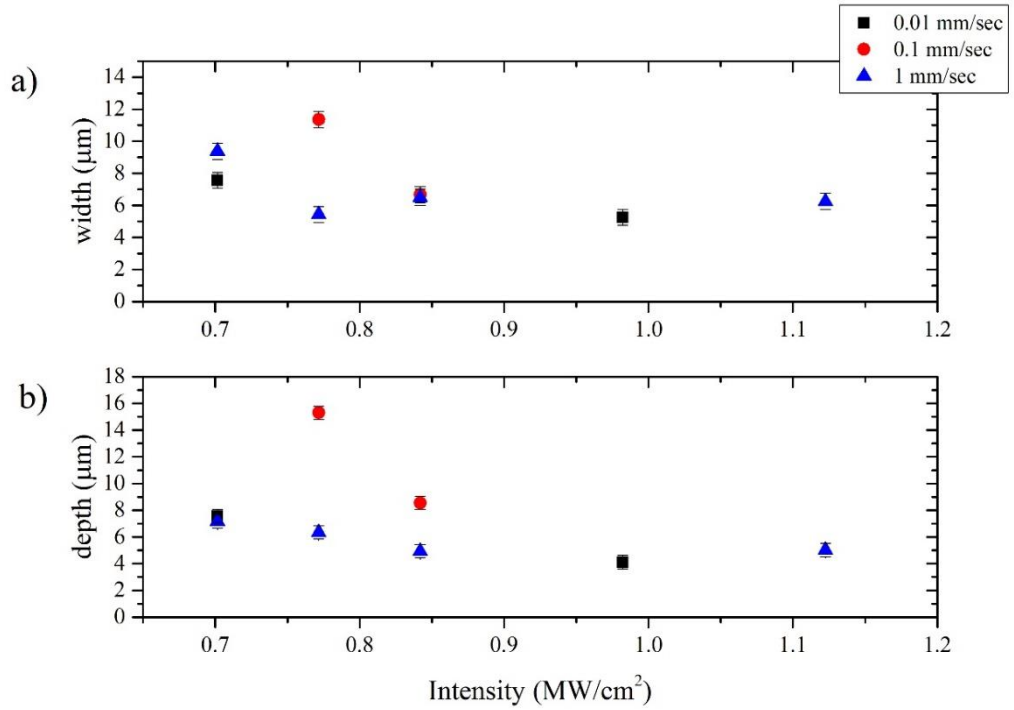

Figure 5.6 a) mode width and b) mode depth at λ=633 nm of TE polarisation corresponding to waveguides written under different writing intensities and writing speeds.

Unlike the ordinary index n_o, the extraordinary index n_e strongly depends on the stoichiometry of the crystal. Specifically, n_e increases as Li_2O is removed from the crystal but n_o is practically unaffected [14]. Therefore, the observation of TE mode propagation cannot be attributed to the changes in the concentration of lithium that has been held responsible for the formation of the UV written waveguides that were observed in [1], because lithium concentration only affects the n_e refractive index value. It is possible that there are other contributions to the observed waveguide formation associated perhaps with stress on the Si/CLN interface and also some diffusion of Si into CLN. A further discussion will be given on the section of the proposed explanation for the formation of the waveguides due to visible irradiation on a-Si/CLN samples in section 5.5.

TM modes at λ=1.52 μm

The investigation of waveguide transmission at telecommunication wavelengths is presented here. The beam from a He-Ne operating in the IR wavelength λ=1.52 μm was coupled to the laser written waveguides, using the experimental apparatus described in Figure 5.1. Typical near-field intensity profiles of the propagating modes, captured by an IR camera are shown in Figure 5.7.

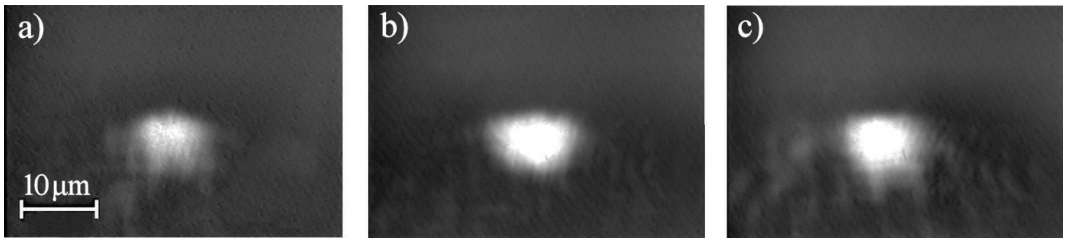

Figure 5.7 TM mode profiles for waveguides at wavelength of 1.52μm of TM polarisation, written under different writing intensities at 1mm/sec. Intensities are: a) 0.77 MW/cm^2, b) 0.84 MW/cm^2 and c) 1.12 MW/cm^2.

The corresponding mode size measurements as a function of the writing intensity for different writing speeds yield the plots which are shown in Figure 5.8. At λ=1.52μm only propagation in the fundamental mode was observed. Interestingly previous results obtained using UV-laser irradiation did not show propagation at telecommunication wavelengths. It is rather difficult however to directly compare the current experimental results that correspond to indirect irradiation (through the Si layer) with previous results obtained with UV irradiation. This is mainly due to the fact that the spot sizes in this case are larger as compared with the UV case which could account for the propagation in the IR. Another observation is that the IR propagation modes are located close to the surface. The corresponding modes in the visible spectrum where located deeper in the crystal. This behaviour of the modes was attributed to the possibility of surface damage that increased the scattering loss close to the surface. The close-to-the-surface location of the IR modes could be an indication that Si has diffused into the substrate during the laser irradiation. Si in CLN would induce loss in the visible, due to absorption but not in the IR.

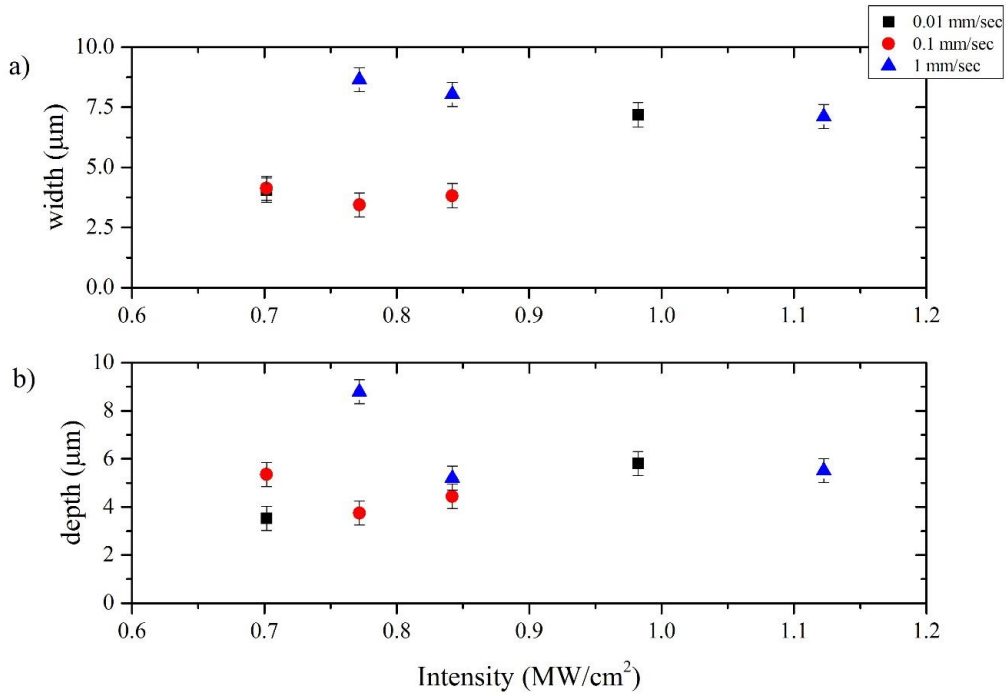

Figure 5.8 a) mode width and b) depth at λ=1.52 μm for TM polarisation corresponding to waveguides written under different writing intensities and writing speeds.

Removing the a-Si over-layer

During the laser irradiation process the a-Si over-layer reaches very high temperatures, as high as the melting point of the material. After cooling the crystalized Si film and the CLN substrate will contract, not necessarily at the same rate. It is expected therefore that some amount of stress will be present at the Si/CLN interface after the laser processing. This stress could contribute to the observed refractive index change. To assess the influence of the over-layer on the propagating mode, the a-Si thin film was removed using KOH and mode profile measurements were repeated. For comparison the near field intensity profiles for the a-Si coated waveguides are shown in Figure 5.9 together with the near field profiles at λ=633nm after the removal of the a-Si over-layer for TM polarisation. A general observation regarding the propagating modes after the removal of the Si over-layer is that the confinement is now worse. Note that the fundamental mode (Figure 5.9a2) after the removal of Si has become larger as compared to the mode before Si removal (Figure 5.9a1). The modes that correspond to higher writing intensities have changed accordingly. According to the mode dimension calculations for all the waveguides, which are presented in Figure 5.10, there is no suggestion of a specific trend after the removal of Si.

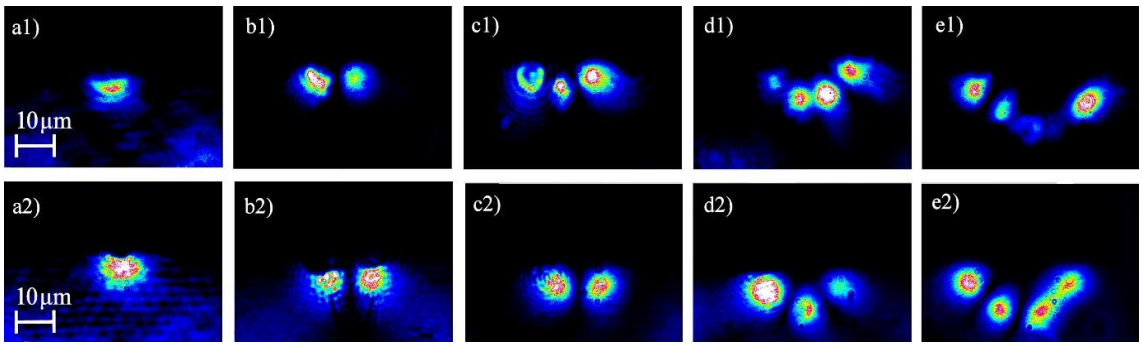

Figure 5.9 Mode profiles of channel waveguides written under writing speed of 1mm/sec and laser intensities: a) 0.49 MW/cm^2, b) 0.63 MW/cm^2, c) 0.70 MW/cm^2, d) 0.77 MW/cm^2 and e) 1.12 MW/cm^2, before (a1, b1, c1, d1, e1) and after (a2, b2, c2, d2, e2) removal of the Si film. Laser writing speed: 1mm/sec.

In Figure 5.10, where the size of the modes is taken at the 1/e^2 position of the outer lobes for all the writing conditions used, the solid data points correspond to a-Si over-layer and the open data points correspond to measurements after the removal of the a-Si film.

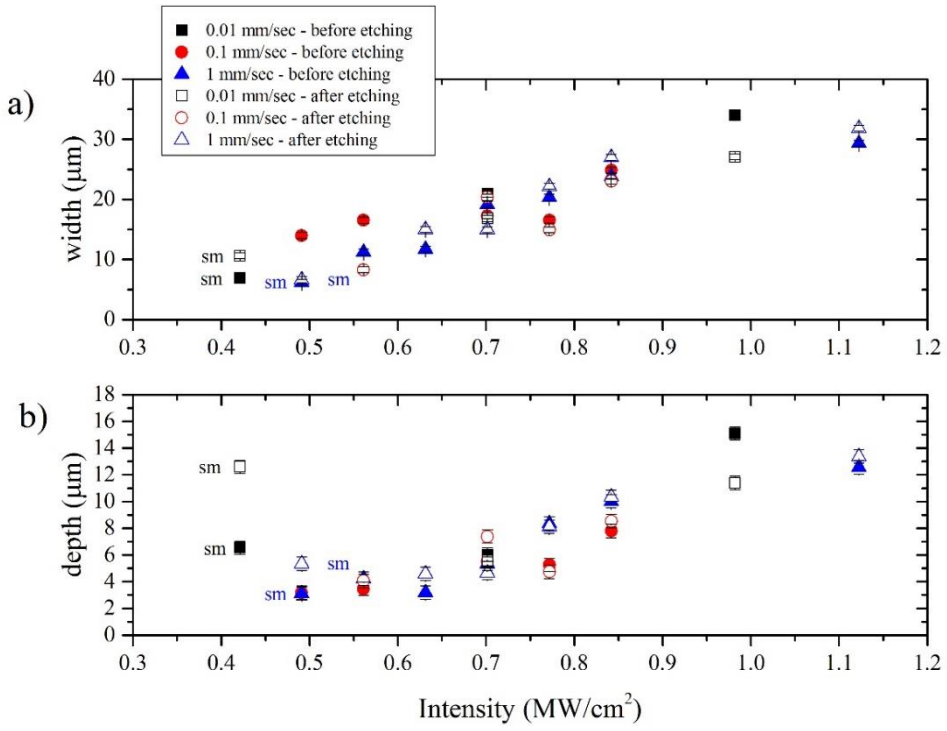

Figure 5.10 a) Mode width and b) mode depth at λ=633 nm of TM polarisation corresponding to waveguides written under different writing intensities and writing speeds. Solid and open data points correspond to measurements taken with and without the a-Si over-layer on top, respectively. The SM notation indicates the single mode waveguides.

Mode profiles for TE polarisation at λ=633 nm were obtained and a plot was yield, comparing the mode sizes of the waveguides before and after the removal of the a-Si film as a function of the writing intensity, as can be seen in Figure 5.11, for constant writing speed of 1mm/sec.

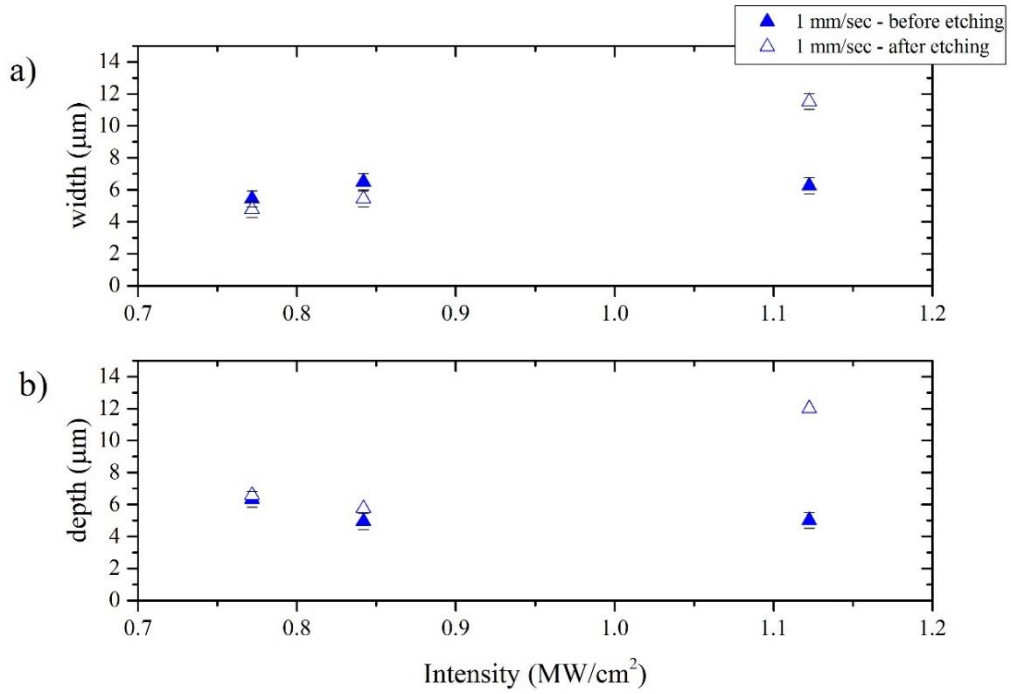

Figure 5.11 a) Mode width and b) mode depth at λ=633 nm of TE polarisation corresponding to waveguides written under different writing intensities and writing speed of 1mm/sec. Solid and open data points correspond to measurements taken with and without the a-Si over-layer on top, respectively.

5.4.2 Propagation Loss

In order to investigate the optical propagation loss of the laser written waveguides another sample was fabricated using a smaller laser spot radius this time (~1.8μm). A set of channel waveguides was fabricated consisting of channels corresponding to different laser intensities and writing speeds. The sample was exposed on the +z face and scanned across its y- crystallographic direction at laser intensities ranging from 0.47 MW/cm^2 to 0.7 MW/cm^2 with a writing speed ranging from 0.016mm/sec to 0.16mm/sec. The propagation loss of the waveguides was measured using the cutback method for TM and TE propagating modes at 633 nm wavelength and for TM propagating modes, which are the only propagating modes at 1.52 μm wavelength.

Using the experimental set-up shown in Figure 5.1, a power meter was placed in the position of the CCD camera and an iris diaphragm was used to preferentially collect the light corresponding to the propagating mode by blocking the uncoupled light. The transmitted laser power was measured

for each waveguide channel. The sample was then shortened by lapping removing ~1-1.5mm from the output edge and the transmission measurement was repeated. This process was repeated five times allowing the measurement of the transmission over a change of propagation length that is approximately ~5.1 mm.

The propagation loss per unit length were derived from the slope of the linear fitting on the average intensities of the five different length and the y-intercept of the linear fitting provides an indication of the coupling loss.

TM polarisation of incident beam: λ=633nm.

Figure 5.12 illustrates the total loss in comparison with the waveguide length value for TM polarisation at λ=633 nm.

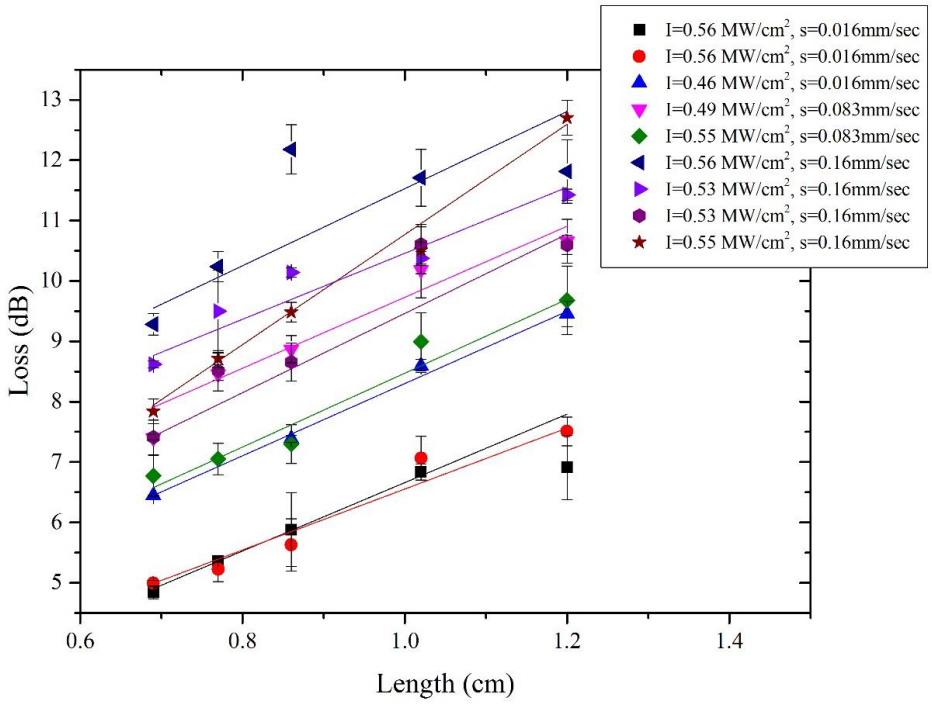

Figure 5.12 Loss versus length of a waveguide written on the +z face of a-Si/CLN sample with different writing conditions. Measurements taken for TM polarisation of incident beam of λ=633nm.

The lowest propagation loss found to be 5.04 ± 0.37 dB/cm and corresponds to waveguide written under writing intensity of 0.56 MW/cm^2 and writing speed of 0.016 mm/sec. Table 5.1 summarises the calculated propagation loss of the explored exposure conditions.

Writing Speed (mm/sec)	Writing intensity (MW/cm^2)	Propagation Loss (dB/cm)	Error
0.016	0.46	5.98051	0.31015
0.016	0.56	5.66937	0.47791
0.016	0.56	5.04812	0.37986
0.083	0.49	5.87768	0.94926
0.083	0.55	6.11783	0.91394
0.16	0.53	5.46395	0.77013
0.16	0.53	6.56518	0.65436
0.16	0.55	9.12279	0.48004

Table 5.1 Measured TM modes at λ=633 nm

Overall, the measured loss was found to be between 5.0 and 6.5 dB/cm throughout the writing conditions used here. Exception of this trend can be seen for a waveguide written with laser intensity of 0.55 MW/cm^2 and speed of 0.16 mm/sec, which was found to be 9.12 ± 0.48 dB/cm, which could be attributed to fabrication error of this particular waveguide. The propagation loss as a function of the laser power and scanning speed is shown in Figure 5.13. The lowest propagation loss was observed for a combination of higher intensity and slow speed. Perhaps the relatively high propagation loss in this set of waveguides is due to the smaller spot size that was used for the fabrication of these channels as the smaller physical dimensions could account for more lossy structures. This could explain why the lower propagation loss has been observed for high intensity fast writing, which is expected to produce a higher refractive index change. Another source of propagation loss could be associated with the Si film which will absorb light at λ=633 nm.

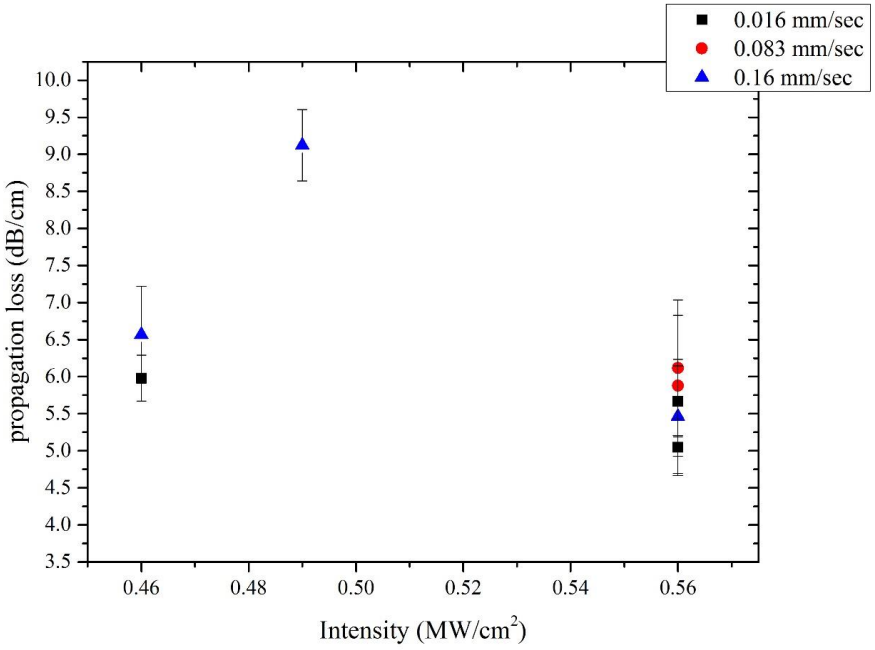

Figure 5.13 Comparison of waveguide propagation and loss versus writing intensity for waveguides written on +z face of a-Si/CLN under different writing speeds. Measurements taken for TM polarisation of incident beam of λ=633nm.

TE polarisation of incident beam: λ=633nm.

Using a TE polarisation of incident beam of λ=633 nm measurements of the propagation loss were also taken and the calculated values are shown in Table 5.2. The lowest obtained value of propagation loss found to be 4.53 ± 0.88 dB/cm and the higher 6.39 ± 0.44 dB/cm.

Writing Speed (mm/sec)	**Writing intensity (MW/cm^2)**	**Propagation Loss (dB/cm)**	**Error**
0.016	0.6	5.85528	0.34624
0.016	0.6	5.74157	1.0893
0.083	0.56	6.30798	0.76447
0.083	0.56	6.06456	0.8454
0.083	0.55	4.53955	0.88193
0.083	0.53	6.77208	1.1647
0.083	0.53	5.18612	0.51009
0.083	0.53	6.39974	0.44617
0.083	0.49	5.03791	1.44002
0.083	0.49	6.05228	1.09986
0.16	0.53	3.81626	0.90793

Table 5.2 Measured TE modes at λ=633 nm

In general, the calculated propagation loss for polarization of TE, was found to be varying between 5.0 and 6.7 dB/cm throughout the writing conditions used, which are similar as for the TM polarization.

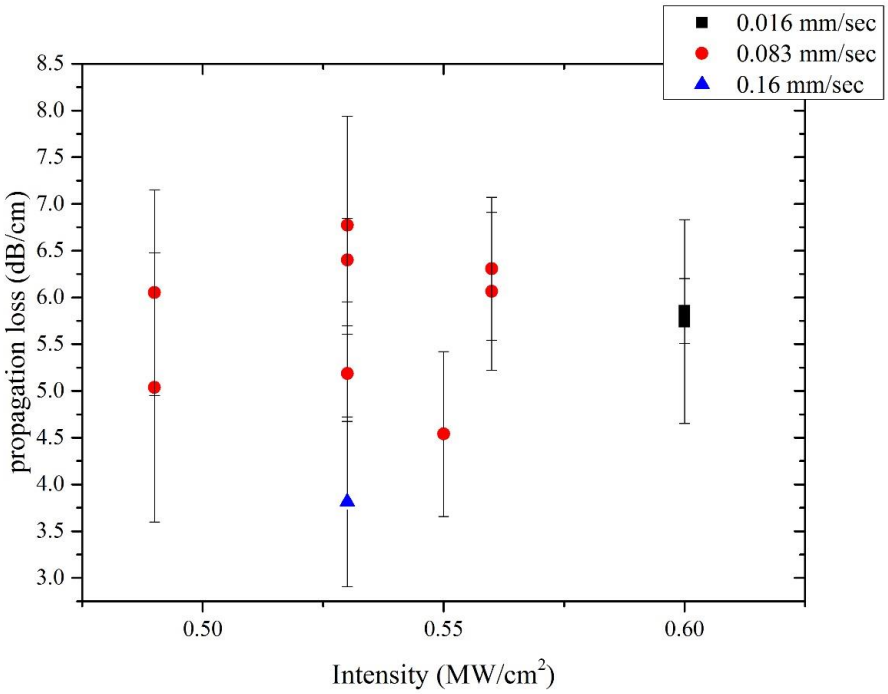

Figure 5.14 Comparison of waveguide propagation and loss versus writing intensity for waveguides written on +z face of a-Si/CLN under different writing speeds. Measurements taken for TE polarisation at 633nm

TM polarisation: λ=1.52μm.

Same results were taken for incident beam of wavelength of TM polarisation at λ=1.52 μm as well, though only for waveguides written at writing speed of 0.016 mm/sec. The rest of the fabricated waveguides found to be lossy which make their calculation challenging. Figure 5.15 illustrates these measurements and Table 5.3 the obtained values of the propagation loss. The lowest propagation loss were calculated at 3.69 ± 0.12 dB/cm on a waveguide written under writing intensity of 0.49 MW/cm^2.

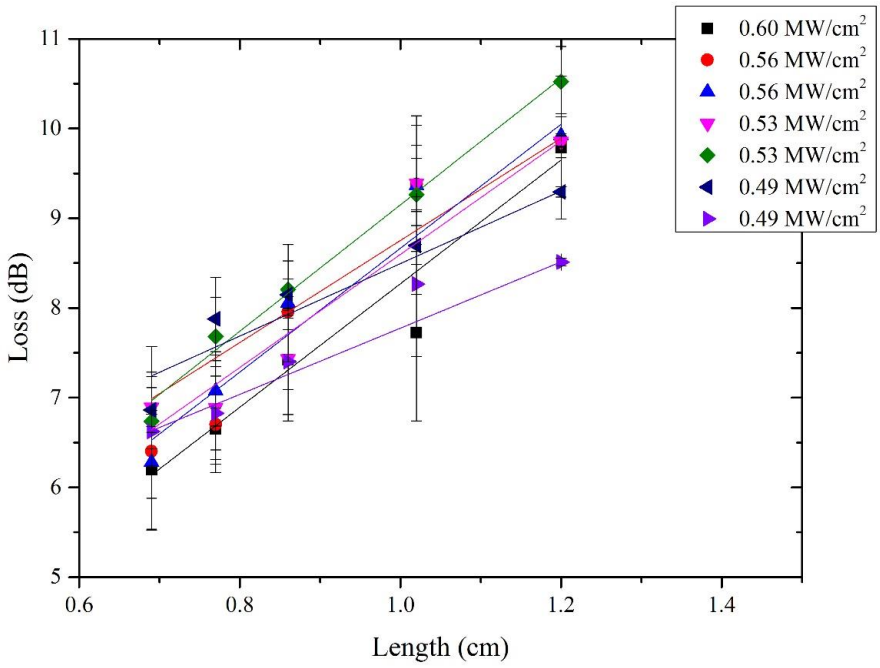

Figure 5.15 Loss versus length of a waveguide written on the +z face of a-Si/CLN sample under different writing intensity and constant writing speed of 0.016mm/sec. Mode profile of the measured waveguide at a wavelength of 1.52 μm of TE polarisation.

Writing Speed (mm/sec)	**Writing intensity (MW/cm^2)**	**Propagation Loss (dB/cm)**	**Error**
0.016	0.6	6.88301	0.77796
0.016	0.56	5.69135	0.3249
0.016	0.56	6.90242	0.7132
0.016	0.53	6.30616	0.56536
0.016	0.53	7.04408	0.36831
0.016	0.49	4.04019	0.44082
0.016	0.49	3.69149	0.12613

Table 5.3 Measured TM modes at λ=1.52 μm

A plot of propagation loss in comparison with the writing intensity was also yield, shown in Figure 5.16 where the lowest laser intensity used appears to exhibit the lowest total loss.

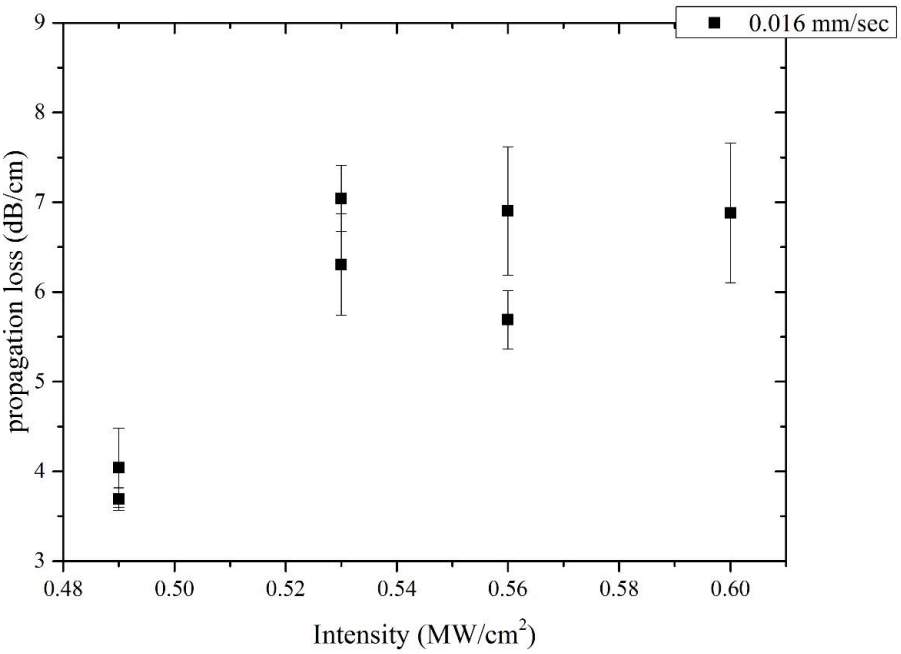

Figure 5.16 Comparison of waveguide propagation loss versus writing intensity for waveguides written on +z face of a-Si/CLN with constant writing speed of 0.016mm/sec. Measurements taken for TM polarisation of incident beam of λ=1.52 μn.

The lowest loss is observed at 1.52 μm, which suggests that absorption in Si could be a source of loss at visible wavelengths.

5.4.3 Channel waveguides on the -z face of a-Si/CLN

TM modes at λ=633 nm

Near field intensity profiles of waveguides fabricated on –z face of a-Si/CLN displayed a difference in the mode sizes of waveguides written on +z face under same writing conditions as seen in Figure 5.17. The spot size was ~3.5 μm for both samples.

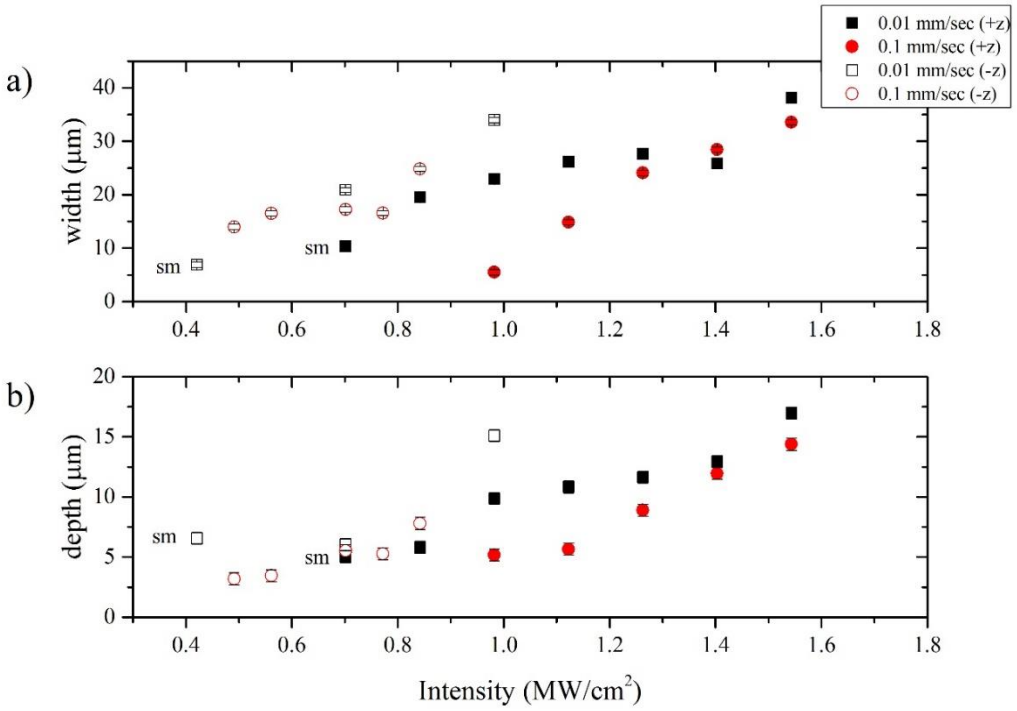

Figure 5.17 Comparison of a) mode width and b) mode depth at λ=633nm of TM polarisation, between waveguides written on +z face (solid data spots) and –z face (open data spots) of a-Si/CLN samples, corresponding to waveguides written under different writing intensities and writing speeds. The SM notation indicates which waveguides are single mode.

In general, lower laser intensities were required to obtain same size waveguide when irradiating on –z face than on +z face a-Si/CLN. For instance, a single-mode waveguide on –z face demands ~ 0.3 MW/cm^2 lower intensity for writing speed of 0.01 mm/sec. The reason for this effect is not clearly understood at the moment.

TE modes at λ=633 nm

Investigation on the mode profiles of waveguides written on the –z face sample for incident beam of λ=633nm and TE polarisation revealed difficulty on exciting this kind of modes. As seen on the TM analysis, the depth and width of the modes on waveguides written on –z face found to be smaller than on the +z face, indicating a smaller refractive index change. Additionally, the extraordinary refractive index change, which, is responsible for TE modes proved to be smaller than the ordinary refractive index change, therefore the accumulation of these two observations might be responsible for the poor optical confinement for TE polarisation on –z face samples.

TM modes at λ=1.52 μm

Near field intensity profile analysis for infrared wavelength was made on –z face a-Si/CLN samples as well. Figure 5.18 compares the measured $1/e^2$ mode size values of the same waveguides between visible and infrared wavelength of incident beam. Under these writing conditions, all the IR propagation modes appeared to be single-mode, but only the waveguide that corresponded to the highest written intensity of 0.56 MW/cm^2 had strong confinement. In general, all the IR modes were located to the surface, however due to the lossy confinement of the waveguide fabricated with intensity lower than 0.56 MW/cm^2, their mode depth was measured higher in contrast with the visible modes of the same waveguides.

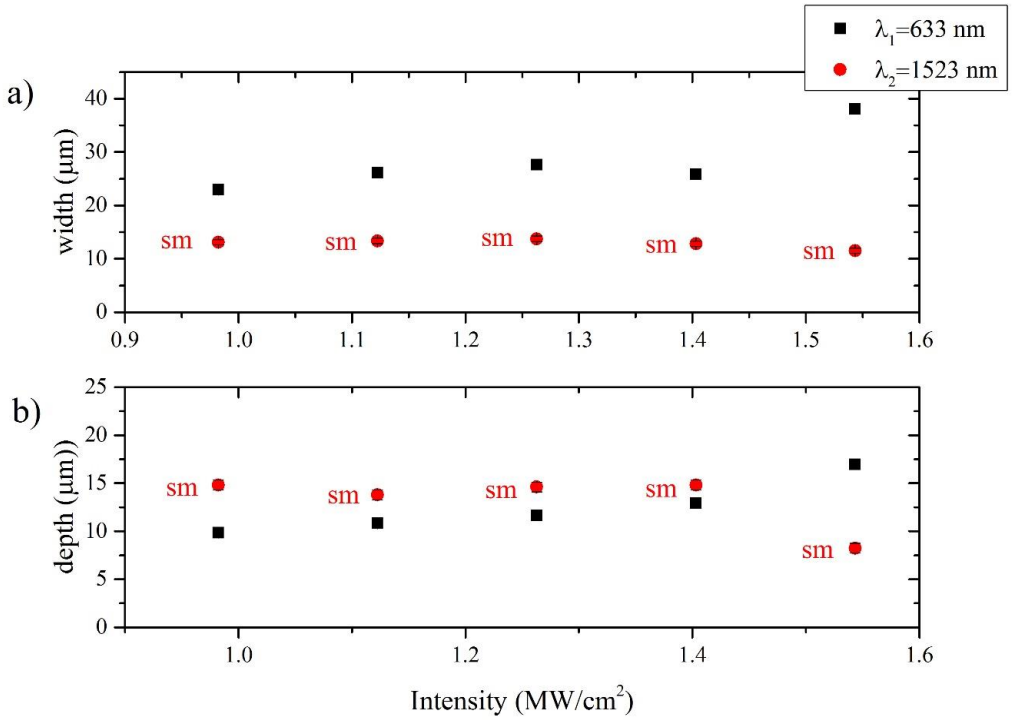

Figure 5.18 Comparison of $1/e^2$ measurements of a) mode width and b) mode depth between λ=633 nm (black dots) and λ=1.52 μm (red dots) of TM polarisation corresponding to waveguides written under different writing intensities and constant writing speed of 0.01mm/sec. The SM notation indicates the single mode waveguides.

Removing the a-Si over-layer

The effect of the optical confinement increase afterwards the KOH etching step was also observed in the –z face a-Si/CLN samples, though in a small extent. Figure 5.19 displays the $1/e^2$ values measured from the near-field intensities profiles of waveguides written under constant writing speed of 0.01mm/sec on –z face of a-Si/CLN film, before and after the film removal.

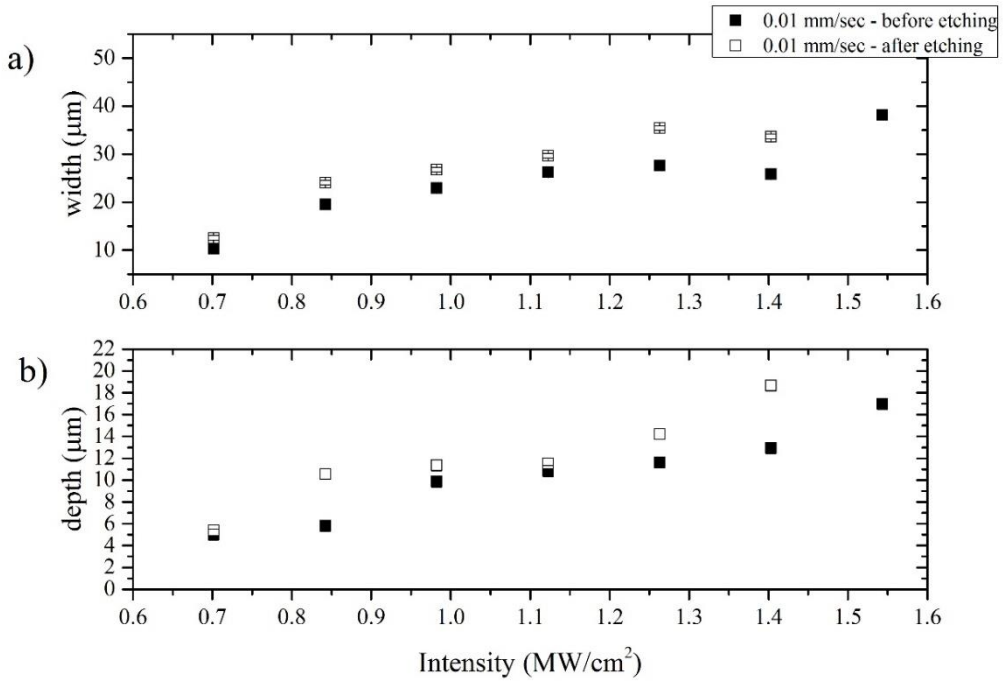

Figure 5.19 Measurements of $1/e^2$ values of waveguides written under different writing intensities at 0.01mm/sec on -z face of a-Si/CLN. The top graph shows the mode widths and the bottom one the depth versus the writing intensities used.

5.5 Proposed mechanism for the waveguide formation

The mechanism for the waveguide formation on the a-Si/CLN crystal during the visible laser annealing should be similar mechanism as in the UV-written waveguides on CLN. More precisely, the high absorption of the a-Si layer induces the temperature on the CLN substrate forming a great temperature gradient forcing the Li ions to migrate by diffusion but also under the influence of the pyroelectric field, which is formed as the heated volume cools down. This thermal mechanism is also responsible for the UV-induced poling-inhibition, which was also observed here as well. The poling-inhibition process is described in the next section.

Moreover, a-Si/CLN waveguides exhibit transmission not only of TM modes (which is the case for UV-written waveguides on CLN), but in TE modes as well, showing an increase in both the extraordinary and ordinary refractive indices. This indicates that there might be other effects apart from Li ion diffusion that takes place and are responsible for the ordinary refractive index change. It is suggested that it is attributed to an interfacial stress on CLN induced by the crystallized layer of Si.

5.6 Poling inhibition on a-Si/CLN crystals

5.6.1 Introduction

A route to overcome the limitations of UV-laser induced domain engineering (limited depth, surface damage) to produce domain structures which are suitable for photonic applications, could be to irradiate a light absorbing thin film deposited on the polar faces of CLN crystals. In this section we will present experimental work, which investigates the formation of PI domains using visible (λ=488 nm) c.w laser irradiation on a CLN crystal coated with an a-Si film. Irradiation of an a-Si thin film covered CLN crystal surface with visible laser radiation have been shown in the previous section to reproduce waveguiding results that were previously obtained with UV laser irradiation. As the physical origin of the optical waveguide writing and PI (or spontaneous) domain formation originates from laser induced temperature gradients in the crystal we expect that it will be possible to reproduce the UV laser induced poling effects also in the a-Si/CLN system but this time by using visible laser irradiation.

5.6.2 Experimental procedures

The samples that were used for the ferroelectric domain inversion experiments were fabricated using the same methods and writing conditions as described in the waveguide writing section 5.2. The laser irradiation conditions (laser intensity and writing speed) were also within the same range that were used for the channel waveguide experiments; intensities: 0.2-1.6 MW/cm^2, writing speeds: 0.01-1mm/sec. A laser beam radius of ~3.5 μm was used.

5.6.3 Laser-induced poling inhibition in a-Si/CLN using a visible irradiation

PI domains characteristics: depth, width and surface quality: In order to perform the poling step, which is necessary for the PI domain inversion the a-Si film was removed, using KOH, to expose the +z face of the crystal. The crystal was then uniformly EFP poled using the process that was described in section 5.4.1, ensuring smooth and slow domain wall velocity. The voltage was ramped up until nucleation was observed and then was kept at a constant level throughout the remaining poling process 9.6 kV.

The investigation of the PI domain characteristics was performed again by wedge polishing at ~ 5^o and brief etching in HF acid (48%) for 3 min at room temperature, producing an etched depth of ~30 nm on the –z face. The etched surface topography provided sufficient contrast to allow investigation of the PI domains using optical microscopy. The revealed PI domains on the +z face of a-Si/CLN samples can be seen in Figure 5.20.

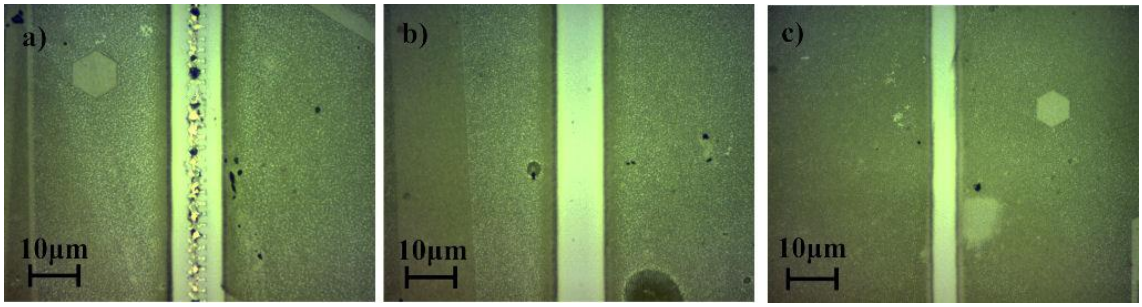

Figure 5.20 Microscope images of HF etched PI domains. The irradiation conditions are: constant scanning speed at 60mm/min and laser intensities at a) 0.63 MW/cm^2, b) 0.56 MW/cm^2 and c) 0.28 MW/cm^2.

Combining the wedge polishing and the HF etching the stretched depth profile is revealed. The surface topography of the etched wedge can be seen clearly in the SEM images [15] shown in Figure 5.21. These SEM images were used to measure the domain size as a function of the fabrication conditions.

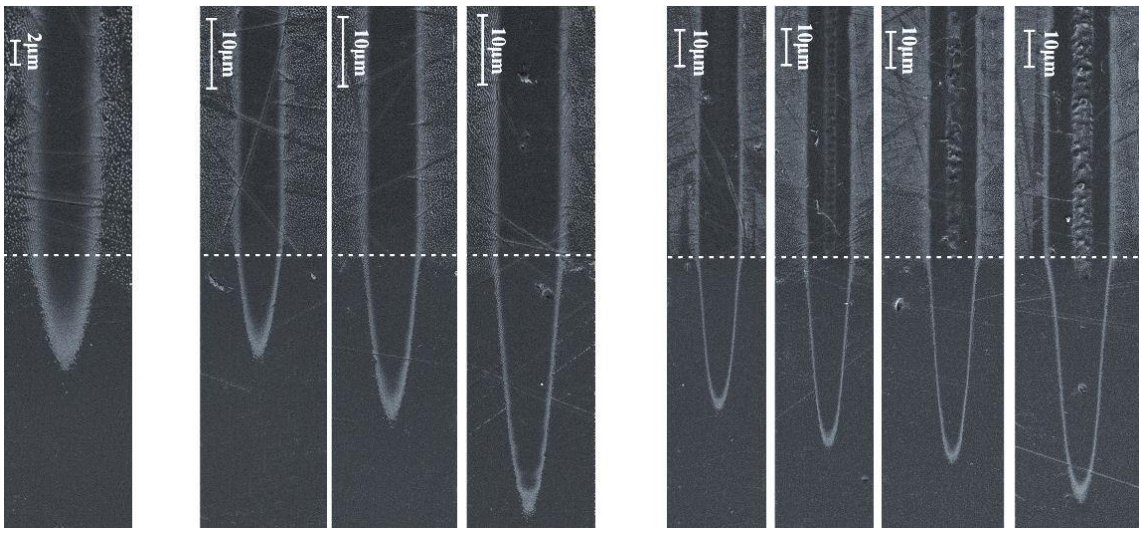

Figure 5.21 SEM images of the wedge-polished PI domains fabricated under different laser intensities keeping the speed constant at 0.1mm/sec.

Additional evidence for the quality of the PI domains that were formed as a result of the irradiation of the a-Si film on the +z face of the crystal was provided by investigation of the surface using PFM. The PFM scans confirm the domain inversion but also reveals that under certain conditions the heat coupled from the Si film to the crystal can cause significant damage of the surface which leads to a local reduction of the ferroelectricity as shown in Figure 5.22.

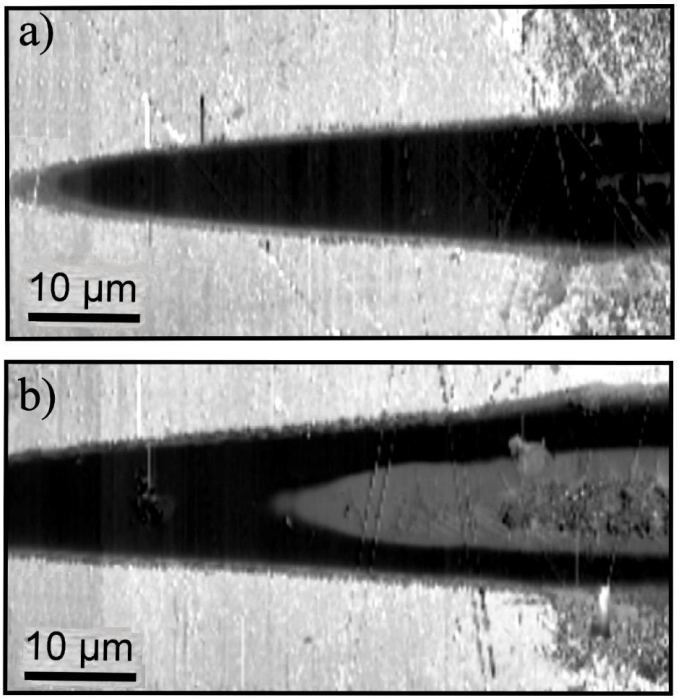

Figure 5.22 PFM images PI domains

The SEM images presented in Figure 5.21, which correspond to writing speed of 0.1 mm/sec exhibit some surface damage for laser intensities above 0.7 MW/cm^2, which can be seen along the laser irradiated tracks on the top side of the horizontal dash line that corresponds to the original +z face of the sample. Surface damage was also seen in previous UV experiments in which case was the result of direct absorption form the crystal [16]. At the lower limit of laser intensities the resulting PI domains consist of scattered nano-domains. The profiles of the visible laser irradiated tracks shows also grainy etch resistant features, which is a characteristic of isolated nano-domains, which have formed within the heat affected zone that extends deeper into the crystal with increasing irradiating laser intensity. From the SEM observations, it reveals that there is a defined zone of roughness on the surface of the samples that corresponds to remains of the a-Si thin film after the KOH etching.

The size (depth and width) of the PI domains fabricated under different writing conditions, measured from the SEM images of the stretched depth profiles of the PI domains, as a function of the writing laser intensity is shown in Figure 5.23.

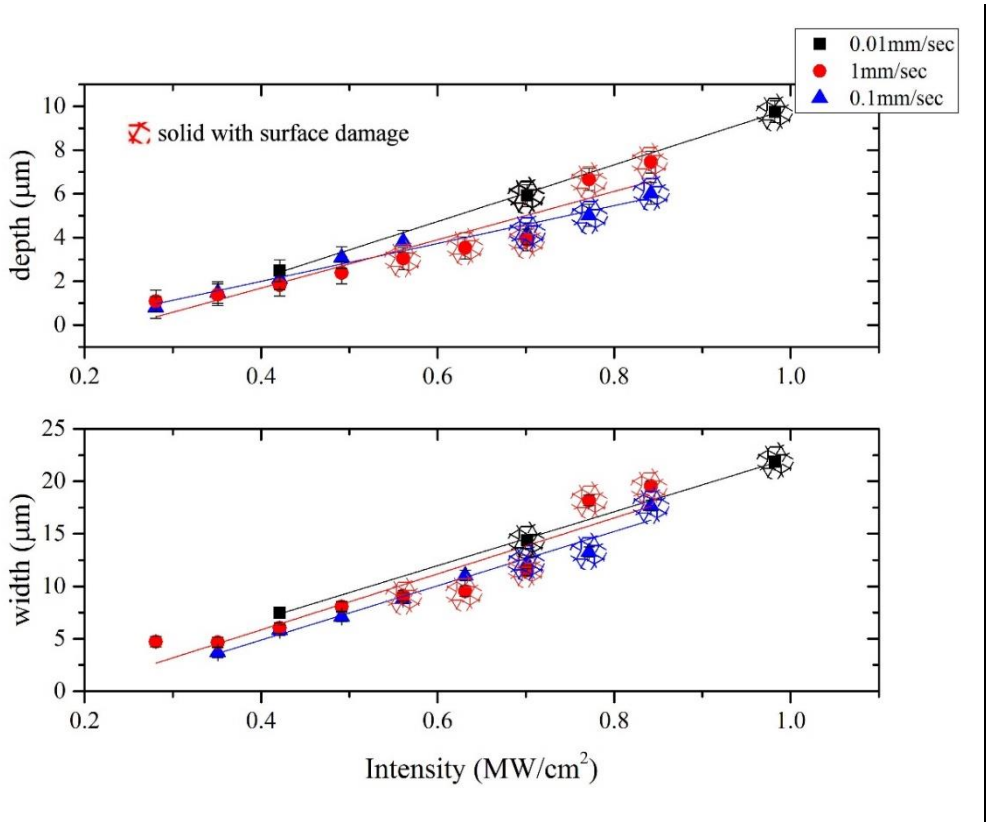

Figure 5.23 The depth and width of PI domains in a-Si/CLN plotted as a function of the writing laser intensity under different writing speeds.

The deepest solid PI domain without any surface damage that was obtained has a depth of 3.8 μm. This depth measurement in contrast with the deeper solid PI domain fabricated by UV-laser irradiation of 244nm wavelength on a plain CLN crystal (2.5μm) [16], [4], displays an increase of depth up to 34% which is an encouraging result, suggesting some degree of domain depth control without risking damaging the crystal surface. In addition, different writing speeds which differ by one order of magnitude minor effect appears to have on PI domain size, which in some cases the values are within the limit of the error bar.

The largest width value of PI domains was measured to be ~11 μm for PI solid domain without any surface damage which is almost double the size of the spot size used. This observation suggests that the heat diffuses well beyond the irradiated area possibly due to the different heat conductivity of the film. The depth and width data were also plotted as depth vs width. The plot is shown in Figure 5.24. As indicated by the linear fits, the data generally follows a linear relationship showing that domain depth and width is larger with higher writing intensity, which is similar behaviour as in the experiments of UV-laser induced PI.

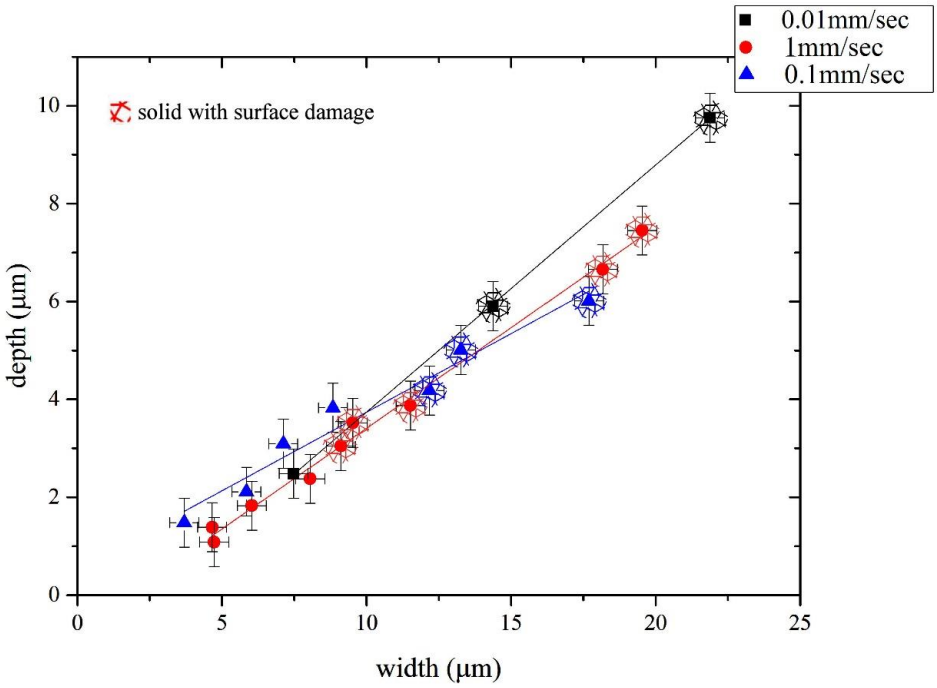

Figure 5.24 PI domain depth versus width for different writing speeds keeping constant the writing speed at 6mm/min. The red line corresponds to linear fitting.

In order to investigate the dependence of the PI domain size on the writing speed, plots of the PI domain dimensions as a function of the writing speed were produced and shown in Figure 5.25. The writing laser intensities here are I_1=0.42 MW/cm^2 and I_2=0.7 MW/cm^2 where the first one corresponds to solid domains without damage and the latter for a PI with surface damage, for all writing speeds.

Changing the writing speed effectively, modifies the exposure time of the surface, which adjusts the duration for each point of the exposed track is subjected to extreme, close to melting point, temperatures. These measurements suggest that the range of the electrostatic barrier that produces the PI domains [16], [17] is pushed further away from the heating source confirming the results that were obtained using UV light.

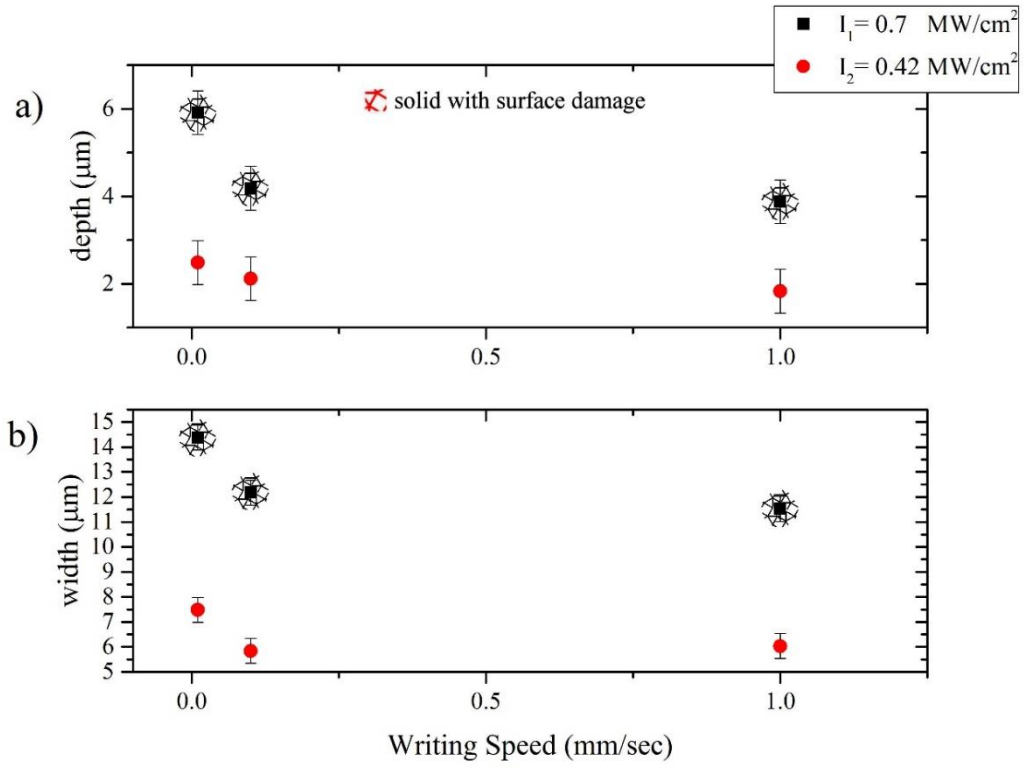

Figure 5.25 Comparison of PI domain depth and width in a-Si/CLN under the same writing intensity (0.42 MW/cm^2 and 0.7 MW/cm^2).

Poling inhibition in a-Si/CLN without removing the Si film: In the PI experiments that were shown in the previous section the Si film was removed prior to the EFP step using KOH etching. However, there is scope for using the laser processed a-Si film, which under certain conditions can be crystalized by the laser irradiation, therefore in this section we will investigate the ability to produce PI domains without the removal of the Si film.

A new sample was fabricated with the aim of obtaining PI domains without removing the a-Si film. The laser focussing this time was tighter (with spot size of ~2.2μm). The laser intensities used here were between 0.35 MW/cm^2 and 1.06 MW/cm^2 and the writing speed was varied from 0.016-0.16mm/sec. Following laser irradiation the sample was subjected to EFP by applying an electric field as in section 5.6.3. The poling process was in-situ visualised using a white light source by stress-induced birefringence at the domain walls [18] collimated through the crystal. An image of the domain wall formation/propagation can be seen in Figure 5.26.

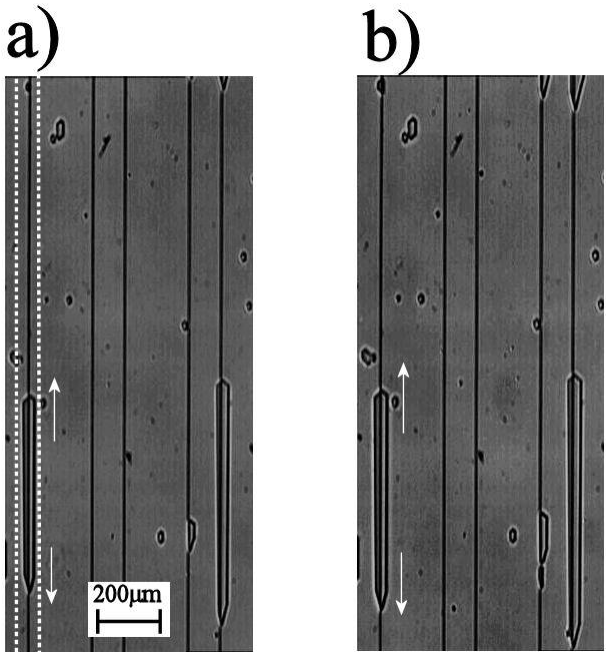

Figure 5.26 In situ optical visualization of the bulk domain formation in association with the laser written tracks. Frame (b) was taken 6 minutes after frame (a). The arrows indicate the directions of domain growth.

No qualitative difference between the EFP in the presence of the Si film and the EFP without was observed. However, this is not a systematic study of the poling process as it was beyond the scope of these experiments. Domain nucleation started at random points commonly along the irradiated regions and the motion of the domain wall was observed to be preferentially along to the laser tracks especially in the beginning of the process. Later, the domains expanded in the area between adjacent tracks and merged thus completing the EFP step.

Visualisation of the resulting PI domains inversion was achieved by wedge polishing, followed by brief HF etching. The SEM images of the wedge polished section shown in Figure 5.27 correspond to laser intensity of 0.51 MW/cm^2 and writing speed of 0.1 mm/min showing the formation of deep and solid PI domains, demonstrating that the PI fabrication process is not affected by the presence of the a-Si film.

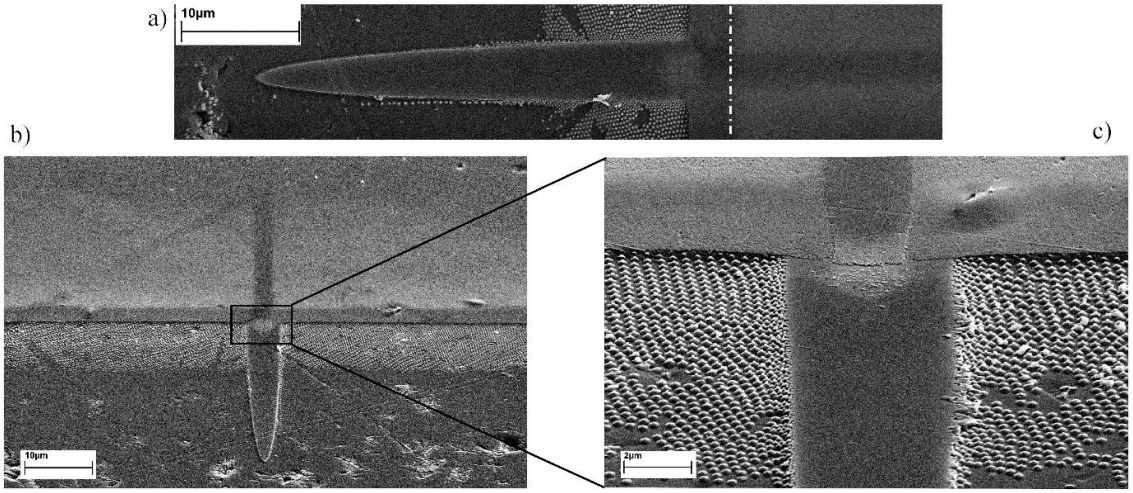

Figure 5.27 SEM images of the wedge-polished PI domains fabricated in (+z) a-Si/CLN sample under laser intensity of 0.51MW/cm^2 and writing speed of 0.016mm/min. a) view from the top, b) titled view at 60 degrees and c) magnified view of image b).

The SEM images of the wedge polished sections which are shown in Figure 5.27 reveal an assembly of nanometre size features which are located immediately bellow the Si film up to a depth of ~ 0.7 μm the origin of which is not clear at the moment. However, a similar effect was observed in EFP experiments that were attempted in proton-exchanged samples. Proton exchange damages the top crystal layer reducing or even eliminating the ferroelectricity locally. We believe that the Si layer plays the same role in the EFP process as the damaged layer in proton exchanged waveguides. As for the quality of the poling in the non-irradiated areas, it is found to be imperfect, showing an assembly of nanometre size features indicating local resistance of poling due to the a-Si film. This appearance of nano-domains extend up to ~1 μm of depth. Another observation of Figure 5.27c) is that through this technique it is possible to visualize the irradiated region on the a-Si film.

Since that irradiated area corresponds to crystalline Si, the observed contrast between the crystalline and amorphous Si could be attributed to the different electric properties of these two faces and their relevant interaction with the electrons beam of the SEM. Measurement of the width of that region don't match with the spot size of ~2.5 μm, while the width of the underlying PI domain found to be closer to that value. Additionally, an upward movement of the a-Si film relatively to the CLN crystal in the regions on either side of the irradiated area can be seen, which is possible caused by the HF acid. However, interestingly this movement doesn't occur on the irradiated area, where the a-Si film appears to be in contact with the CLN substrate and only a deformation of the film close to the boundaries of that area is shown to occur.

After taking measurements of the SEM images of the stretched depth profiles of the PI domains on a-Si/CLN sample, the domains depth was calculated. Figure 5.28 displays the

dependence of PI domain depth on the laser writing intensity for constant writing speed of 1 mm/sec. Comparing these measurements with PI domains obtained after prior removal of the Si film indicated that there is no significant difference between the two processes.

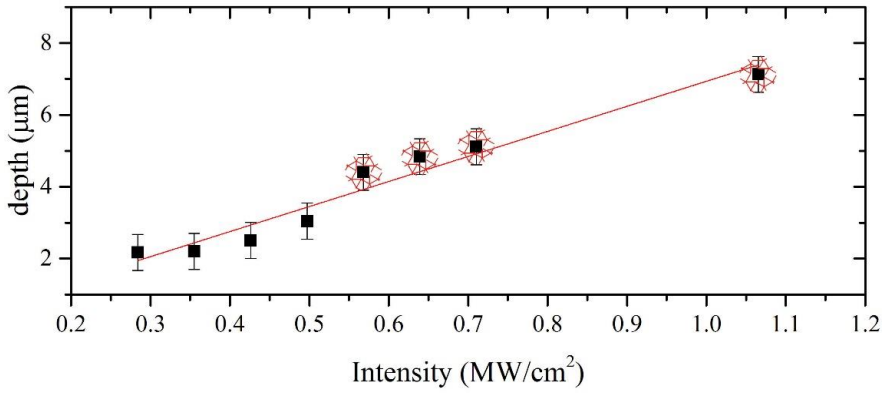

Figure 5.28 The depth of PI domains in a-Si/CLN plotted as a function of the writing laser intensity fabricated under constant writing speed of 0.16mm/sec.

Optical characterisation: In order to investigate the impact of the PI domain on the pre-existing waveguide, an optical characterisation at 633 nm wavelength was performed using the optical set-up shown in Figure 5.1. Because the sample was wedge-polished for the PI domain size measurements, end-face polishing was executed, following the polishing procedure described in 5.4.

The mode profiles taken appeared an unusual behaviour comparing with the pre-existing waveguide modes, i.e. before the uniform poling step. All the waveguides exhibited a single-mode profile, irrespectively of the written conditions. Waveguides written under the lowest intensity were placed close to the surface, however, for high laser intensities the waveguides found to be located deep in the crystal, of maximum estimated depth of ~ 10μm. The resultant effect is not clearly understood at the moment and differs significantly from the UV-written waveguides which can overlap with the UV-induced PI domain as shown in Chapter 3.

5.6.4 Directly-written domains induced by visible laser

Directly-written domain characteristics: depth, width and surface quality: Visible laser induced inverted domains were examined following the same experimental procedures as for PI domains. The sample that used for the optical characterisation in section 5.4.3, was wedge-polished at ~ 5^o and was immersed in HF acid (48%) for 3min at room temperature, revealing the opposite domains due to differential etching. SEM images of the stretched depth profiles of the domains were taken as shown in Figure 5.29. For reminder purposes, the writing conditions of that sample were:

~3.5 μm of spot size, laser beam intensities ranging from 0.2 MW/cm^2 to 1.6 MW/cm^2 and writing speeds of 0.01-1mm/sec.

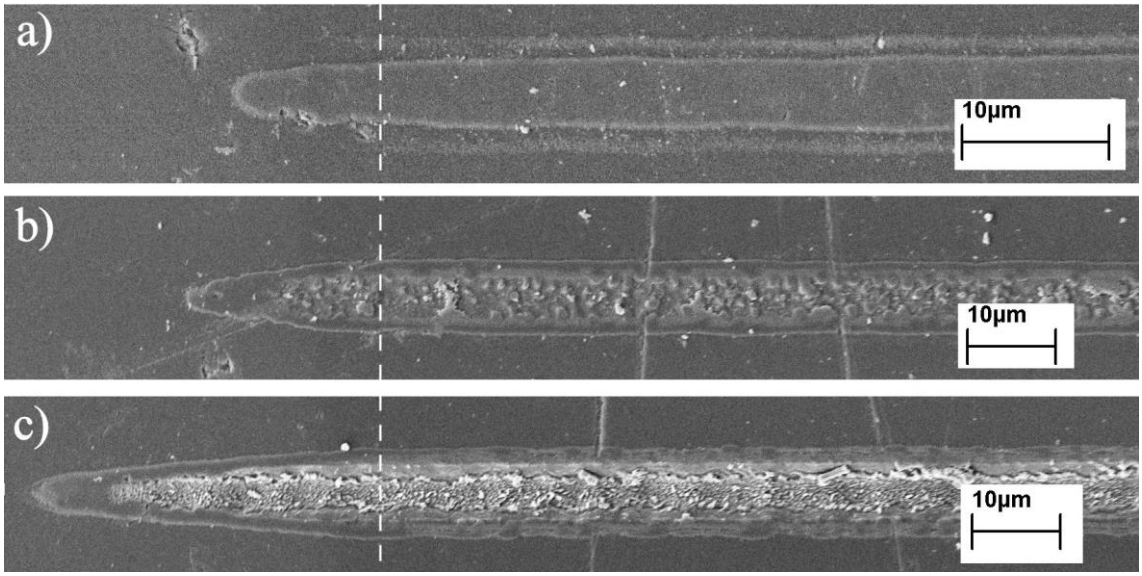

Figure 5.29 SEM images of the wedge-polished spontaneous inverted domains keeping the speed constant at 0.6mm/min and varying the writing intensity: a) 0.56 MW/cm^2 , b) 0.70 MW/cm^2, c) 0.84 MW/cm^2.

A solid domain without any surface damage can be obtain for intensity of 0.56 MW/cm^2 as can be seen in Figure 5.29a but for higher intensities surface damage was observed. Under the same writing conditions on the +z face of a-Si/CLN, same effects had been observed, however, on –z face the damage appears to be more intense and the whole process to be more violent. The solid inverted domain appears to be smaller also in comparison with the PI domain on +z face under the same writing conditions.

Measurements of depth and width of the inverted domains were taken from the SEM images of the stretched depth profiles yielding plots versus the writing intensity for all the writing speeds as shown in Figure 5.30. In this graph, domains above laser intensity of 0.7 MW/cm^2 suffer from surface damage, which becomes excessive for intensities above 0.84MW/cm^2.

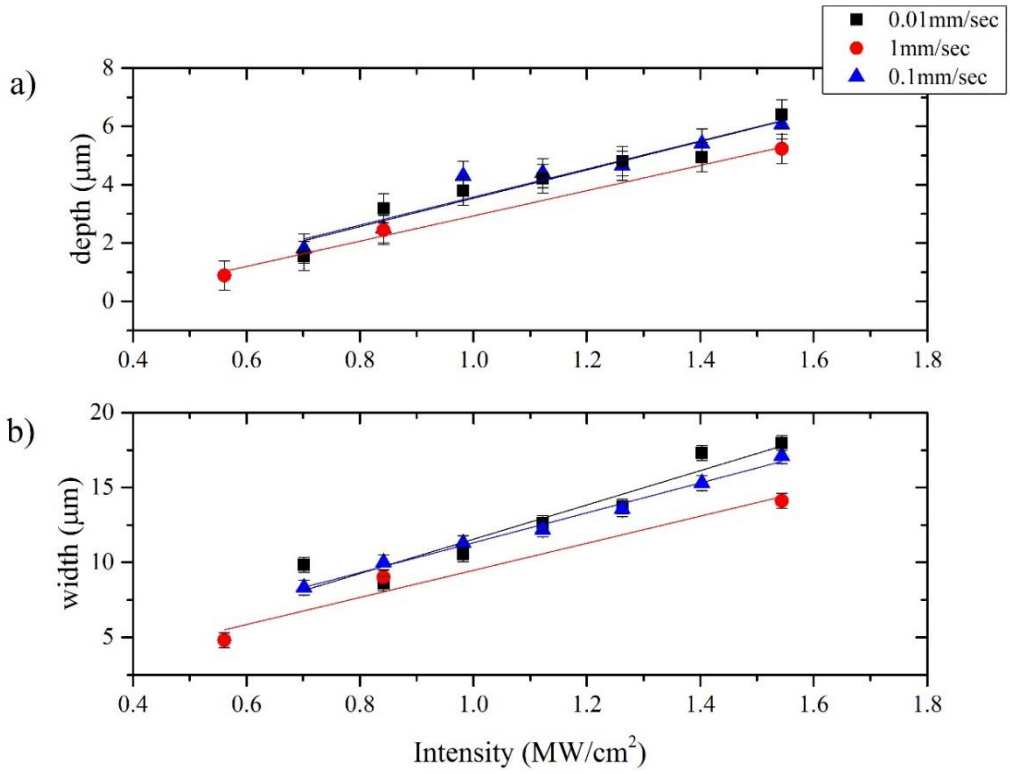

Figure 5.30 The width and depth of spontaneous inverted domains in –z face a-Si/CLN plotted as a function of the writing laser intensity under different writing speeds.

The relation between the domain sizes and the writing intensity is similar as in the PI domain case and appears linear. The role of the laser intensity is more important than the exposure time, which can be adjusted by the scanning speed as illustrated in Figure 5.31.

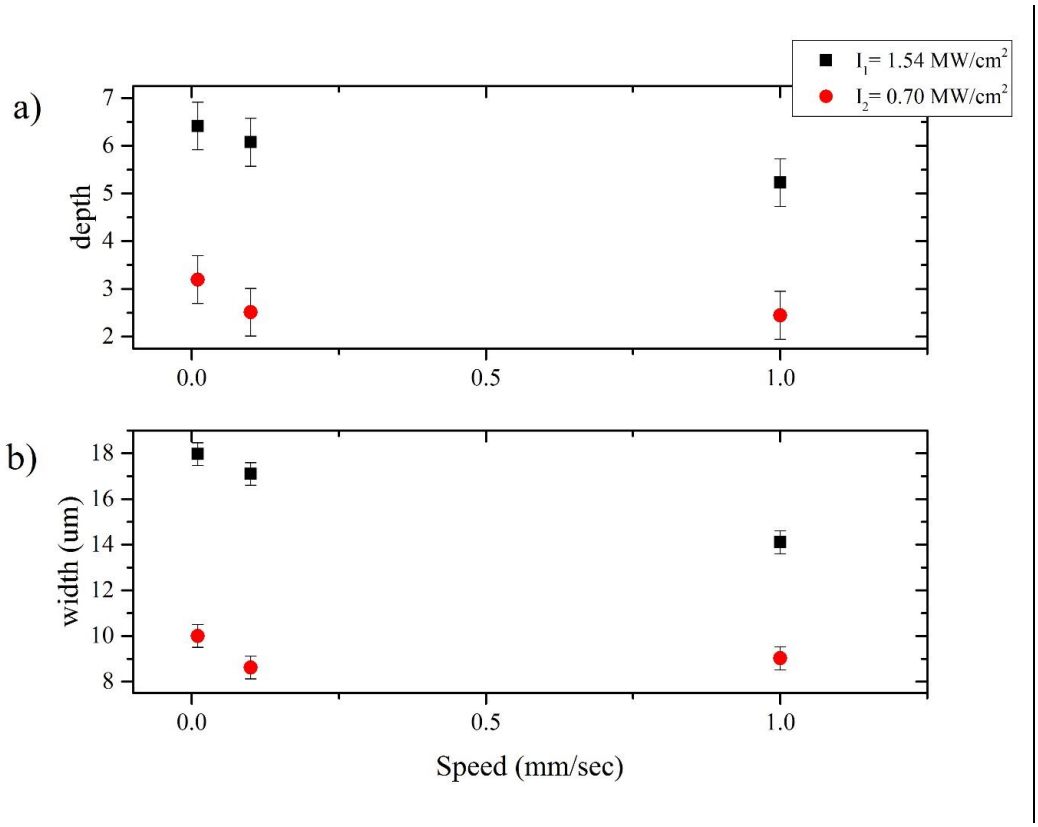

Figure 5.31 Comparison of spontaneous inverted domain depth (a) and width (b) in –z face a-Si/CLN under the same writing intensity (black dots: 1.54 MW/cm^2 and red dots: 0.70 MW/cm^2).

Optical characterisation of the fabricated waveguides on –z face a-Si/CLN is being described in section 5.4.3 where the spontaneous inverted domains didn't appear to affect the waveguide propagation.

5.6.5 Proposed mechanism for domain formation

In general, for both cases of visible laser induced PI and direct domain inversion, the mechanism appears to be similar as the one proposed for the explanation of the same effect due to UV irradiation. The strong absorption of the Si film in the visible wavelengths combined with the poor heat conductivity of CLN leads to a substantial increase of the temperature locally. The steep temperature gradients which are formed in the CLN substrate as a result of the heat of the a-Si film causes Li ions side diffusion. This change of the stoichiometry causes a local increase of the amplitude of the electric field which is required for domain inversion.

The dependence of the domain sizes mostly to the writing intensity and not to the writing speed indicates that the occurrence of direct poling depends strongly on the peak temperature which is achieved during laser irradiation and not on the duration that the crystal stays at an raised temperature. It has been proposed that the same effect for UV-laser induced domain inversion

originates from a synergy of electric fields, formed by displaced charge carriers and the pyro-electric field, which adds up to produce a net poling field during the cooling stage of the rapid heating-cooling cycle as a result of the laser irradiation. The similar results for a-Si/CLN while it's irradiated by visible laser beam indicates that this proposed mechanism was right and that it is mostly a thermal effect that takes place.

5.7 Conclusions

A study of the channel waveguide formation and ferroelectric domain fabrication induced by the direct visible laser irradiation on a-Si/CLN samples has been performed. More specifically we observed the formation of directly inverted domains on the –z face of the crystal and PI domain formation on the +z face. Optical channel waveguides were observed on both faces. These results indicate that it is possible to obtain the same effects that were previously observed using UV laser irradiation.

Single and multimode waveguide structures were fabricated and a dependence of the mode size on the irradiation conditions was found and presented here. Subsequent removal of the a-Si film after irradiation lead to a change of the propagating mode profile indicating a reduction of the spatial range and/or the refractive index change that was responsible for the waveguide formation. This is an indication that perhaps stress on the annealed a-Si/CLN interface could contribute to the observed refractive index change. Channel waveguides fabricated on +z face of a-Si/CLN samples were found to exhibit transmission of both TM and TE modes, at 633nm wavelength of incident laser beam, indicating that there is a significant increase of both the ordinary and extraordinary refractive indices, while waveguides fabricated on -z face of a-Si/CLN samples found to exhibit transmission TM modes only. TM mode propagation was observed on both faces at 1.52μm wavelength.

Waveguides written on +z face of a-Si/CLN composite show a minimum propagation loss of 3.69 dB/cm for infrared wavelength at 1.52nm, 5.04 dB/cm at visible wavelength of 633nm of TM polarisation and 4.53 dB/cm for TE polarisation of 633nm.

The PI domain formation on the +z face was observed allowing the fabrication of domains, which are deeper than their UV, irradiated counterparts and also exhibiting a lower level of laser induced surface damage. Spontaneous domain inversion (for –z face samples) was also observed. The domain size results as a function of irradiation conditions indicate that writing intensity is the most important parameter as compared to writing speed.

The formation of channel waveguides and the ability for domain engineering using an a-Si film as absorber not only allows the use of a conventional laser source for the processing of lithium niobate crystals but also confirms the previous hypothesis that all the effects that are associated with UV writing in lithium niobate have a thermal origin.

5.8 References

[1] S. Mailis, C. Riziotis, I. T. Wellington, P. G. R. Smith, C. B. E. Gawith, and R. W. Eason, "Direct ultraviolet writing of channel waveguides in congruent lithium niobate single crystals.," *Opt. Lett.*, vol. 28, no. 16, pp. 1433–5, Aug. 2003.

[2] C. L. Sones, a. C. Muir, Y. J. Ying, S. Mailis, R. W. Eason, T. Jungk, Á. Hoffmann, and E. Soergel, "Precision nanoscale domain engineering of lithium niobate via UV laser induced inhibition of poling," *Appl. Phys. Lett.*, vol. 92, no. 7, 2008.

[3] C. L. Sones, P. Ganguly, C. Y. J. Ying, E. Soergel, R. W. Eason, and S. Mailis, "Poling-inhibited ridge waveguides in lithium niobate crystals," *Appl. Phys. Lett.*, vol. 97, no. 15, p. 151112, 2010.

[4] C. Y. J. Ying, a. C. Muir, C. E. Valdivia, H. Steigerwald, C. L. Sones, R. W. Eason, E. Soergel, and S. Mailis, "Light-mediated ferroelectric domain engineering and micro-structuring of lithium niobate crystals," *Laser Photon. Rev.*, vol. 6, no. 4, pp. 526–548, 2012.

[5] A. Boes, D. Yudistira, T. Crasto, H. Steigerwald, V. Sivan, T. Limboeck, J. Friend, S. Mailis, E. Soergel, and A. Mitchell, "Ultraviolet laser induced domain inversion on chromium coated lithium niobate crystals," *Opt. Mater. Express*, vol. 4, no. 2, p. 241, 2014.

[6] A. Boes, V. Sivan, G. Ren, D. Yudistira, S. Mailis, E. Soergel, and A. Mitchell, "Precise, reproducible nano-domain engineering in lithium niobate crystals," *Appl. Phys. Lett.*, vol. 107, no. 2, p. 022901, 2015.

[7] H. Steigerwald, M. Lilienblum, F. von Cube, Y. J. Ying, R. W. Eason, S. Mailis, B. Sturman, E. Soergel, and K. Buse, "Origin of UV-induced poling inhibition in lithium niobate crystals," *Phys. Rev. B*, vol. 82, no. 21, p. 214105, 2010.

[8] A. C. Muir, G. J. Daniell, C. P. Please, I. T. Wellington, S. Mailis, and R. W. Eason, "Modelling the formation of optical waveguides produced in $LiNbO_3$ by laser induced thermal diffusion of lithium ions," *Appl. Phys. A*, vol. 83, no. 3, pp. 389–396, 2006.

[9] N. Healy, S. Mailis, N. M. Bulgakova, P. J. a Sazio, T. D. Day, J. R. Sparks, H. Y. Cheng, J. V Badding, and A. C. Peacock, "Extreme electronic bandgap modification in laser-crystallized silicon optical fibres.," *Nat. Mater.*, no. September, pp. 1–6, 2014.

[10] G. T. Reed, "Device physics: The optical age of silicon," *Nature*, vol. 427, no. 6975, pp. 595–596, 2004.

[11] R. S. Weis and T. K. Gaylord, “Lithium Niobate: Summary of physical properties and crystal structure,” *Appl. Phys. A*, vol. 37, no. 4, pp. 191–203, 1985.

[12] F. Jansen and S. Krommenhoek, “Thin film deposition on inside surfaces by plasma enhanced chemical vapor deposition,” *Thin Solid Films*, vol. 252, no. 1, pp. 32–37, 1994.

[13] C. L. Sones, P. Ganguly, Y. J. Ying, F. Johann, E. Soergel, R. W. Eason, and S. Mailis, “Spectral and electro-optic response of UV-written waveguides in $LiNbO_3$ single crystals.,” *Opt. Express*, vol. 17, no. 26, pp. 23755–64, 2009.

[14] J. R. Carruthers, G. E. Peterson, M. Grasso, and P. M. Bridenbaugh, “Nonstoichiometry and crystal growth of lithium niobate,” *J. Appl. Phys.*, vol. 42, no. 5, pp. 1846–1851, 1971.

[15] C. L. Sones, S. Mailis, W. S. Brocklesby, R. W. Eason, and J. R. Owen, “Differential etch rates in z-cut $LiNbO_3$ for variable HF/HNO_3 concentrations,” *J. Mater. Chem.*, vol. 12, no. 2, pp. 295–298, 2002.

[16] C. Y. J. Ying, G. J. Daniell, H. Steigerwald, E. Soergel, and S. Mailis, “Pyroelectric field assisted ion migration induced by ultraviolet laser irradiation and its impact on ferroelectric domain inversion in lithium niobate crystals,” *J. Appl. Phys.*, vol. 114, no. 8, p. 083101, 2013.

[17] S. Mailis, C. Sones, J. G. Scott, and R. W. Eason, “UV laser-induced ordered surface nanostructures in congruent lithium niobate single crystals,” *Appl. Surf. Sci.*, vol. 247, no. 1–4, pp. 497–503, 2005.

[18] V. Gopalan and T. Mitchell, “In situ video observation of 180 domain switching in $LiTaO_3$ by electro-optic imaging microscopy,” *J. Appl. Phys.*, vol. 85, no. 4, pp. 2304–2311, 1999.

Chapter 6: Future Work

A number of approaches have been presented in this thesis for the processing of lithium niobate crystals in terms of domain engineering, waveguide fabrication and surface micro-structuring which hold potential for the realisation of photonic devices. Nevertheless, supplementary work will be required in order to further understand and control several aspects of these methods for practical applications. Some suggestions for further work are given here.

UV laser-induced poling-inhibition in CLN

Future plans involve the surface tension reshaping for smoothening of ridge photonic structures and the development a titanium or gallium diffusion process for increasing the refractive index of the top ridge section. Particularly for gallium diffusion in lithium niobate has been reported to produce a 3.3×10^{-3} [1] refractive index change and has the advantage of being a relatively low temperature process. In addition, the PI domain based ASL transducers devices will be characterized and analysed. Because of the restriction of the spot size of the UV-laser beam, the widths of the PI domains are not equal with their adjacent domains (i.e. the inverted domains) causing problem to the periodicity. This can be solved by combining individual PI domains to produce larger complex domain structures as discussed on the relative chapter, or by simply decreasing the period Λ which will allow the increase of the operation frequency according to Eq. 2-1. Fabrication of an integrated AO filters using a PI based ASL structure associated with a single-mode Ti in-diffused or PE optical waveguide should be attempted as well.

Local enhancement of the electro-optic coefficient in poling inhibited CLN channel waveguides

The proposed method has the potential to reduce the complexity of fabrication of electro-optic devices and would be extremely well-suited for the implementation of the dense compact photonic circuits for future optoelectronic technologies. One of the future tasks is to investigate the possible enhancement of the nonlinear performance of devices that consist of PI domains. More specifically, a PPLN sample consisted by UV-induced PI domains should be fabricated and the SHG efficiency should be measured. A possible observation of an enhancement of the second-order nonlinear coefficient would provide a sufficient clarification on the proposed mechanism for the enhancement of the effective electo-optic coefficient as discussed on section 3.6.

UV laser-induced poling inhibition in proton exchanged LN crystals

The UV laser induced redistribution of protons consequently modifies the refractive index profile of the original waveguide providing lateral confinement for the propagating light hence it could be used for post fabrication trimming of the characteristics of planar or channel PE waveguides in congruent and Mg-doped lithium niobate.

Direct writing of channel waveguides and PI domains in LN using an amorphous silicon absorption layer

Further investigation of the proposed mechanism is needed. More precisely, through Micro-Raman spectroscopy it would be possible to measure the mechanical stress with micrometric spatial resolution [2]. Distributions of mechanical stress in a-Si:CLN waveguides can be measured on the waveguide facets. Also, an improvement of the existing model [3] that explains the formation of waveguides by laser induced thermal diffusion of lithium ions should be performed, recalculating the laser induced temperature distribution on the CLN substrate by taking into account the presence of the a-Si film and a possible silicon diffusion in CLN.

Optimisation of the writing conditions for best crystallisation of the a-Si film upon the irradiated regions and subsequently the waveguide formation on CLN substrate is also required and already being under investigation by the group. The influence of the thickness of the a-Si film should be also taken into account for both effects. Lastly, domain engineering on a-Si:CLN samples requires additional study. PFM images could provide more information about the nano-domains that occur when poling is performed without firstly remove the a-Si film. SAW and SHG devices should be easy to achieved, showing the capabilities of this technique and subsequently check their performance and what is the impact due to the presence of the nano-domains

6.1 References

[1] W. W. Huang and W. W. Wang, “Gallium in-diffusion for the fabrication of Lithium Niobate optical waveguides,” *Photonics Technol. Lett. IEEE*, vol. 19, no. 20, pp. 1679–1681, 2007.

[2] F. Bianco, K. Fedus, F. Enrichi, R. Pierobon, M. Cazzanelli, M. Ghulinyan, G. Pucker, and L. Pavesi, “Two-dimensional micro-Raman mapping of stress and strain distributions in strained silicon waveguides,” *Semicond. Sci. Technol.*, vol. 27, no. 8, p. 085009, 2012.

[3] A. C. Muir, G. J. Daniell, C. P. Please, I. T. Wellington, S. Mailis, and R. W. Eason, “Modelling the formation of optical waveguides produced in $LiNbO_3$ by laser induced thermal diffusion of lithium ions,” *Appl. Phys. A*, vol. 83, no. 3, pp. 389–396, 2006.

Appendix

List of Publications

Journal papers

- **G.Zisis**, C.Y.J.Ying, E.Soergel, and S.Mailis, "Ferroelectric domain building blocks for photonic and nonlinear optical microstructures in $LiNbO_3$," *J. Appl. Phys*., vol. 115, no. 12, p. 124102, Mar. 2014.

Papers under preparation

- **G. Zisis**, M. Manzo, K. Gallo, E. Soergel, S. Mailis, "UV laser-induced poling inhibition in proton exchanged $LiNbO_3$ crystals", In preparation for submission to Journal of Applied Physics.
- **G. Zisis,** C.Y.J.Ying, P.Ganguly, C.L.Sones, E.Soergel, R.W.Eason, S.Mailis, "Enhancement of the Electro-Optic response in domain engineered $LiNbO_3$ Channel Waveguides", In preparation for submission to Applied Physics B.
- G.Martinez, **G.Zisis**, Y.Franz, N. Healy, A.C.Peacock, H.M.H. Chong, D.Grech, S.Mailis, "Visible laser induced domain engineering in amorphous silicon coated lithium niobate crystals", In preparation for submission to Applied Physics Letters.

Conferences presentations

- S.Mailis, N.Healy, G.Martinez-Jimenez, **G.Zisis**, Y.Franz, D.Grech, H.M.H. Chong, A.C. Peacock, "A silicon/lithium niobate hybrid photonic material platform produced by laser processing", Keynote lecture, EUROMAT 2015, Warsaw, Poland 20-25 Sept. 2015
- G.Martinez, **G.Zisis**, Y.Franz, N.Healy, A.C.Peacock, H.Chong, D.Grech, S.Mailis, "Laser crystallization of silicon on lithium niobate", *Conference on Lasers and Electro-Optics (CLEO '14):* San Jose, CA 8-13 Jun 2014
- **G.Zisis**, C.Y.J.Ying, E.Soergel, S.Mailis, "UV laser-induced poling inhibited domain building blocks for photonic and nonlinear optical microstructures", *CLEO/Europe-IQEC 2013* Munich 12-16 May 2013.
- **G.Zisis**, M.Manzo, K.Gallo, E.Soergel, S.Mailis, "UV laser-induced poling inhibition in proton exchanged optical waveguides in lithium niobate", *PR13* Winchester 4-6 Sept 2013
- S.Mailis, G.Martinez, **G.Zisis**, Y.Franz, N.Healy, A.C.Peacock, "Annealing of amorphous silicon using c.w. visible lasers", *E-MRS '14 Materials Research Society Spring Meeting* Lille 26-30 May 2014.
- C.Y.J.Ying, **G.Zisis**, A.R.Naylor, P.Ganguly, C.L.Sones, E.Soergel, R.W.Eason, S.Mailis, "Local electro-optic coefficient enhancemant in $LiNbO_3$ channel waveguides by domain engineering", *PR11: Light in nonlinear structured materials* Ensenada Mexico 13-15 Oct 2011 (Invited).
- C.Y.J.Ying, **G.Zisis**, A.R.Naylor, P.Ganguly, C.L.Sones, E.Soergel, R.W.Eason, S.Mailis, "Enhancement of effective electro-optic coefficient in domain engineered UV-written waveguides in $LiNbO_3$", *CLEO/QELS 2011* Baltimore 1-3 May 2011.
- C.Y.J.Ying, **G.Zisis**, A.R.Naylor, P.Ganguly, C.L.Sones, E.Soergel, R.W.Eason, S.Mailis, "Electro-optic coefficient enhancement in poled $LiNbO_3$ waveguides", *CLEO/Europe-EQEC 2011* Munich 22-26 May 2011